Investigation of Thermoelectric Thallium Chalcogenides

by

Yixuan Shi

A thesis

presented to the University of Waterloo

in fulfillment of the

thesis requirement for the degree of

Doctor of Philosophy

In

Chemistry

Waterloo, Ontario, Canada 2020

Examining Committee Membership

The following served on the Examining Committee for this thesis. The decision of the Examining Committee is by majority vote.

External Examiner	Jian He Associate Professor
Supervisor(s)	Holger Kleinke Professor
Internal Member	Pavle Radovanovic Professor
Internal-external Member	David Hawthorn Professor
Other Member(s)	Dmitriy Soldatov Associate Professor

Author’s declaration

I hereby declare that I am the sole author of this thesis. This is a true copy of the thesis, including any required final revisions, as accepted by my examiners. I understand that my thesis may be made electronically available to the public

Abstract

Thermoelectric materials have drawn extensive attention because of their potential to provide assistance in reducing the usage of fossil fuel sources and the greenhouse effect. Throughout this thesis, the purpose was to investigate the thermoelectric properties of previously reported thallium tellurides. $Tl_2Ag_{12}Te_{7+\delta}$, $TlSbTe_2$, and $Tl_4Ag_{18}Te_{11}$ were selected as candidates for this investigation due to their interesting crystal structures. By substituting the Te element in $Tl_2Ag_{12}Te_{7+\delta}$, with Se we found a new phase of Tl-Ag-Se system which crystallizes in a commensurate superstructure and possesses ultralow thermal conductivity. These four parent compounds have low thermal conductivity owing to the high molar mass and complex crystal structures.

In Chapter 1, thermoelectric background knowledge was introduced. Generally, complex crystal structures such as incommensurate superstructures can reduce the lattice thermal conductivity, which is beneficial for increasing the thermoelectric figure of merit. The minimum lattice thermal conductivity can be estimated by three different models: Clarke model, Cahill model, and Diffuson model. Finally, a brief review of the state-of-the-art chalcogenide thermoelectrics was presented.

In Chapter 2, the experimental procedures related to all the projects were described. Powder X-ray diffraction, single crystal X-ray diffraction, and energy depressive X-ray analysis were utilized to obtain the compositional and structural information of the synthesized materials. Electronic structures of the materials were determined by performing first principle density

functional theory calculations. Then the physical properties including melting point, Seebeck coefficient, electrical conductivity, and thermal conductivity were determined.

In Chapter 3, a new selenide, $Tl_2Ag_{12}Se_7$, is reported. Unlike $Tl_2Ag_{12}Te_{7+\delta}$, $Tl_2Ag_{12}Se_7$ crystallizes in a commensurate superstructure with a √3 × √3 × 1 super cell of the $Zr_2Fe_{12}P_7$ structure type. Initial investigations into the thermoelectric properties of this selenide suggested that it was a *p*-type semiconductor at room temperature that underwent a *pnp* phase transition at 410 K. Further investigations via XPS indicated that the electronic states of all atoms did not undergo significant variations before and after the phase transition temperature. The reanalysis of the raw data obtained from the ZEM-3 instrument and the low temperature Seebeck measurements implemented by the PPMS also confirmed that $Tl_2Ag_{12}Se_7$ remains a *p*-type semiconductor throughout all temperatures investigated.

In Chapter 4, $Tl_2Ag_{12}Te_{7+\delta}$ was originally reported by Moreau *et al.* to crystallize in the hexagonal space group *P*6.[1] The unrealistically short Te-Te bond distances in the reported crystal structure (2.4 Å) led us to investigate the crystal structure further. We determined that $Tl_2Ag_{12}Te_{7+\delta}$ is actually an incommensurate composite crystal structure composed of a linear Te atom chain along the *c* axis surrounded by a $Tl_2Ag_{12}Te_6$ framework. The super-space group of the Te atom chain is $P6(00\gamma)s$ and the super-space group of the $Tl_2Ag_{12}Te_6$ framework is $P6_3(00\gamma)s$. The complex crystal structure resulted in an extremely low thermal conductivity of 0.25 W m^{-1} K^{-1} and a *zT* of 1.1 at 525 K. This is the largest thermoelectric figure of merit observed in an incommensurate crystal structure to date.

In Chapter 5, the $TlSbTe_2$ crystal structure shares similarities with the crystal structure of the state of the art thermoelectric material Bi_2Te_3. Both have a layered crystal structure; this

layered structure in Bi_2Te_3 leads to anisotropic electronic properties depending along which crystallographic axis the properties are measured. $TlSbTe_2$ has significantly more covalent interactions between the telluride layers diminishing the anisotropic effects. The best thermoelectric performance of In-doped $TlSbTe_2$ was achieved at 625 K, with a figure of merit (zT) of 0.77. The overall best zT was improved to 0.85 at 620 K with the sample of nominal composition $Tl_{0.98}SbYb_{0.02}Te_2$.

In Chapter 6, $Tl_4Ag_{18}Te_{11}$ was claimed to crystallize in a cubic structure with disordered Tl atoms filling cuboctahedral voids. The electronic structure calculations of $Tl_4Ag_{18}Te_{11}$ predicted it to be a semimetal with the valence and conduction bands touching at the Γ point in the Brillouin zone, based on an *I*4*mm* space group model with ordered Tl atom sites. The studies of the thermoelectric properties of hot-pressed $Tl_4Ag_{18}Te_{11}$ and its nonstoichiometric homologs, illustrated an unusual *n*-type extrinsic semiconducting behavior, combined with an extremely low thermal conductivity. The thermal conductivity of a sample of the nominal composition "$Tl_{4.05}Ag_{18}Te_{11}$" reached 0.19 W m^{-1} K^{-1} at 500 K, with this value being one of the lowest achieved by crystalline materials to date. This can be attributed to the highly disordered Tl atoms and the large unit cell with its highly complex structure, in accord with the low Debye temperature of 98 K.

Acknowledgements

Foremost, I would like to show my deepest and sincere gratitude to my supervisor, Dr. Holger Kleinke, who has guided my doctoral studies patiently and meticulously. His passionate and "can do" altitude inspired me throughout my graduate academia. He encouraged and supported me throughout my time doing research, and he also provided me with many excellent opportunities to collaborate with other researchers and industrials worldwide. I credit having such an amazing Ph.D. experience to Holger.

Additionally, many thanks to the rest committee members: Dr. Linda Nazar, Dr. Pavle Radovanovic, and Dr. Dmitriy Soldatov. Dr Nazar, a very outstanding woman scientist, I am grateful to her invaluable advice on organizing the "big picture" of my current research. I am thankful to Dr. Pavle Radovanovic for his kind encouragement and insightful advice on my nanotechnology and semiconductor studies. I also want to thank Dr. Dmitriy Soldatov, not only did he drive from Guleph to Waterloo to attend my doctoral proposal seminar, he also offered many constructive suggestions for my crystallography studies. I appreciate the help from all three of these professors to make my Ph.D. studies stay on track.

I am grateful to Dr. Sven Lidin for helping me with the incommensurate structure determination. I would like to thank Dr, Yu-chih Tseng, my internship supervisor at the CANMET institution, for his generous help improving my engineering skills. I would like to thank Dr. Abdeljalil Asssoud, who is both a mentor and a friend to me, for his guidance and assistance. I am also grateful to Mrs. Katja Kleinke for the countless times she has helped during lab work and with my English grammar.

I shall thank all my former and present colleagues, Quansheng Guo, Nader Farahi, Nagarai Nandihalli, Nhi Truong, Mohammed Oudah, Rafay Shams, Mathew VanZant, Parisa Jafarzadeh, Wenbin Ji, Xiaoyu Cheng, Cheryl Strum, Daniel Ramirez, Luke Menezes, Leilane Macario, Simeon Ponou, Bryony Stanbridge, Nour Mashmoushi, Zahra Sepahi, and Yanran Zheng, for their warm help and shared experience.

I want to thank all my friends and relatives for their endless support and love.

Last but not least, I would like to thank my parents, who countlessly offered me financial and mental support.

Yixuan

Contents

List of Figures

List of Tables

List of Symbols and Abbreviations

Symbols

zT	the dimensionless figure-of-merit of thermoelectric material
σ	electrical conductivity
S	Seebeck coefficient
κ	thermal conductivity
κ_e	electrical thermal conductivity
κ_L	lattice thermal conductivity
T	temperature
n	carrier concentration
μ	carrier mobility
E_F	fermi level
m^*	effective mass
c	heat capacity
PXRD	powder X-ray diffraction
DSC	differential scanning calorimetry
DOS	density of states
TE	thermoelectric
TG	thermogravimetry
EDX	energy dispersive X-ray spectroscopy
SEM	scanning electron microscopy

Chapter 1: Introduction

1.1 Thermoelectric Motivation

Thermoelectric (TE) energy generation has become incrementally more important due to the continuously depleting fossil fuel resources and mankind's increasing demand for power sources.[2] TE materials enable the conversion from waste heat to electricity and also enable refrigeration by electricity.[2–5] TE generators have been applied in the field of aerospace on the Martian Curiosity rover[6] and Lunar Chang'e-4[7] to overcome the ultralow temperature and lack of solar power in space. Commercial applications have also been launched, such as body temperature powered watch[8] and portable coolers. However, TE devices are still limited by their low conversion efficiency, so researchers are industriously searching more efficient TE materials. In this chapter, the principles of TE research, a brief summary of chalcogenide TEs, and an introduction of some misfit structures will be discussed.

1.2 Thermoelectric Effect

In 1821, German physicist Thomas Johann Seebeck discovered that a voltage can be generated when a temperature gradient is provided to a *p*-type and *n*-type junction (Figure 1-1a). Thirteen years later, French physicist Jean Charles Peltier noticed an inverse phenomenon, where a temperature difference can be produced by a junction of *p*-type and *n*-type materials when a voltage is applied (Figure. 1-1b). These two effects establish the foundation of TE studies and are named after these two outstanding physicists.[9]

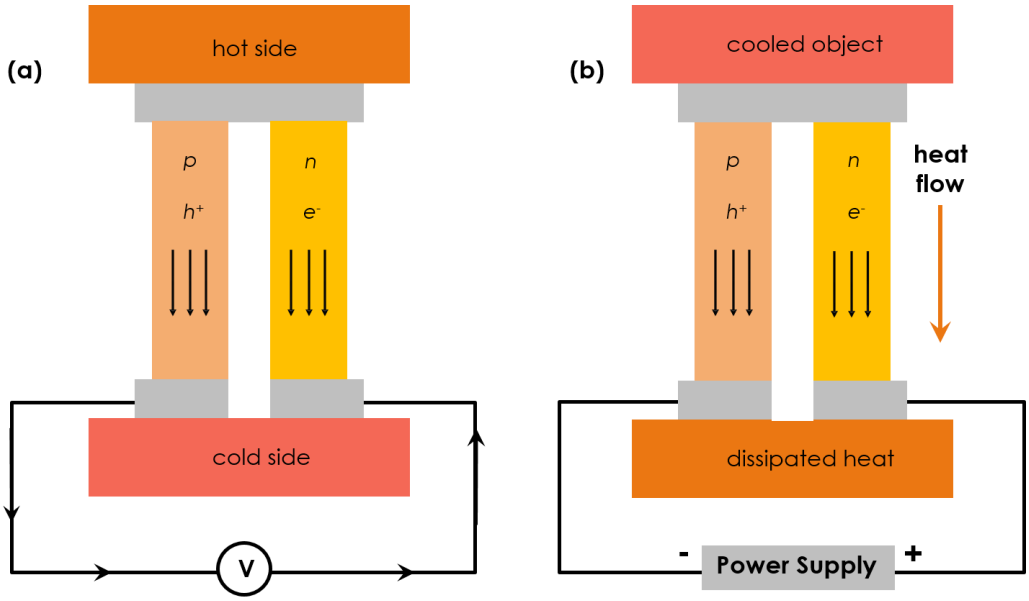

Figure 1-1: a) The power generation mode based on the Seebeck effect and b) the solid state cooling mode based on the Peltier effect.

1.3 Thermoelectric Evaluation

The performance of a TE material is evaluated by a dimensionless figure of merit, zT, which is defined in Eq. (1-1),[5]

$$zT = \frac{S^2 \sigma T}{\kappa} \tag{1-1}$$

where *S* is the Seebeck coefficient, σ is the electrical conductivity, *T* is the absolute temperature, and κ is the total thermal conductivity. *p*-type semiconductors exhibit positive Seebeck coefficient as the carriers in the material are governed by the holes, while *n*-type semiconductors show negative values as the carriers inside are dominated by the electrons. The power factor, *P.F.,* is the product of α^2 and σ (Eq. (1-2)), describing the electrical performance of a TE material.

$$P.F. = S^2 \sigma \tag{1-2}$$

The electrical conductivity is calculated based on Eq. (1-3),

$$\sigma = n\, e\, \mu \tag{1-3}$$

where e is the electron's charge, and μ is the charge carrier mobility. The total thermal conductivity (Eq. (1-4)) consists of the lattice thermal conductivity, κ_L, caused by the phonons traveling through the lattice, and the electrical thermal conductivity, κ_e, resulting from the heat transferred by charge carriers.

$$\kappa = \kappa_L + \kappa_e \tag{1-4}$$

According to the Wiedemann-Franz law[10], κ_e can be determined via Eq. (1-5),

$$\kappa_e = n\, e\, \mu\, L_0\, T \tag{1-5}$$

where L_0 denotes the Lorenz number.

All these physical properties except κ_L are interrelated to each other as functions of carrier concentration, n. n can be influenced by the doping level, temperature, and defects. In general, α increases but σ and κ decrease with n. As a result, there is no beau ideal method to optimize these variables (except κ_L). The carrier concentration range for achieving optimized zT has been demonstrated to be 10^{19}-10^{20} cm^{-3}, and such range usually belongs to the degenerate semiconductors.[5] κ_L , however, can be minimized by including heavier elements such as thallium, antimony, tellurium, and lead without a detrimental impact on the other properties. More complex crystal structures can also provide a lower κ_L via lowering μ, but the mobility decrease therein is often is detrimental to σ.[4,5]

The efficiency of a TE device, η, is determined by Eq.1-6, where $\overline{ZT}$ is the average figure of merit over the whole temperature range, and T_C and T_H are the temperatures at the cold and hot ends, respectively.

$$\eta = \frac{T_H - T_C}{T_H} \times \frac{\sqrt{1+\overline{ZT}} - 1}{\sqrt{1+\overline{ZT}} + {T_C}/{T_H}} \tag{1-6}$$

The maximum efficiency is constrained by the Carnot limit and as well the *zT* values.[11] Figure 1-2 is represented to have a better visualization of the relationship between the thermoelectric device efficiency and the average figure of merit.

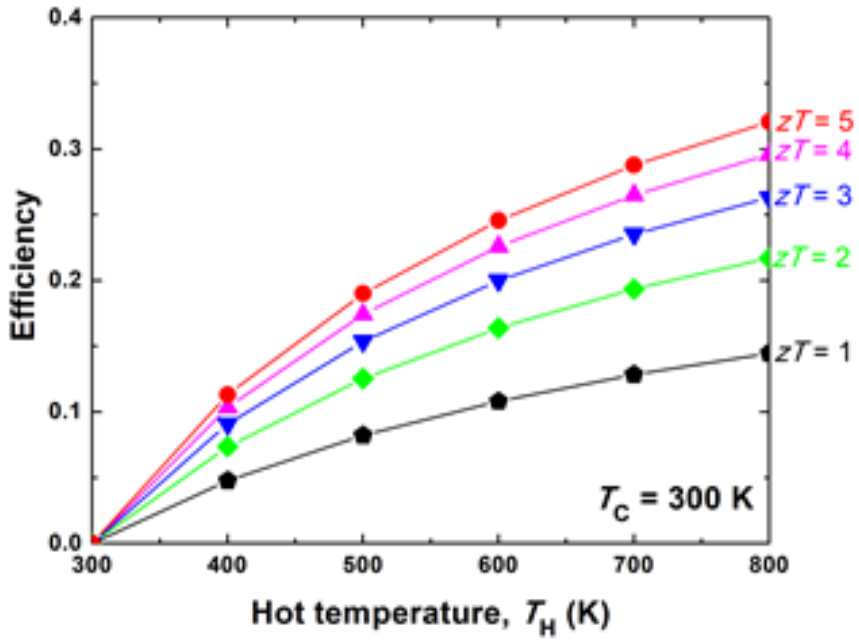

Figure 1-2: The efficiency of thermoelectric devices as a function of hot-end temperatures, assuming the cold-end remains at 300 K.[12]

1.3.1 Lattice Thermal Conductivity

Since lattice thermal conductivity is independent to other TE variables, lowering κ_L can be an effective strategy to increase *zT* values. The lattice thermal conductivity of glass-like crystals or amorphous materials is quite low, nonetheless, the actual glasses have poor TE performance because of their low electrical conductivity. Therefore, the ideal candidates for TEs are postulated to have the features of a "phonon-glass, electron-crystal" (PGEC). In addition, heat in a glass are transported randomly through the lattice rather than orderly via phonons, which results in the concept of minimum thermal conductivity.

Heat is generated from the vibrations of atoms (which are a function of atomic mass). The greater the amplitude of the vibrating atoms; the more heat is produced. Heavy elements can help to reduce κ_L at elevated temperatures, due to the lower heat capacity caused by their larger average molecule mass, *M*, based on the Dulong-Petit estimation.

Based on this theory, alloying with heavier elements is one strategy to lower κ_L, in addition because of the mass fluctuation effect. Mass fluctuation can lower the lattice thermal conductivity by creating more point defects; thus, scattering phonons more efficiently as a result of mass differences. Successful examples applying mass fluctuation include $BaCu_{6-x}Se_{1-y}Te_{6+y}$,[13] $Mg_2Si_ySn_{0.97-y}Bi_{0.03}$,[14] $FeV_{1-x}Nb_xSb$,[15] and so on.

Inserting defects (such as interstitial defects, vacancies, substitutions) into crystals, making rattling structures, or creating misfit structures can also lead to lower κ_L, because the phonons are scattered more efficiently in these structures. The disorders in these structures decreases the phonon mean free path, which is proportional to κ_L as seen in Eq. (1-6).

$$\kappa_L = \frac{1}{3} c v_s l_{MFP} \tag{1-6}$$

Where c is the specific heat per unit volume. v_S the mean phonon speed, and l_{MFP} the average phonon mean free path.

Other approaches that had been successfully applied to reduce κ_L are using nanostructures and nanocomposites.[12] Both nanostructures and nanocomposites create more interfaces to scatter phonons (shorter phonon mean free path) without necessarily affecting the electron mean free path.

1.3.2 Minimum Thermal Conductivity

There are two different models of determining minimum thermal conductivity based on phonon theory, the Clarke model and the Cahill model. In the Clarke model, the minimum thermal conductivity limit is reached when the phonon mean free path length is on the order of interatomic spacing (a).[16] In the Cahill model, he used half of a wavelength of the phonon to describe the mean free path to obtain the minimal thermal conductivity.[17] Other than the phonon basis, Synder used a diffuson as basis.[18] The differences between these two basis is visually illustrated in Figure 1-3. In the diffuson model, the diffusons are assumed as they can travel and collide in a random way, whereas in the phonon model, phonons have to propagate in a collective way that is related to the group velocity and relaxation time. Since the diffuson model relys on a thermal diffusivity resulting from random walk considerations, the two operative theoretical inputs, jump attempt frequency ($\frac{2\varpi}{2\pi}$) and successful jump probability (P) are considered. The diffuson rate is proportional to P, and P is an empirical number. When P = 1, it reaches the

maximum diffusive thermal conductivity, and when P = 0, it assumes that no energy or heat is transferred. The κ_{diff} represents the minimum of thermal conductivity when vibrations are both not propagating (not phonon-like) and not localized (specifically, P = 1).

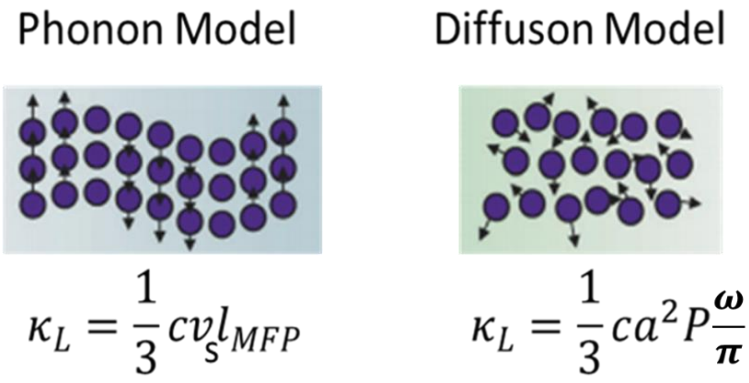

Figure 1-3: Lattice thermal conductivity models.

The equations for these three different methods can be simplified as:

Cahill: $\kappa_{glass} = 1.21 n_a^{2/3} k_B v_S$

Clarke: $\kappa_{min} = 0.93 n_a^{2/3} k_B v_S$

Snyder: $\kappa_{diff} = 0.76\, n_a^{2/3} k_B v_S$

where n_a is the number density of atoms (the number of atoms per cell per unit volume). v_S is the arithmetic average sound velocity, given by equation:

$$v_S = \frac{1}{3}(2v_T + v_L)$$

where v_T and v_L are defined as transverse and longitudinal velocities of sound, respectively. The Debye temperature, ϑ_D, is directly proportional to the sound velocity:

$$\vartheta_D = \frac{\hbar}{k_B}(6\pi^2 n_a)^{1/3} v_S$$

Therein, $\hbar$ is the reduced Planck constant, k_B the Boltzmann constant.

The ideal minimum thermal conductivity is expected to be always lower than the experimental measured thermal conductivity values. The minimum thermal conductivity value given by κ_{diff} is approximately 37% lower than the κ_{glass} of Cahill and 18% lower than the κ_{min} estimate of Clarke according to the identical experimental input data. However, if a thermal conductivity below the κ_{diff} limit is observed, it may indicate the existence of localized vibrations, phonon focusing, or other extraordinary physical mechanisms.

1.4 Incommensurate Superstructures

In classical crystallography, the atomic assemblies are considered to be complete and periodic repetitions. However, the definition of aperiodic crystal structures emerged when aperiodic atomic arrangements were observed, such as incommensurate superstructures and quasicrystal. A superstructure denotes a structure containing substructures that are equal or nearly equal in configuration. The space group of the superstructure is a subgroup of the space group of the substructures, and at least one of the Wyckoff positions of the subcell is split into at least two separate Wyckoff positions in the supercell. Superstructures can be categorized as commensurate and incommensurate ones. Furthermore, the incommensurate structures are classified as incommensurate modulated structures and incommensurate composite structures.[19]

1.4.1 Incommensurate Modulated Superstructure

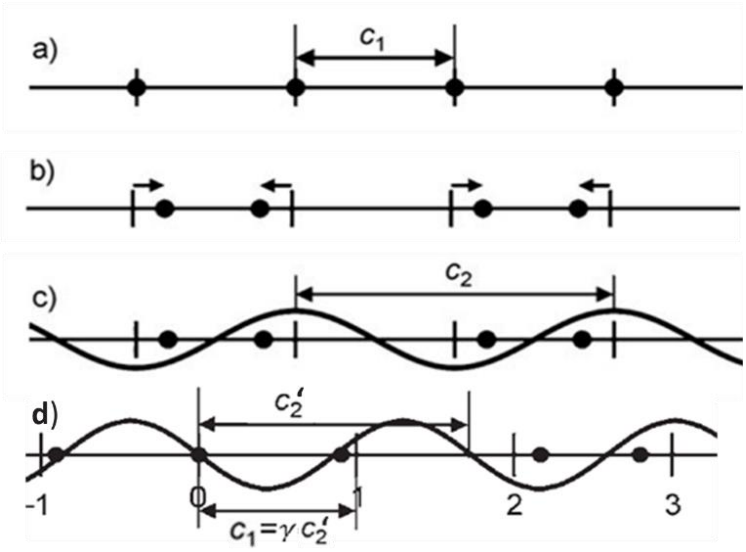

Figure 1-4: Incommensurate modulated superstructure schematic illustration.

As shown in Figure 1-4a, all the atoms in the one-dimensional chain are periodically spaced with the spacing equal to c_1, referring to the average structure. A twofold superstructure corresponding to a doubled original unit cell can be generated by displacements of the atoms by equal distances in opposite directions, forming associated pairs or namely, a Peierls distortion (Figure 1-4b). The new unit cell (Figure 1-4c) can be described as a commensurately modulated superstructure, which still has long-range order and translational symmetry. The new lattice parameter $c_2 = 2c_1$. When the displacements are further distorted, such that the supercell lattice paremeter, c_2, is not an integer multiple of the original sublattice lattice parameter, c_1, an incommensurate modulation wave is produced (Figure 1-4d). Now, $c_1 = \gamma c_2'$, where γ is an irrational number, which means that no matter how many times the structure is extended, the supercell does not have translational symmetry.

The atomic displacements in the superstructure from the average structure can be in any direction or magnitude. Therefore, the modulation function can be characterized by a wave vector *q,* with the three basis vectors, a_1, a_2, and a_3 along the three crystallographic axes. *q* can be represented by the reciprocal basis vectors of the average structure.

$$q = \sigma_1 a_1^* + \sigma_2 a_2^* + \sigma_3 a_3^*$$

In the incommensurate modulated structures, either σ_1, σ_2, or σ_3 values are irrational numbers.

1.4.2 Incommensurate Composite Structure

Incommensurate composite structures, also refers to incommensurate intergrowth structures, defined as two or more periodic subsystems that together form an incommensurate aperiodic structure. Each subsystem is independent, and each of them has their own superspace group. The superspace group contains the information about both the symmetry of the lattice of the average structure and modulation wave vectors.

For instance, $[LaS]_{1.14}[NbS_2]$, one misfit layer compound, of which layers of composition NbS_2 alternatively stacked on LaS layers. Along the stacking orientation, the subsystems of LaS and NbS_2 share a common period; nonetheless, parallel to the layers of NbS_2 and LaS have their own lattice parameters, and the periodicities parallel to the layers are mutually incommensurate. The unit cell of NbS_2 subsystem has four formula units of NbS_2, whereas that of LaS has eight. The ratio of the two subsystem lattice parameters is an irrational number, approximately 0.57. For NbS_2 formula unit, this gives $0.57 \times 8/4 = 1.14$ per formula unit LaS (shown in Figure 1-5).

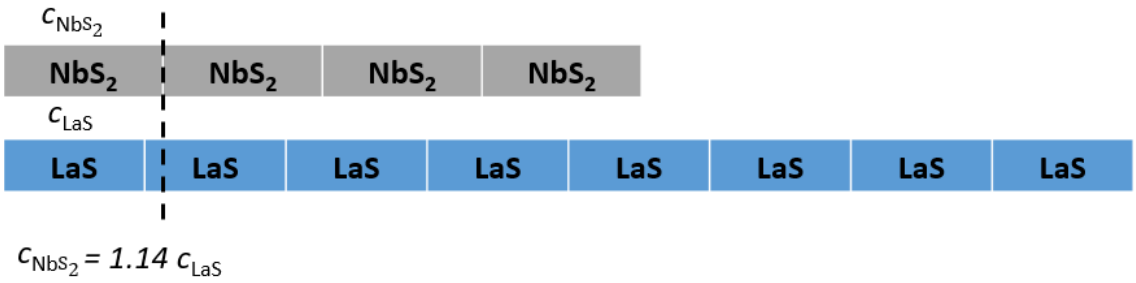

Figure 1-5: An illustration example of unit formula determination of an incommensurate composite structure compound, $[LaS]_{1.14}[NbS_2]$.

1.4.3 Thermoelectric materials with Incommensurate Structures

For example, Nowotny chimney-ladder compounds, T_mE_n (T_m, transition metals; E, group 13 to group 15 elements), usually possess narrow band gaps and large power factor. The compound $FeGe_\gamma$ ($\gamma \approx 1.52$) reveals an incommensurate chimney-ladder structure around 373 K, and it possesses a glass-like low lattice thermal conductivity of about 1 W m^{-1} K^{-1} at 373 K.[20] The maximum zT reaches 0.57 at 573 K with a lattice thermal conductivity of 1.26 W m^{-1} K^{-1}.[20] The Compound $(Mn_{1-x}Cr_x)Si_\gamma$ ($\gamma \approx 1.7$) with x = 0.20, achieves zT = 0.45 at 900 K with an approximate lattice thermal conductivity of 1.7 W m^{-1} K^{-1}.[21]

$ReSi_{1.75}$ adopts a commensurate structure of the with the $MoSi_2$ structure type, and Al doping renders an incommensurate structure. $ReSi_{1.675}Al_{0.10}$ reaches zT = 0.13 at 700 K, exhibiting a lattice thermal conductivity about 3 W m^{-1} K^{-1}.[22] Ge_xNbTe_2, with x is an irrational number, it crystallizes in an incommensurate structure with crystalline layers of $NbTe_2$ incommensurately modulated from one layer to the other. $Ge_{0.55}NbTe_2$ was demonstrated to have a maximum zT value of 0.12 at 650 K, with a lattice thermal conductivity of 2 W m^{-1} K^{-1}.[23]

1.5 Chalcogenide Thermoelectric materials

A substantial portion of the state-of-the-art TE materials are tellurides. The binary tellurides Bi_2Te_3 and PbTe, considered as traditional TEs, have been studied and utilized for decades. Telluride materials usually behave low thermal conductivity and high electrical conductivity,[24–28] which are both favorable for the TE energy conversion, benefiting from its larger heaviness and lower ionicity compared to other selenides and sulfides.[29–31]

1.5.1 Binary Chalcogenide Thermoelectric materials

The binaries Bi_2Te_3 and Sb_2Te_3 crystalize in layered structures, leading to anisotropic physical properties. Bi_2Te_3 is still the state-of-the-art TE material for cooling applications. The Bi_2Te_3 structure consists of close packed layers of cations and anions, stacked as …Te-Bi-Te-Bi-Te… along the *c* axis. The band gap of Bi_2Te_3 is about 0.16 eV, and the melting point is about 858 K.[32] Co-doping with the transition metal atoms Cu, Ag, and Cd yielded zT_{max} = 1.4 at 425 K.[33] Nanostructuring caused further improvements for Bi_2Te_3. Introducing nanostructures via recrystallization through hot-forging lowered the lattice thermal conductivity below κ_L = 0.5 W m^{-1} K^{-1}, from κ_L = 1.5 W m^{-1} K^{-1} for bulk Bi_2Te_3, which gave zT_{max} values at room temperature.[34] Bi_2Te_3 nanowires, as published in 2013, were also reported to exceed a zT = 2 at room temperature.[35] Compared to Bi_2Te_3, the thermoelectric performance of Sb_2Te_3 is a bit less attractive, but zT of nano-structured superlattices of Bi_2Te_3/Sb_2Te_3 can exceed 2.[36]

PbTe, once properly modified as both *n*- and *p*-type, exhibits outstanding thermoelectric properties at elevated temperatures, suitable for electricity generation from waste heat. PbTe-based thermoelectric generators have been used in several NASA space missions, from Transit 4

A to Viking 2, and in the Mars rover Curiosity.[37] PbTe crystallizes in the rock salt structure with a melting point of 1200 K, and is a semiconductor with a direct band gap of 0.32 eV.[38] Its highly symmetric crystal structure is the opposite of a complex crystal structure often postulated to be ideal for thermoelectric materials. In part, its relatively low lattice thermal conductivity of 2.2 W m^{-1} K^{-1} stems from its very high average molar mass of 167.4 g mol^{-1}. A re-investigation of the properties of the historic *n*-type PbTe revealed zT values ≈ 1.4 between 700 K and 850 K.[39] Introducing nanodomains caused a significant performance increase as reflected in a zT_{max} = 2.2 at 800 K for co-doped $AgPb_{18}SbTe_{20}$.[40,41] Kanatzidis coined this family LAST-*m*, standing for Lead Antimony Silver Telluride, with *m* being the amount of Pb per formula unit (18 in $AgPb_{18}SbTe_{20}$). Ag-Sb-rich nanodomains in an Ag-Sb-poor matrix significantly lowered the lattice thermal conductivity to κ_L ≈ 0.8 W m^{-1} K^{-1} at room temperature, compared to 2.2 W m^{-1} K^{-1} for PbTe.

Recent investigations have shown that SnSe, a lighter homologue of PbTe crystallizes in a strongly distorted NaCl variant, and can exhibit great thermoelectric properties as well. Despite its lower average molar mass of 98.8 g mol^{-1} compared to 167.4 g mol^{-1} in case of PbTe, its low thermal conductivity stems from a combination of strongly anharmonic and anisotropic bonding caused by the lone pair of electrons on Sn^{2+}, as reflected in its heavily distorted $SnSe_7$ polyhedron.[42] Measured on a single crystal along its *b* axis, a sensationally high zT_{max} = 2.6 was determined at 973 K.[43] Polycrystalline samples exhibit lower performance, for an example with a peak zT = 0.92 at 873 K,[44] and 1.36 at 823 K after solvothermal synthesis.[45]

The chalcocite Cu_2S occurs in three different modifications, depending on the temperature. The low temperature form, the *γ* phase, is monoclinic, which transforms into the hexagonal *β* form at 370 K. The superionic cubic *α* phase[46], thermodynamically stable above 700

K, is comprised of a face-centered cubic sublattice of S^{2-} ions, with the Cu ions located in many different positions with fractional occupancies. The latter is often described as a liquid-like sublattice. Various studies have consistently shown the lattice thermal conductivity being well below 0.8 W m^{-1} K^{-1}, despite the relatively low average molar mass of 53.1 g mol^{-1}.

An investigation varying *x* in $Cu_{2-x}S$ found peak performance for $Cu^{1.97}S$ with zT_{max} = 1.7 at 1000 K[47], a sensationally high value for a bulk sulfide. Using a melt-solidification technique, the performance was even further increased to zT_{max} = 1.9 at 973 K[48]. Poor stability of that $Cu_{1.97}S$ was observed during the electrical measurements because of the high and unrestricted ion mobility, however, Cu_2S and Cu_2Se form a solid solution over all S/Se ratios, which in part results in even lower thermal conductivity. Replacing small amounts of Se with S optimized (lowered) the charge carrier concentration of Cu_2Se via reduction of the Cu vacancies by the stronger Cu–S bonds, causing a *zT*= 2.0 at 1000 K in case of $Cu_2S_{0.08}Se_{0.92}$ after SPS[49]. $Cu_2S_{0.2}Se_{0.8}$ was reported to attain *zT*= 1.65 at 950 K after SPS, exhibiting a lattice thermal conductivity < 0.4 W m^{-1} K^{-1} throughout the whole temperature range[50]. An outstanding zT_{max} was obtained with an S/Se ratio of 1:1, namely *zT*= 2.3 at 1000 K in case of $Cu_{1.94}S_{0.5}Se_{0.5}$ after SPS. These samples are composed of different polymorphs on the mesoscale as well as various nanodomains.[51]

Alloying with Te and using the concept of nanoscale mosaicity via spark-plasma-sintering, *zT* was reported to reach 2.1 at 1000 K in the case of $Cu_2S_{0.52}Te_{0.48}$, with lattice thermal conductivity values being in the range of 0.3 W m^{-1} K^{-1} to 0.4 W m^{-1} K^{-1}.[52] The thermal conductivity and figure of merit plots are shown in Figure 1-6, along with those of Cu_2Se and Cu_2Te.

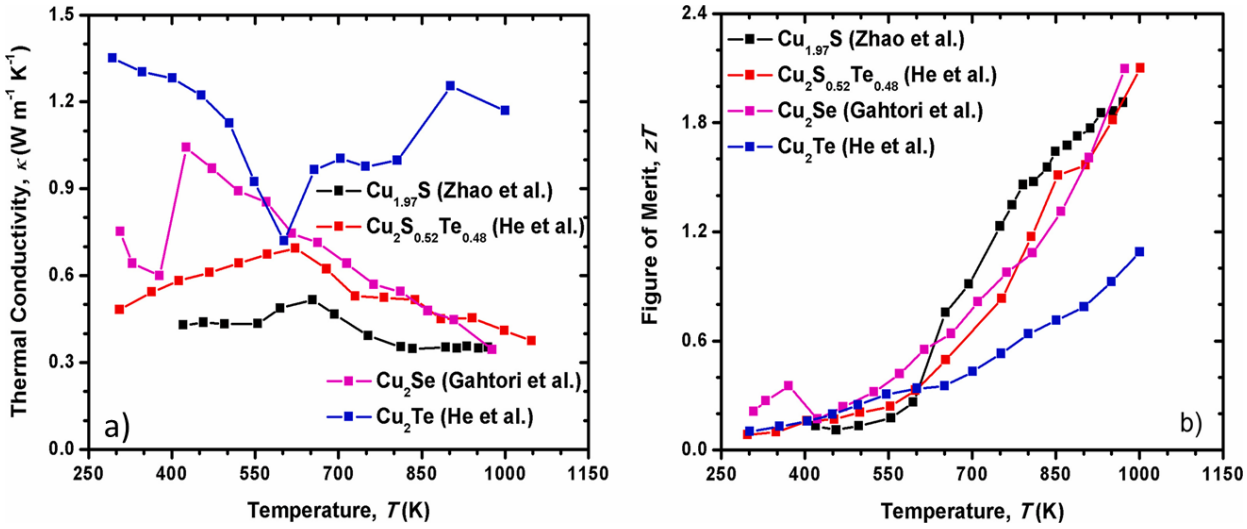

Figure 1-6: a) Thermal conductivity and b) figure of merit of the binary copper chalcogenides.

α-Cu_2Se undergoes a phase transition around 410 K into the fast ion conducting β form, wherein the Se atoms form a face-centered lattice with Cu atoms being kinetically disordered over various interstitial positions. Since 2012, various investigations have revealed high zT_{max} values from 973 K to 1000 K, including zT= 1.5 after traditional solid state synthesis[53], 1.6 after ball-milling[54], 1.8 after self-propagating synthesis[55], 1.8 after melt-quenching[56], and finally a zT_{max}= 2.1 after inclusions of defects on the nanoscale[57].

Cu_2Te has five different phases, and interestingly, Cu_2Te exhibits the lowest albeit still impressive thermoelectric performance of the binary copper chalcogenides. At the highest temperature, above 850 K, the cubic ε-phase persists, where the highest zT values are found. Undoped Cu_2Te was reported to only have a zT_{max} = 0.29 at 900 K, while Ag-doping led to a substantial enhancement of zT_{max}= 1.0 at 900 K.[58] Subsequently it was shown that similar if not superior values (a zT_{max} = 1.1 at 1000 K) can be achieved without Ag, namely via minimizing the carrier concentration.[59]

1.5.3 Ternary Chalcogenide Thermoelectric materials

Thallium tellurides have increasingly attracted attention since the report of (an extrapolated) zT_{max}= 1.2 for zone-melted Tl_9BiTe_6 in the year 2001, with an ultralow lattice thermal conductivity of κ_L= 0.4 W m^{-1} K^{-1}.[60] In contrast to PbTe and Bi_2Te_3, this material is bestowed with a complex crystal structure as a consequence of distorted coordination polyhedra around the thallium atoms, whereas Pb is surrounded by an ideal octahedron of six Te atoms in PbTe and Bi by an almost undistorted octahedron in Bi_2Te_3. This is a consequence of the stereochemically active lone pair of Tl^+. It should also be noted that Tl_9BiTe_6 contains over 56 atomic percent Tl, resulting in a higher averaged molar mass of 175.9 g mol^{-1}, compared to 167.4 g mol^{-1} for PbTe and 160.2 g mol^{-1} for Bi_2Te_3. Other substitution variants in polycrystalline form have matched or even exceeded this performance after optimizing the electron concentration, namely $Tl_9Bi_{0.98}Te_6$,[61] $Tl_{8.05}Sn_{1.95}Te_6$ and $Tl_{8.10}Pb_{1.90}Te_6$,[25] with zT_{max} values ranging from 1.1 to 1.4. Thallium silver tellurides also exhibit promising performance values because of the ultralow thermal conductivity; for example, $TlAg_9Te_5$ reaches zT_{max} at 700 K with a value of 1.23,[62] and Cu doped TlAgTe reaches zT_{max} = 0.6 at 575 K. Sn-doped Tl_9BiTe_6 shows competitive zT value, 0.95 at 500 K. $Tl_{10-x}Sn_xTe_6$ and $Tl_{10-x}Pb_xTe_6$, with x varying between 1.9 and 2.05 reached zT_{max} values of 1.26 and 1.46 at 685 K, respectively. Tl_2SnTe_5 also exhibits impressive high zT value, zT = 0.85 at 400 K, which is comparable to Bi_2Te_3.

Other silver containing telluride materials, namely $CsAg_5Te_3$, exhibits a high zT of 1.5 at 727 K and an extraordinarily low lattice thermal conductivity (0.18 W m^{-1} K^{-1}), due to its "cage rattling" crystal structure.[63] The figure-of-merit of Se doped $AgSbTe_2$ reaches a zT_{max} = 1.37 at

about 565 K as a *p*-type semiconductor.[44] Silver containing argyodite such as Ag_8GeSe_6, Ag_8SiSe_6, Ag_8SnSe_6, and silver containing tellurides Ag_8SiTe_6 and Ag_8GeTe_6 also represent promising thermoelectric candidates at high temperature due to their high ionic mobility and disorder induced by silver ion migration. Their thermoelectric properties are summarized in Table 1-1.

Table 1-1: A thermoelectric performance summary of silver containing chalcogenides

Material	**Type**	**κ_L (W m^{-1} K^{-1}) at T**	**zT_{max} at T**	**Reference**
$Ag_8GeSe_{5.88}$	*n*	0.35 at 900 K	0.55 at 900 K	[64]
Ag_8GeTe_6	*p*	0.30 at 703 K	0.48 at 703 K	[65]
Ag_8SnSe_6	*n*	0.20 at 900 K	1.20 at 900 K	[66]
Ag_8SiTe_6	*p*	0.31 at 800 K	0.49 at 800 K	[67]
Ag_8SiSe_6	*n*	0.30 at 340 K	0.75 at 340 K	[68]

1.6 Scope of This Thesis

Prior to this work, thallium tellurides have shown low thermal conductivity and promising TE properties, such as TlAgTe,[69] $TlAg_9Te_5$,[62] and Tl_2SnTe_5[24] due to their heavy molar masses and complex structures. The reported $Tl_4Ag_{24-x}Te_{15-y}$ crystal structure possessed an impossibly short Te-Te distance[1], so the initial investigation started with solving the appropriate structural model for this material. Additionally, there is no thermoelectric data for this material, and it is more interesting to explain its excellent TE performance originating from its composite misfit structure. $Tl_4Ag_{18}Te_{11}$ was reported to be a structure with some disordered Tl sites rattling in the cuboctahedral voids[70], and cage rattling structure was reported to help reduce the lattice thermal

conductivity, such as the filled skutterudites[71–73] and clathrates.[4,74,75] Herein, investigating the thermal conductivity of $Tl_4Ag_{18}Te_{11}$ is able to provide more information about the relationship between rattling atoms in crystal structures and lattice thermal conductivity. $TlSbTe_2$ also attracted our interest because of its anisotropic structure and high TE performance[76], we wanted to examine whether this compound possesses anisotropic electrical properties and further improve its *zT* by optimizing the carrier concentration.

Chapter 2: Experimental Procedures

2.1 Synthesis Procedures

All starting materials were stored in an argon-filled MBRAUN glove box, assuring the oxygen and moisture contents inside below 0.6 and 0.1 ppm, respectively. The starting materials were weighed based on the stoichiometric ratios and loaded into a silica tube. The tubes containing the elements were then transferred to a vacuum line and evacuated to at least 2.4×10^{-3} mbar, followed by being sealed utilizing a hydrogen and oxygen flame. Next, the sealed tubes were transferred into resistance furnaces. The details about the temperature program will be described in each chapter.

The as prepared ingots were manually ground into fine powder, and the powder was then sintered under a 5% hydrogen + 95% argon atmosphere employing an Oxy-Gon FR-210-30T-ASA-160-EVC hot press furnace system in a hardened graphite die with an inner diameter of 12.7 mm. The detailed temperature and pressure profiles will be stated in each chapter.

The density of the pressed pellet, ρ_D, was determined by the Sartorius YDK01 density determination kit based on the Archimedean principle. Due to the buoyant force, the weight of an object soaked in the fluid (m_f) reveals a lower value than in the air (m_a). Assuming the density of the fluid is ρ_f, then ρ_D is given by

$$\rho_D = \frac{m_a \times \rho_f}{m_a - m_f}$$

In this thesis, water is used as the fluid, and the air under standard conditions is assumed as 0.0012 g/cm^3. Thus, the formula used after correcting the errors of air buoyancy is derived by

$$\rho_D = \frac{m_a \times (\rho_f - 0.0012\ g/cm^3)}{m_a - m_f} + 0.0012 g/cm^3$$

2.1.1 Phase Diagrams

Phase diagrams can be applied as a useful tool to determine the solid state synthesis process. A peritectic reaction usually requires a quenching followed by an annealing below the peritectic point to achieve a pure modification of the sample. In contrast, a eutectic reaction does not have that requirement, but is often performed with a slow cooling to obtain high quality crystals.

2.2 Characterization

The wavelength of X-rays is between 0.01 nm and 10 nm, and it is one of the important tools for material characterization. X-rays can interact with the electrons elastically or inelastically. When a photon strikes an electron that is tightly bound with the core, an elastic collision occurs where the electron stays at the same position. The scattered photon wave possesses the same energy as the incident wave, which is referred to as a coherent scattering process, or diffraction. Diffraction patterns can reveal information about the atom's position. Single crystal and powder diffractometers allow for structure determination of materials. However, in an incoherent scattering process, or Compton scattering, the incident X-ray loses energy and changes direction, and the lost energy is converted into the kinetic energy of the electrons. The wavelength of the

incoherently scattered photons is longer than that of the incident waves because of the lower energy.

Diffraction techniques is usually not enough for revealing the whole structural information, so electron microscopy is widely used to remedy the insufficiency. Electron microscopes are designed based on either transmission or reflection. The specimen detected by a transmission electron microscopy (TEM) has a restrict thickness requirement, usually thinner than 200 nm, because electrons cannot penetrate through thick particles. With reflection instruments, such as scanning electron microscopy (SEM), the specimen thickness is no longer an issue, so the sample preparation criteria are easier. If the sample has poor electrical conductivity, a thin layer metal coating must be applied to avoid charge accumulation on the surface. SEM can be applied with the combination of energy dispersive spectroscopy (EDX) to provide more valuable information about the elemental topography and sample composition.

2.2.1 Powder X-ray Diffraction

The phase purity of all samples in this thesis was verified by an INEL® X-ray powder diffractometer with a position-sensitive detector and Cu Kα1 X-ray radiation source with a wavelength of 1.540598 Å, under the acceleration voltage and current of 30 kV and 30 mA, respectively. The powder X-ray diffraction (PXRD) patterns were collected at room temperature in air atmosphere, with a 2ϑ between 5° and 120°.

The fundamental principle of PXRD is presented in Figure 2-1. When an X-ray beam hit a crystal in which atoms are periodically arranged with an incident angle of ϑ, a diffracted beam is emitted also with angle of ϑ. The waves of the emitted photons can interfere with each other,

leading to both constructive and destructive interference in various orientations. In the selected orientations, the constructive interferences are collected, which then are plotted as a function of angle. In terms of the Bragg's law, the variance in the path length of two diffracted beam should equal to an integer multiple (n) of the wavelength (λ), which satisfies the requirements to generate constructive interference.

$$n\lambda = 2d_{hkl}\sin\vartheta$$

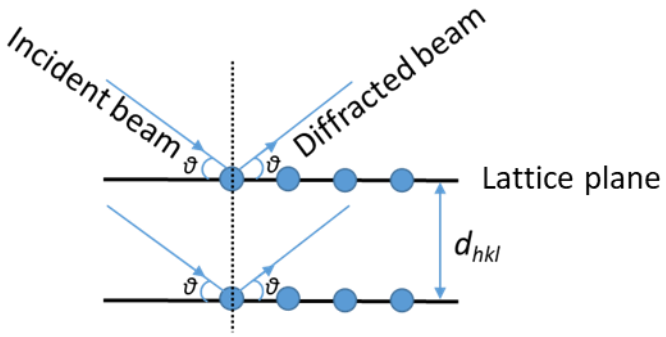

Figure 2-1: The illustration of the Bragg's law.

The atomic plane distance, d_P, is derived by

$$\frac{1}{d_{hkl}^2} = \frac{h^2}{a^2} + \frac{k^2}{b^2} + \frac{l^2}{c^2}$$

where, a, b, c are lattice parameters; h, k, l are the Miller indices.

The intensity of the radiation scattered is given by the Thomson equation:

$$I_P \propto \frac{1}{2}(1 + cos^2 2\theta),$$

where I_P is the scattered intensity at any point, P. Based on this equation, one can see that the highest intensity occurs when parallel or antiparallel to the incident beam. The Thompson

equation is also known as the polarization factor, and it is widely used during the angular correction processing of intensity data.

Each element has a different scattering power factor, *f*, which is proportional to the atomic number, Z, and decreases with increasing Bragg angle, θ. Then, an individual diffracted wave by atom *j* can be represented by the form

$$F_j = f_j (\cos \delta_j + i \sin \delta_j) = f_j e^{i\delta j}$$

where δ is the phase given by $\delta = 2\pi (hx + ky + lz)$. The summation of a unit cell then can be carried out by the structure factor, F_{hkl}.

$$F_{hkl} = \sum_j f_j (cos\delta_i + sin\delta_i)$$

The structure factor can be classified as observed one F_{hkl}^{obs} and calculated one F_{hkl}^{cal}. The level of agreement between these two values is defined by the residue factor, *R*.

$$R = \frac{\sum \left| |F_{hkl}^{obs}| - |F_{hkl}^{cal}| \right|}{\sum |F_{hkl}^{obs}|}$$

The lower the *R* value, the more likely the structure is correct, in solving an unknown crystal structure. A typical magnitude of *R* to ensure the correctness of the structure is lower than 0.1.

Here, the Rietveld refinements are implemented by the General Structure Analysis System (GSAS)[46] via the graphical interface EXPGUL[77].

2.2.2 Single Crystal X-ray Diffraction

Single crystal X-ray diffraction is applied to determine the unit cell and space group of the compound. The single crystal information obtained in this thesis was obtained using a Bruker APEX II diffractometer, with a Mo Kα (λ = 0.71073 Å) X-ray radiation. The collected data were analyzed by the APEXII package software developed by the Bruker® company. The data collected were processed by the program SHELXTL[78], to derive the diffracted beams into the real lattice information. The goodness of the refinement is weighed by the *R* factor (*R*1) and weighted *R* factor (*wR*2), where *wR*2 is calculated by

$$wR2 = \sqrt{\frac{\sum w(F_{hkl}^{obs^2} - F_{hkl}^{cal^2})^2}{\sum w(F_{hkl}^{obs^2})^2}}$$

with *w* is the weighting parameter. Incommensurate composite superstructure models were refined by JANA2006 package.[79]

2.2.3 Scanning Electron Microscopy and Energy Dispersion X-Ray Spectroscopy

SEM works in a resolution range of 10^{-2} to 10^{2} μm. In this thesis, the SEM was performed by an FEI Quanta Feg 250 ESEM (with EDX) under an acceleration voltage of 20 kV. The SEM is composed of a vacuum system, a high energy electron source, and a detector. SEM requires an evacuated working environment, not only because the filament will be quickly burnt out in air, but also because the electrons may collide with the gas molecules resulting in lower quality of the image. The fundamental principles of SEM utilize the interactions between accelerated electrons and the sample, producing various types of signals such as secondary electron signal, Auger electron signal, backscattered electron signal or X-ray signal.

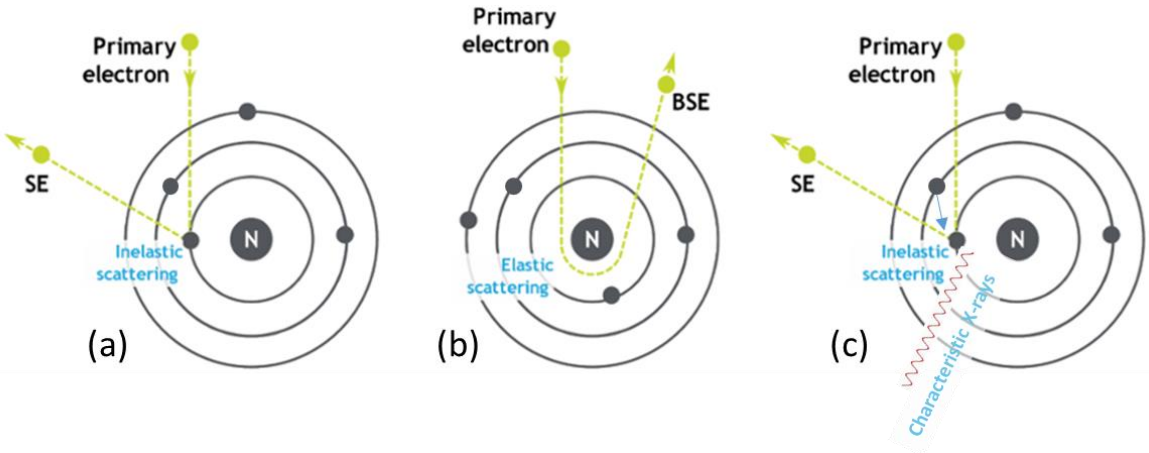

Figure 2-2: Graphic demonstration of the generation of (a) secondary electrons, (b) backscattered electrons, (c) characteristic X-rays.

When high energy radiation hits matter, it can result in different products, as shown in Figure 2-2. Secondary electrons (SE) are produced when electrons in the sample are ejected by the primary radiation with sufficient energy that exceeds the ionization potential, which is an inelastic scattering process, illustrated in Figure 2-2a. Secondary electrons are generally low in energy (below 50 eV), so they can be easily absorbed. Consequently, the secondary electron detector can only collect the signal from the surface of the sample, which is more favorable to revealing the topographic information of the specimen. Whereas backscattered electrons (BSE) originate from an elastic scattering event due to the interactions between the nuclei and the primary radiation, demonstrated in Figure 2-2b. Backscattered electrons generally possess high energy and travel through the deep area of the sample, providing more useful data on the sample's composition.

When a secondary electron is generated as mentioned above, a vacancy is formed, and another electron from outer shell that has higher energy will jump to the vacancy. The energy difference between the inner shell and outer shell, as a result, can be offset by releasing an X-ray

of the corresponding energy difference. Different elements have specific energy differences between the shells, so measuring the energies of these emitted X-rays allows the detection of elemental distribution in the sample.

2.3 First Principle Calculations

Computational electronic structures were determined by density functional theory (DFT) in order to predict and understand the properties of materials in more depth. The purpose of DFT is to replace the wave function with electron density as the basic quantity of research. The multi-electron wave function has 3*N* variables (*N* is the electron number, and each electron contains three spatial variables). However, electron density only possesses a function of three variables, which is more convenient in both concept and practice.

The earliest form of approximation to the exchange-correlation energy functional in DFT is based on the relationship between the energy of free electron gas and the density, which is called local-density approximation (LDA). Nonetheless, the electron density is not uniform, because the electrons are not totally free (including the interaction between electrons and the interaction between nucleus and electrons). For the periodic systems, the electron density is approximate to be uniform, so the LDA assumption is quite successful in this case.

In this research, the nonempirical, Perdew-Burke-Ernzerhof (PBE) generalized gradient approximation (GGA) is the main method that was employed.[80] This PBE function belongs to the hybrid functional method, which mixes exact exchange with density functional approximations to exchange-correlation. Additionally, the Tran-Blaha modified Becke-Johnson (mBJ) potential was also employed for more accurate band gap calculations.[81] mBJ potential uses the semilocal

exchange potential which adds corrections of the screening effect to the local approximation of the exact exchange potential. All the band structure and density of states (DOS) calculations were performed by the Wien2k package[82] in this thesis.

2.4 Physical Property Measurements

2.4.1 Thermodynamic Measurements

Both differential scanning calorimetry (DSC) and thermogravimetry (TG) were conducted by a Netzsch STA 409 PC Luxx under a constant argon flow using sapphire as the reference. Decomposing points, melting points and phase transitions that occurred as temperature increased were studied through analyzing the data obtained by DSC. The obtained decomposing temperature and melting temperature are able to assist in determining the hot press conditions, in order to obtain denser pellets before decomposing.

2.4.2 Electrical Conductivity and Seebeck Coefficient Measurements

. The electrical conductivity and the Seebeck coefficient were measured by a ULVAC-Riko® ZEM-3 instrument under an ultrapure helium atmosphere. The samples were cut into a rectangular prism shape with an approximate dimension of 10 × 2 × 2 mm. As illustrated in Figure 2-3, the bar is set in a vertical position between two electrodes, where the side contacts two *R*-type thermocouples. In the measurement, a constant current (*I*) and a heat from the bottom electrode are provided, with two thermocouples detecting the voltage (*dV*) and temperature differences (*dT*). As a result, the Seebeck coefficient can be determined by

$$S = dV/dT$$

The resistance of the area between the two thermocouples in the sample, *R*, can be calculated by

$$R = dV/I$$

In addition, based on Ohm's law, the electrical resistivity (ρ), and the electrical conductivity (σ) are determined by

$$\rho = 1/\sigma = R \cdot A/d$$

where *A* is the surface area of the specimen, and *d* the length between the two thermocouples. This four-point electrical conductivity measurement method can avoid the error caused by the contacting resistance. The experimental error margin for *S* and σ are estimated as $\pm$3% and $\pm$5%, respectively.

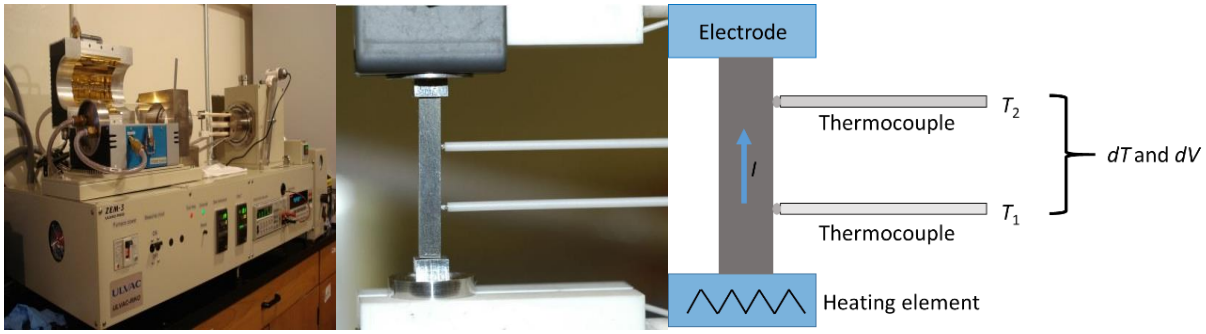

Figure 2-3: Overview of ZEM-3 instrument and schematic demonstration of its working principle.

2.4.3 Thermal Conductivity Measurements

Thermal diffusivity (*D*) was measured on hot pressed pellets with a diameter of 12.7 mm and heights approximating 2 mm, utilizing a TA®-instruments LASERFLASH DLF-1200 system under an ultrapure argon atmosphere. This instrument qualifies *D* utilizing the flash method which can be implemented at high temperatures and minimize the heat loss by reducing the

measuring duration. The sample pellets are pre-coated with a thin layer of colloidal graphite in order to achieve an even sample surface, a homogeneous heating, and a better absorption and emissivity. A laser provides an instantaneous energy pulse to the bottom face of the disc, and an infrared detector stands above the upper face to register the temperature change with time after each laser pulse. The equation to determine *D* is expressed as

$$D = 0.1388 \frac{{L_D}^2}{t_{1/2}}$$

with L_D referring to the thickness of the measured disk, and $t_{1/2}$ the time to reach half of the maximum temperature. Then, the thermal conductivity is derived by

$$\kappa = D\, c\, \rho_D$$

where ρ_D represents density of the pellet, and *c* the heat capacity. High temperature *c* is usually estimated through the Dulong-Petit law, where R defines the gas constant and *M* the average molecular mass of the material chemical composition.

$$c = 3R/M$$

The experimental error range for κ is approximated as $\pm$5%.

The overall error range for *zT* is postulated as $\pm$10%.

Chapter 3: Thermoelectric Properties of $Tl_2Ag_{12}Se_7$

3.1 Introduction

At first the new selenide introduced with this contribution, $Tl_2Ag_{12}Se_7$, appeared to be isostructural with $K_2Ag_{12}Se_7$[83] and $K_2Ag_{12}Te_7$[84] ($Zr_2Fe_{12}P_7$ type),[85] or with $Tl_4Ag_{24-x}Te_{15-y}$,[1] based on its very similar X-ray powder diagram. However, our single crystal structure studies revealed that it actually crystallizes in a √3 × √3 × 1 super cell of the $Zr_2Fe_{12}P_7$ type, while $Tl_4Ag_{24-x}Te_{15-y}$ was reported to adopt a 1 × 1 × 2 super cell of the $Zr_2Fe_{12}P_7$ type. Like many of the above-mentioned thallium chalcogenides, this material is bestowed with a very low thermal conductivity.

This Chapter was published as a *pnp* semiconducting transition behavior due to an artifact of the measurement device. Subsequent high temperature X-ray photoelectron spectroscopy (XPS) investigations into the phase transition did not reveal any obvious changes to the electronic states of any element, indicating that no *pnp* transition occurred. Upon further inspection, the raw data collected from the ULVAC® ZEM-3 instrument exhibited positive Seebeck values at all temperatures, but the voltage difference versus temperature difference exhibits an inversely proportional relationship. Therefore, the slope (i.e. Seebeck coefficient) was erroneously determined to switch from *p*- to *n*-type and back.

3.2 Experimental Procedures

The synthesis began from the elements, stored in an argon filled glovebox. The elements were used as acquired: Tl, granules, 6 mm, 99.99%, Alfa Aesar; Ag, shots, 99.99%, Strem Chemicals; Se, pellets, <5 mm, 99.99%, Sigma-Aldrich. The ternary selenide was first synthesized starting from the elements in the molar ratio of 4:22:15 Tl : Ag : Se, for a total amount of approximately 500 mg. This ratio was chosen to investigate whether the Se analog to $Tl_4Ag_{24-x}Te_{15-y}$ ($x = 2$, $y = 0$) exists. The tube was placed into a resistance furnace, and then heated to 1023 K within 20 h, kept at 1023 K for 10 h, and thereafter slowly cooled over 100 h to room temperature to obtain crystals for a single crystal analysis.

The obtained X-ray diffraction pattern, collected at room temperature for 60 min in the 2ϑ range from 5° to 120°, strongly resembled the one calculated from the published model for $Tl_4Ag_{24-x}Te_{15-y}$.[1] After successful structure solution and refinement, we obtained the formula $Tl_2Ag_{12-x}Se_7$ with $x = 0.14(2)$. To verify whether or not deficiencies on the Ag sites are always present, we repeated this reaction with a ratio of 2:12:7 Tl : Ag : Se. No side product peaks were detected in the X-ray powder pattern (Figure 3-1), and a second single crystal structure study revealed no significant differences, resulting in the formula $Tl_2Ag_{12-x}Se_7$ with $x = 0.16(2)$.

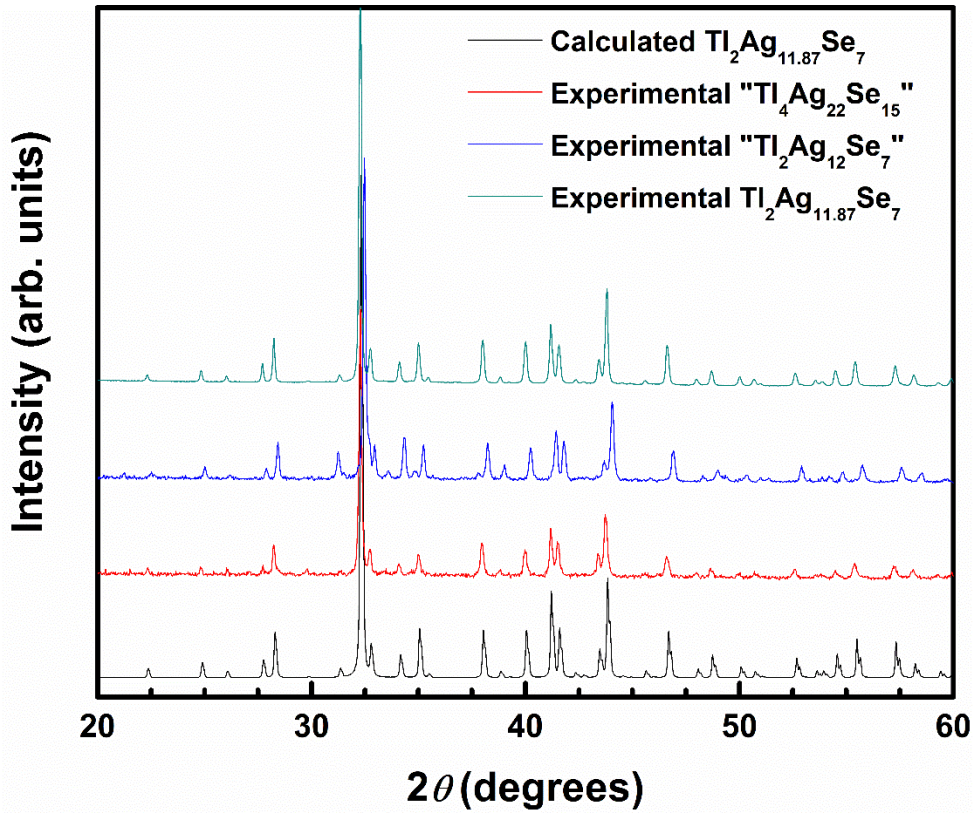

Figure 3-1: Powder X-ray diffraction patterns of $Tl_2Ag_{12}Se_7$.

Next, several grams of a sample of the nominal composition "$Tl_2Ag_{11.86}Se_7$" were prepared for the physical property measurements. Again, no side products were identified in any of the X-ray powder diagrams obtained from these reactions

Data collections were carried out at room temperature on a Bruker Smart Apex CCD and a Bruker Kappa Apex II CCD, respectively, utilizing Mo Kα radiation. The plate-like-shaped black crystals were selected under an optical microscope and attached to a very thin glass fiber via epoxy glue. After the determination of preliminary unit cells, the data were collected by scanning ω and φ of 0.3° in different sets of frames for full data coverage and low redundancy, using the search strategy part of the APEX II suite. The exposure time was 60 s per frame.

In contrast to the related selenides $K_2Ag_{12}Se_7$ (space group $P6_3/m$)[83] and $K_2Ag_{12}Se_{7.11}$ (space group $P6_3$),[86] both synthesized via solvothermal methods, no systematic absences were observed, which stands against this structure having a 6_3 screw axis as well. The structure was solved in the space group $P\bar{3}$, employing the direct method, and refined using the least-squares procedure of the SHELXTL package. The tidy routine of the Platon program package[87] was utilized to standardize the atomic positions. Its addsymm part was applied to identify potential additional symmetry elements; none were found.

Since the Ag sites in many silver chalcogenides exhibit various deficiencies, we tentatively refined the occupancies of all six Ag sites. Three thereof remained at full occupancy (99–100%) within two standard deviations, and the other three had occupancies of 97–98%; i.e., the deficiencies were larger than three standard deviations. This resulted in the refined formula $Tl_2Ag_{11.86(2)}Se_7$. To analyze whether or not these deficient Ag sites may be fully occupied, we repeated the procedure from a sample of nominal composition "$Tl_2Ag_{12}Se_7$", corresponding to six fully occupied Ag sites. In this case, we refined the Ag site occupancies to be equal to those of $Tl_2Ag_{11.86(2)}Se_7$ within error, resulting in $Tl_2Ag_{11.84(2)}Se_7$. Finally, we used the structure model of $K_2Ag_{12}Se_{7.11}$ for a tentative refinement in $P6_3$, but then multiple problems occurred in the linear Se atom chains. Crystallographic data are summarized in Table 3-1, atomic positions are listed in Table 3-2, and selected bond distances are given in Table 3-3.

Table 3-1: Crystallographic details of $Tl_2Ag_{11.86}Se_7$.

Formula	**$Tl_2Ag_{11.86(2)}Se_7$**	**$Tl_2Ag_{11.84(2)}Se_7$**
FW	2241.16	2238.86
Crystal System	trigonal	trigonal
Space Group	$P\bar{3}$ (No. 147)	$P\bar{3}$ (No. 147)
***a, c* (Å)**	18.9153(18), 4.3783(4)	18.910(3), 4.3769(8)
***V* (Å^3)**	1356.6(2)	1355.5(5)
Z	3	3
Density (g cm^{-3})	8.230	8.228
Absorption Coefficient (mm^{-1})	44.324	44.339
***F*(000)**	2873	2870
Crystal Size (mm)	0.04 × 0.04 × 0.01	0.06 × 0.04 × 0.05
Temperature (K)	296(2)	296(2)
Radiation (Å)	0.71073	0.71073
Total, Unique Data, *R*(int)	7783, 2651, 0.0483	9637, 2637, 0.0530
Observed Data [I > 2σ(I)]	1553	1333
No. of Reflections, Parameters	2651, 100	2637, 100
***R*(F_o),[a] *R_w*(F_o^2),[b] GOF (obs. Data)**	0.0492, 0.0938, 1.163	0.0592, 0.0914, 1.277
min., max. residual electron density [e Å^{-3}]	-2.992, 5.191	-2.943, 6.006

[a] $R(F_o) = \Sigma||F_o|-|F_c|| / \Sigma|F_o|$; [b] $R_w(F_o^2) = [\Sigma[w(F_o^2 - F_c^2)^2] / \Sigma[w(F_o^2)^2]]^{1/2}$, with F_o and F_c being the observed and calculated structure factors, respectively.

Table 3-2: Fractional atomic coordinates and equivalent isotropic displacement parameters and occupancies of $Tl_2Ag_{11.86}Se_7$.

	x	*y*	*z*	U_{eq}/Å^2	*occ*
Tl1	0.33357(3)	0.00000(3)	0.25103(3)	0.03154(16)	1
Ag1	0.06808(8)	0.56432(8)	0.2361(3)	0.0441(3)	1
Ag2	0.13091(10)	0.00672(8)	0.2257(3)	0.0562(6)	0.980(6)
Ag3	0.16268(8)	0.26496(8)	0.2795(3)	0.0441(3)	1
Ag4	0.20780(9)	0.53418(10)	0.2778(3)	0.0552(6)	0.971(6)
Ag5	0.40134(8)	0.23077(8)	0.2172(3)	0.0439(3)	1
Ag6	0.54206(10)	0.20183(10)	0.2656(3)	0.0582(6)	0.981(6)
Se1	0.23834(8)	0.17650(8)	0.2305(2)	0.0246(3)	1
Se2	0.27117(8)	0.42824(8)	0.2744(2)	0.0240(3)	1
Se3	0.60476(8)	0.09475(8)	0.2582(2)	0.0241(3)	1
Se4	1/3	2/3	0.0098(7)	0.0463(7)	1
Se5	0.0000	0.0000	1/2	0.0426(9)	1

Table 3-3: Interatomic distances (Å) of $Tl_2Ag_{11.86}Se_7$.

Tl1–Se2	3.3212(12)	**Ag5–Se3**	2.7029(18)
Tl1–Se1	3.3414(13)	**Ag5–Se1**	2.7199(18)
Tl1–Se3	3.3586(17)	**Ag5–Se2**	2.7468(17)
Tl1–Se2	3.4109(16)	**Ag5–Se2**	2.8048(17)
Tl1–Se1	3.4457(13)		
Tl1–Se3	3.4649(12)	**Ag6–Se4**	2.708(2)
		Ag6–Se2	2.7541(17)
Ag1–Se2	2.7030(18)	**Ag6–Se3**	2.8130(19)
Ag1–Se3	2.7178(18)	**Ag6–Se2**	3.020(2)
Ag1–Se3	2.7613(17)		
Ag1–Se3	2.8006(17)	**Ag1–Ag4**	2.9750(19)

		Ag1–Ag6	3.1388(18)
Ag2–Se5	2.6973(14)	**Ag1–Ag6**	3.149(2)
Ag2–Se1	2.7447(17)	**Ag1–Ag1**	3.250(2)
Ag2–Se1	2.8137(19)		
Ag2–Se1	3.035(2)	**Ag2–Ag3**	2.9800(19)
		Ag2–Ag2	2 × 3.121(2)
Ag3–Se1	2.6998(18)	**Ag2–Ag3**	3.132(2)
Ag3–Se2	2.7225(18)	**Ag2–Ag3**	3.1631(18)
Ag3–Se1	2.7449(17)		
Ag3–Se1	2.8136(17)	**Ag3–Ag5**	3.3195(18)
		Ag3–Ag5	3.3389(18)
Ag4–Se4	2.7101(19)		
Ag4–Se3	2.7588(17)	**Ag4–Ag5**	3.121(2)
Ag4–Se2	2.8027(19)	**Ag4–Ag6**	2 × 3.150(2)
Ag4–Se3	2.999(2)	**Ag4–Ag5**	3.1510(18)
		Ag5–Ag6	2.981(2)

The calculation on $Tl_2Ag_{12}Se_7$ (assuming fully occupied Ag positions) was performed with 120 independent *k* points of the first Brillouin zone on a grid of 6 × 6 × 24 *k* points along the respective vectors of the reciprocal lattice, with the convergence criterion of the energy change being less than 0.0001 Ry.

The thermal behavior of $Tl_2Ag_{11.86}Se_7$ was investigated on a ground sample of approximately 30 mg by differential scanning calorimetry (DSC) and thermogravimetry (TG) using the NETZSCH® STA 409 PC Luxx instrument. The experiment was carried out under a constant argon flow with a heating rate of 20 K/min up to 823 K using sapphire as reference sample. The

densifying was performed at 623 K under 70 MPa for 6 h, resulting in a density of 98% of the theoretical density.

All XPS measurements were collected using a Kratos (Manchester, UK) AXIS Supra system at the Saskatchewan Structural Sciences Centre (SSSC). This system is equipped with a 500 mm Rowland circle monochromated Al Kα (1486.6 eV) source and combined hemi-spherical analyzer (HSA) and spherical mirror analyzer (SMA). A spot size of hybrid slot (300 x 700 microns) was used. All survey scan spectra were collected in the -5 – 1200 eV binding energy range in 1 eV steps with a pass energy of 160 eV. High resolution scans of 4 regions were also conducted using 0.05 eV steps with a pass energy of 20 eV. An accelerating voltage of 15 keV and an emission current of 15 mA were used for the analysis. All scans were performed at room temperature (25°C), 90°C, 135°C, 160°C and room temperature (25°C) at the end after the heating experiments were performed.

New low temperature Seebeck coefficient and electrical conductivity was measured by a PPMS from Quantum Design.

3.3 Results and Discussion

The room temperature crystal structure of $Tl_2Ag_{12}Se_7$ is depicted in Figure 3-2. As a variant of the $Zr_2Fe_{12}P_7$ type adopted by $K_2Ag_{12}Se_7$ and $K_2Ag_{12}Te_7$, it features a three-dimensional tunnel structure constructed by covalently bound $AgSe_4$ tetrahedra, whose tunnels are filled by Tl atoms.

Because of the √3 × √3 super cell in the *a*,*b* plane, each unit cell of $Tl_2Ag_{12}Se_7$ is comprised of two symmetry inequivalent—yet topologically equivalent—clusters. These clusters are both centered

by a chain of Se atoms, Se4 and Se5, running along [1/3, 2/3, *z*] and [0, 0, *z*]. These two Se sites, highlighted in red in Figure 3-3, are each octahedrally coordinated by six Ag atoms.

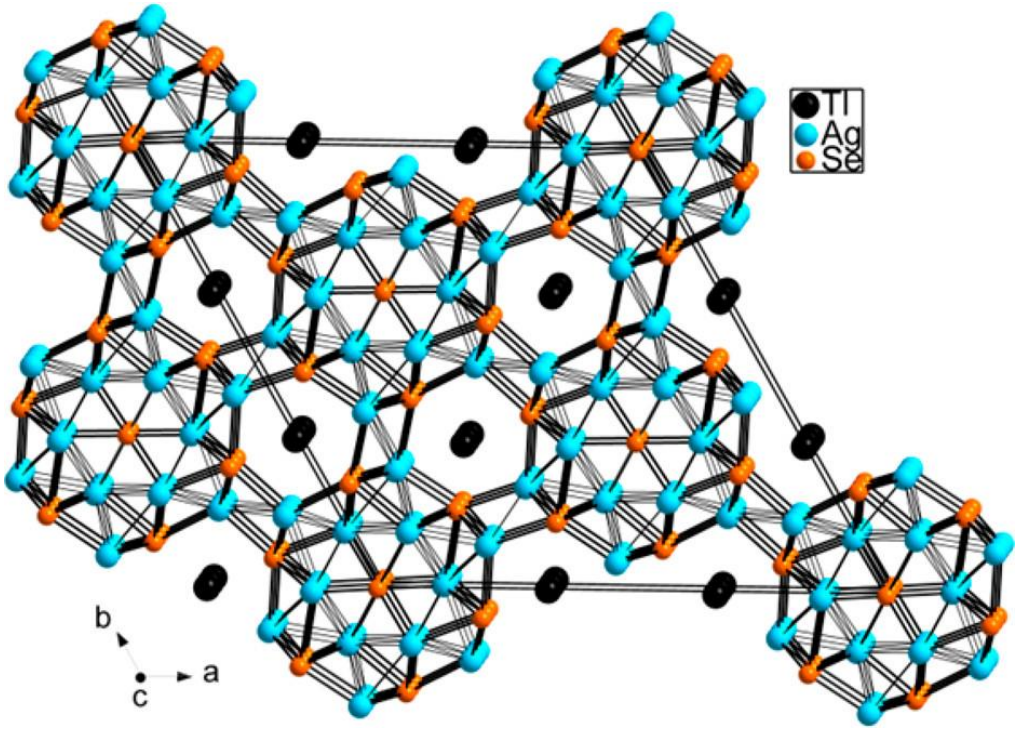

Figure 3-2: Crystal structure of $Tl_2Ag_{12}Se_7$.

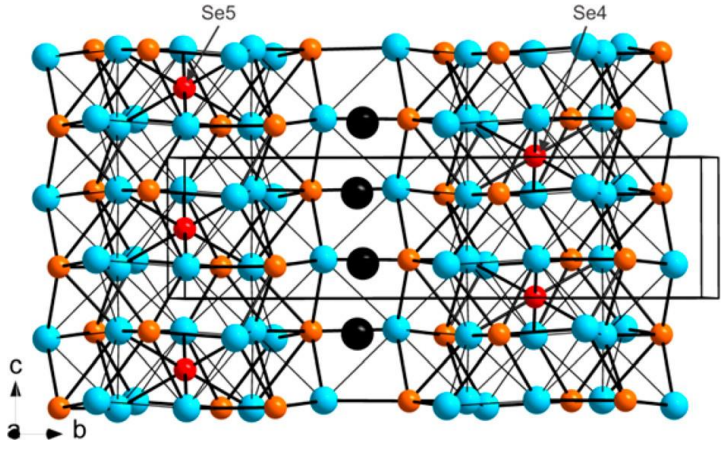

Figure 3-3: Two independent chains of Se-centered clusters of $Tl_2Ag_{12}Se_7$.

The structure of $K_2Ag_{12}Se_{7.11}$ is topologically equivalent in a view down the *c* axis, but exhibits strongly disordered Se atoms in those linear chains with a small but significant Se excess.

On the other hand, the telluride (and $Zr_2Fe_{12}P_7$) has only one such cluster, and thus only one independent chalcogen chain per unit cell.

All Ag atoms are tetrahedrally coordinated by Se atoms in the structure of $Tl_2Ag_{12}Se_7$, with Ag–Se distances varying between 2.70 and 3.04 Å. As a consequence of the edge condensation of the $AgSe_4$ tetrahedra, numerous Ag–Ag contacts of 2.98–3.16 Å occur. Such d^{10}–d^{10} Ag–Ag interactions are quite common in Ag selenides, and typically of bonding character, as discussed in the case of $Tl_2NdAg_3Se_4$.[88]

The Tl atoms are coordinated to six Se atoms at distances of 3.32–3.46 Å forming a trigonal prism, with the shortest Tl–Tl distances being >4 Å along the *c* axis. These Tl–Se distances are typical for thallium selenides, which often also comprise Tl–Tl contacts shorter than 3.7 Å. [88] The lack of such secondary contacts is likely a consequence of the small Tl content of less than 10 at. % in this structure and may enable a substitution of Tl with alkali metal atoms, in contrast to more Tl-rich chalcogenides such as $Tl_2NdAg_3Se_4$, [88] Tl_9BiTe_6,[60] and $Tl_{10-x}Sn_xTe_6$ and $Tl_{10-x}Pb_xTe_6$.[25] Thusly, both $K_2Ag_{12}Se_7$[83] and $K_2Ag_{12}Se_{7.11}$[86] adopt similar yet different structures wherein the K atoms are also forming a linear chain of KSe_6 trigonal prisms.

Since there are no Se–Se contacts shorter than 4 Å, we can assign the typical oxidation states of Tl^+, Ag^+, and Se^{2-}, resulting in the balanced formula $(Tl^+)_2(Ag^+)_{12}(Se^{2-})_7$. Thus, the stoichiometric material appears to be an intrinsic semiconductor, which is confirmed by the density of states (DOS), presented in Figure 3-4, revealing a (calculated) band gap of 0.5 eV. It should be noted, however, that this calculation method usually results in smaller band gaps, compared to experimental methods.

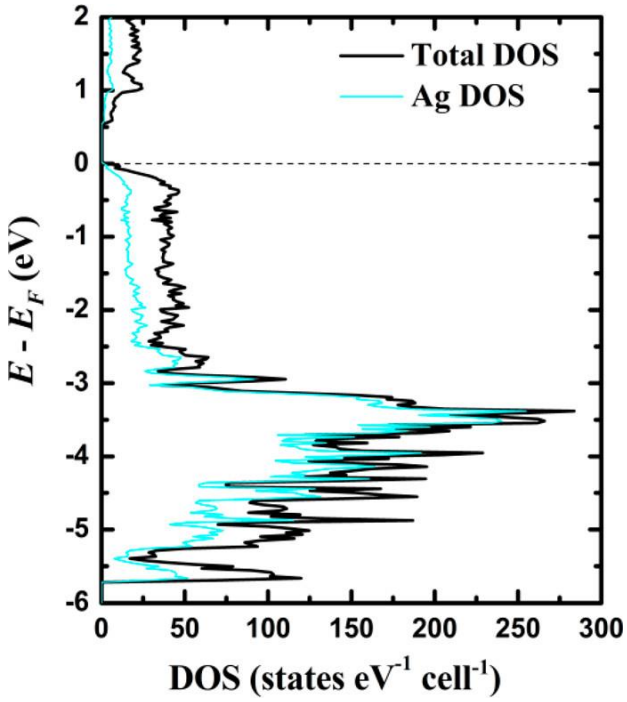

Figure 3-4: Density of states of $Tl_2Ag_{12}Se_7$.

The states both above and below the Fermi level (dashed horizontal line) comprise Ag as well as Se contributions because of the covalent character of the Ag–Se interactions. The region between −3 and −6 eV is dominated by the (filled) Ag d states, while the Tl states have only negligible contributions, in part caused by the small amount of Tl in this material. The Tl-s states occur below the selected energy window.

Upon heating, two phase transitions are observed, namely, at 410 K and at 710 K (Figure 3-5). The first reversible one (*α*–*β*) corresponds to a minor change in the crystal structure, as no obvious changes were identified in a powder diagram obtained at 453 K, and the latter likely corresponds to the melting point. A comparison with a previous phase diagram study of the Tl_2Se–Ag_2Se system implies that $Tl_2Ag_{12}Se_7$ was originally identified as "$TlAg_7Se_4$", which would incongruently melt into a more Tl-rich liquid and solid Ag_2Se at 699 K.[89] Upon fast cooling, one

obtains $Tl_2Ag_{12}Se_7$ and a small amount of "$TlAg_3Se_2$", which explains the occurrence of a second crystallization peak. The shifts in the peak positions of the heating and cooling curves are a consequence of the fast cooling rate, causing a delay in the onset of the phase transitions.

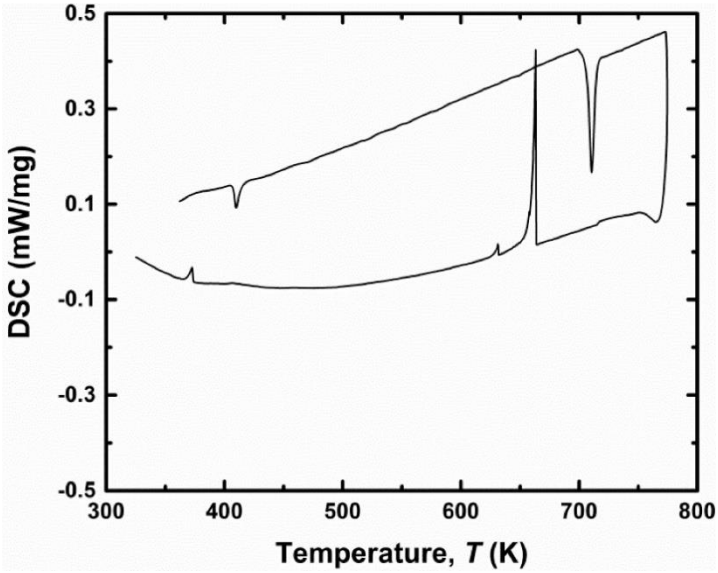

Figure 3-5: DSC of $Tl_2Ag_{12}Se_7$.

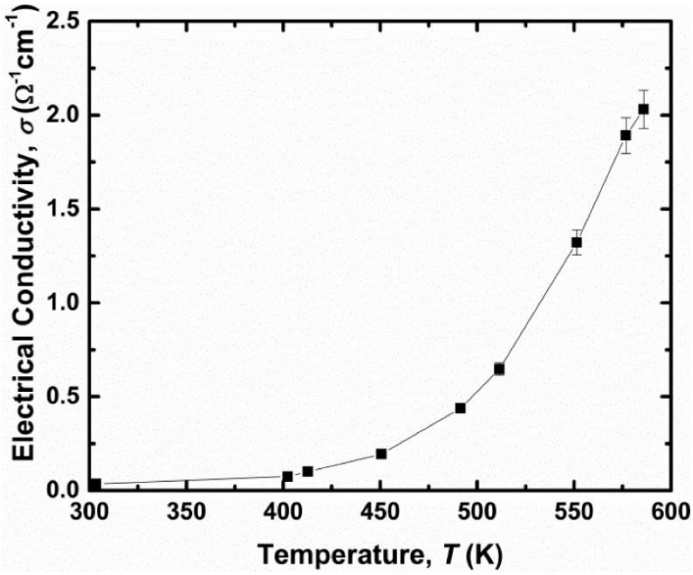

Figure 3-6: Electrical conductivity of $Tl_2Ag_{12}Se_7$.

The electrical conductivity (σ) curve exhibits more or less an exponential increase with increasing temperature, as predicted for an intrinsic, or slightly doped, semiconductor (Figure 3-6). This implies that the charge carrier concentration remains low during the phase transition, while changing its dominant character from holes to electrons to holes. The σ values range from 0.04 Ω^{-1} cm^{-1} at 303 K to 2.0 Ω^{-1} cm^{-1} at 586 K. These values are too small for the thermoelectric energy conversion, where σ values of the order of several hundred Ω^{-1} cm^{-1} are required.

The almost exponential temperature dependence of the electrical conductivity allows for an experimental estimation of the band gap, E_g, from the slope of the lnσ vs 1/T curve (Figure 3-7). We obtained a linear fit with a regression coefficient of $R^2 = 0.999$, and $E_g = 0.8$ eV. As expected, the experimental band gap is larger than the calculated one of 0.5 eV, while of the same order of magnitude.

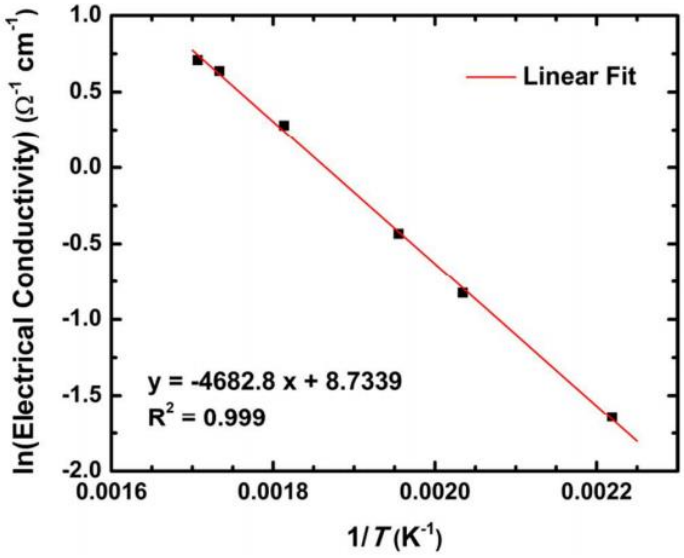

Figure 3-7: Linear fit of the lnσ, 1/T curve.

The thermal conductivity remains below κ = 0.45 W m^{-1} K^{-1} during the whole data collection up to 578 K (Figure 3-8). These values are significantly lower than those of benchmark

thermoelectric bulk materials such as Bi_2Te_3 and PbTe, and comparable to those of Tl-rich chalcogenides such as Tl_9BiTe_6[60] and $Tl_{10-x}Sn_xTe_6$ and $Tl_{10-x}Pb_xTe_6$.[25] In this case, however, the Tl content is so small that the major driving force is the complexity of this structure, combined with partly deficient Ag sites and enlarged anisotropic displacement factors (ADPs, averaged to the U_{eq} values listed in Table 3-2), rather than the presence of Tl atoms. Specifically, the Se4 and Se5 atoms of the linear Se chains and their surrounding Ag sites, Ag2, Ag4, and Ag6, display larger ADPs than the other Se and Ag sites, respectively, while the Tl site is inconspicuous in contrast to $Tl_{10-x}Sn_xTe_6$ and $Tl_{10-x}Pb_xTe_6$. [25]

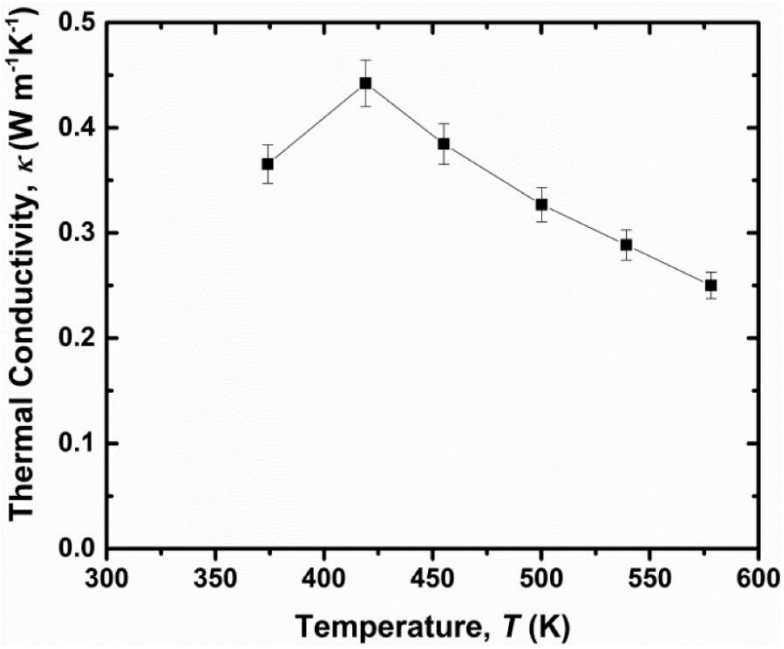

Figure 3-8: Thermal conductivity of $Tl_2Ag_{12}Se_7$.

The thermal conductivity shows a peak during the phase transition, namely, a maximum of 0.44 W m^{-1} K^{-1} at 419 K, up from 0.36 W m^{-1} K^{-1} at 374 K. Thereafter, κ proceeds to gently decrease with increasing temperature because of the increasing lattice vibrations, down to 0.25

W m^{-1} K^{-1} at 578 K. Since the electrical conductivity remains small throughout this temperature range, the electronic contribution to the thermal conductivity is negligible.

We attempted to investigate in more detail the originally observed *pnp* transition at the phase transition. The cause for the *pnp* transition was postulated as the variation of the charge of the chain of Se atoms. The XPS data of the Se atoms, compared at different temperatures, revealed no obvious change before and after the phase transition (Figure 3-9). The other two elements, Tl and Ag did not show any significant variation either.

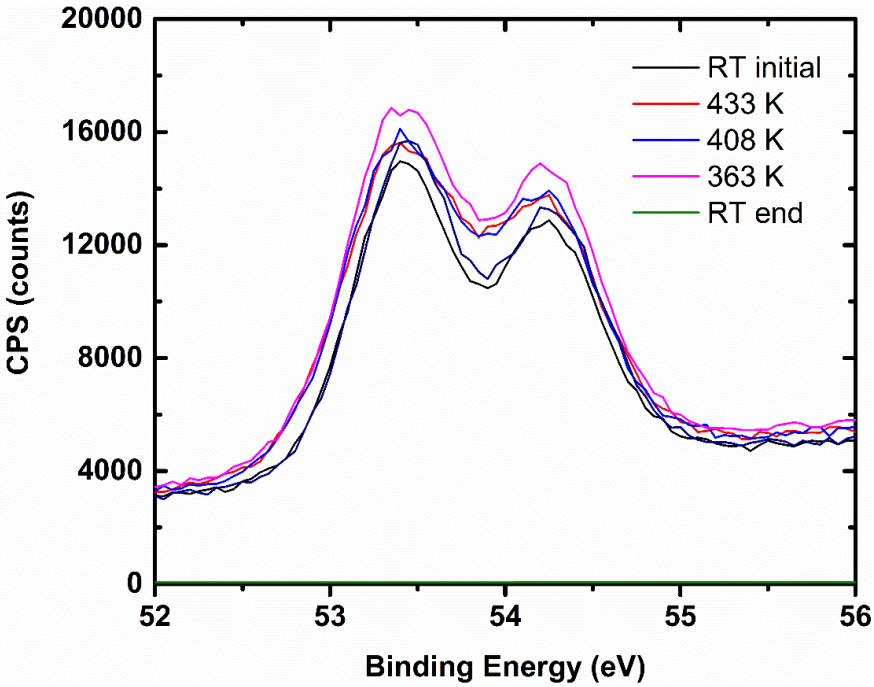

Figure 3-9: Se-3d XPS patterns of $Tl_2Ag_{12}Se_7$ obtained at different temperatures.

We reinvestigated the raw Seebeck coefficient data collected and calculated from the ULVAC® ZEM-3 instrument and found a problem in how the Seebeck coefficient was calculated. The ZEM-3 instrument software applied the least square fit method to calculate the Seebeck coefficient at certain temperatures based on three pre-set temperature differences. However,

this method is only precise when the voltage difference versus temperature difference corresponds to a linear relationship. The raw data of the voltage difference and the temperature difference obtained from the ZEM-3 instrument had an inversely proportional relationship, leading to a negative slope which was mistakenly interpreted as switching from *p*- to *n*- to *p*-type around the phase transition. This was likely caused by reaching the limits of the instrument because of the high Seebeck coefficient (Table 3-4). In fact, each Seebeck measurement resulted in a positive value, proving that the seemingly occurring *pnp* transition was an artifact of the analysis method.

Table 3-4: Raw Seebeck data obtained from ZEM-3 device at 370 K, 410 K, and 460 K.

Temperature (K)	Seebeck Coefficient (μV K^{-1})	Temperature Difference (K)
370	4590	1.63
	2941	2.44
	2189	3.28
410	4453	1.72
	3237	2.57
	2632	3.46
460	4846	1.69
	3262	2.51
	2462	3.36

A new low temperature Seebeck measurement done with a PPMS confirmed that this material is *p*-type below 380 K, with high Seebeck values from 700 μV K^{-1} at 215 K to 550 μV K^{-1} at 380 K (Figure 3-10). The data obtained from the PPMS revealed that all the Seebeck values are

in a normal magnitude, unlike suggested in the Table 3-4 obtained from the ZEM-3 instrument. Further investigations into accurate Seebeck values at high temperatures will be performed.

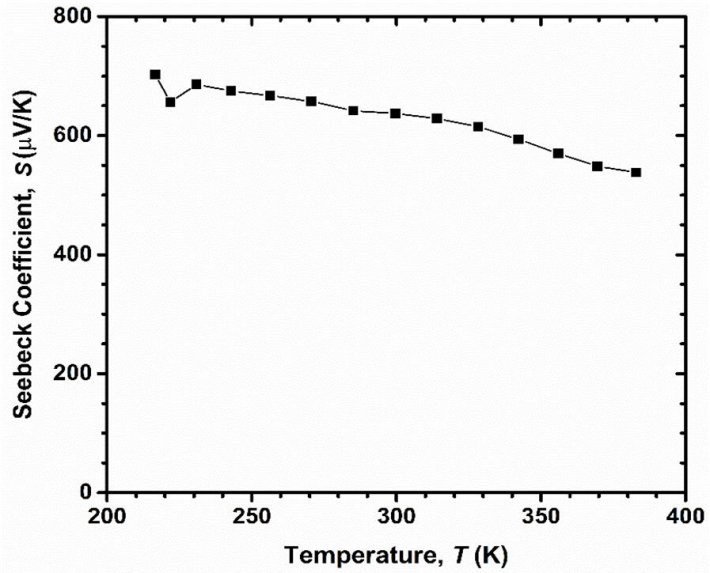

Figure 3-10: Low temperature Seebeck coefficients of $Tl_2Ag_{12}Se_7$.

3.4 Conclusions

A new selenide, $Tl_2Ag_{12}Se_7$, was discovered and characterized. It crystallizes in a supercell of the $Zr_2Fe_{12}P_7$ type. We determined this material to be a semiconductor with a very low thermal conductivity. Despite the low thermal conductivity, the thermoelectric performance is insufficient because of the low electrical conductivity. Increasing the charge carrier concentration would be required to be able to obtain useful thermoelectric properties, in addition to replacing the Tl atoms to reduce the toxicity. In the future, we will also re-analyze the Seebeck values at high temperatures and the phase transition.

Chapter 4: Thermoelectric Properties of $Tl_2Ag_{12}Te_{7+\delta}$

4.1 Introduction

Previously, the crystal structure of $Tl_4Ag_{24-x}Te_{15-y}$ was reported to be of the $Zr_2Fe_{12}P_7$ type but include an impossibly short Te–Te distance, smaller than 2.4 Å. In addition, thallium silver telluride such as TlAgTe and $TlAg_9Te_5$ possess ultralow thermal conductivity, which gives the hope that $Tl_2Ag_{12}Te_7$ could have low thermal conductivity.[69,90] In this chapter, an incommensurate composite crystal structure with all the Te–Te distances larger than 2.8 Å was solved, and the electronic structure was simulated via four models with various Te atom chains along *c* axis. The high disorder of the linear Te atom chain contributes to an extraordinarily low thermal conductivity that further leads to the highest *zT* value achieved by a misfit structure material. This project ultimately supports the concept of using composite structures as TEs.

4.2 Experimental Procedures

The elements were used directly as required (Tl, granules, 6 mm, 99.99%, Alfa Aesar; Ag, shots, 99.99%, Strem Chemicals; Te, broken ingots, 99.99%, Strem Chemicals). To determine whether or not a phase width of the originally reported $Tl_4Ag_{24-x}Te_{15-y}$ (x = 2, y = 0) exists,[1] we began with three different Tl:Ag:Te molar ratios of 4:22:14.5, 4:22:15, and 4:22:15.5. The samples were heated to 1173 K within 20 hours and then kept at 1173 K for ten more hours. For the single crystal growth, the furnace was slowly cooled down over 100 h. This yielded ingots that appeared to be homogeneous. Later for the property measurements, new, larger samples were simply water-quenched directly from 1173 K to save reaction time.

Ground samples of nominal compositions of "$Tl_4Ag_{22}Te_{14.5}$", "$Tl_4Ag_{22}Te_{14.5}$", and "$Tl_4Ag_{22}Te_{14.5}$" were hot-pressed at 623 K and 70 MPa for 6 h, resulting in densities of 99% of the theoretical density, as determined via the Archimedes method.

The diffraction patterns were collected at room temperature for 60 min in the 2ϑ range from 5° to 120°. No systematic differences were detected between them and the one calculated from the published model for $Tl_4Ag_{24-x}Te_{15-y}$[1] or the one calculated from our structure solution (Figure 4-1).

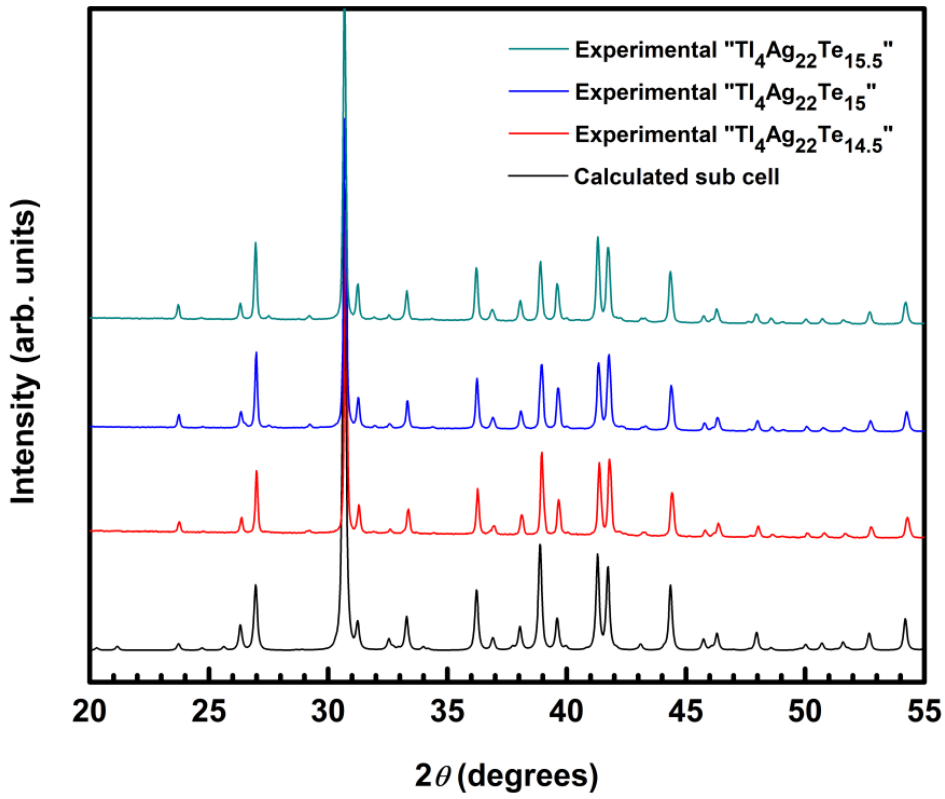

Figure 4-1: PXRD Patterns of "$Tl_4Ag_{22}Te_{14.5}$", "$Tl_4Ag_{22}Te_{15}$", and "$Tl_4Ag_{22}Te_{15.5}$" compared to the calculated sub cell.

Scanning electron microscopy studies were performed on three samples with the nominal compositions "$Tl_4Ag_{22}Te_{14.5}$", "$Tl_4Ag_{22}Te_{15}$", and "$Tl_4Ag_{22}Te_{15.5}$". EDX mappings showed that all

three elements were distributed evenly through the whole area. No significant differences were found between the samples (Table 4-1).

Table 4-1: EDX results on the "$Tl_4Ag_{24-x}Te_{15-y}$" samples. Values calculated from the starting compositions are given in parentheses.

Composition	Tl	Ag	Te
"$Tl_4Ag_{22}Te_{14.5}$"	9.3% (9.9%)	56.0% (54.3%)	34.7% (35.8%)
"$Tl_4Ag_{22}Te_{15}$"	9.7% (9.8%)	55.8% (53.7%)	34.5% (36.6%)
"$Tl_4Ag_{22}Te_{15.5}$"	9.3% (9.6%)	56.1% (53.0%)	34.6% (37.4%)

The DSC and TG measurements were implemented on a ground sample of approximately 30 mg of "$Tl_4Ag_{22}Te_{14.5}$". The experiment was carried out under a constant argon flow with a heating rate of 20 K min^{-1} up to 823 K

For single crystal structure studies, the data were collected by scanning ω and φ in steps of 0.3° in different sets of frames for full data coverage and low redundancy, using the search strategy part of the APEX II suite. The exposure time was 45 s per frame. In analogy with the related selenides $K_2Ag_{12}Se_7$ (space group $P6_3/m$)[83] and $K_2Ag_{12}Se_{7.11}$ (space group $P6_3$),[86] the systematic absences pointed to the existence of a 6_3 screw axis. The structure solution was found via direct methods in the space group $P6_3$ and then refined using the least-squares procedure of the SHELXTL package.[78] The tidy routine of the Platon program package[87] was utilized to standardize the atomic positions. Its addsymm part was applied to identify potential additional symmetry elements; none were found. The small Flack parameter of 0.15(4) is also indicative of a noncentrosymmetric space group.

Three of the five positions of this structure model, namely the two Ag sites and Te2, exhibit enlarged anisotropic displacement parameters, quite uniformly in the case of the Ag sites but very anisotropically in the case of Te2, with $U_{33} > 10 \times U_{11}$ (and $U_{11} = U_{22}$). Refining the occupancies of all these three sites resulted in significant deficiencies, namely 97% occupancy for Ag1, 95% for Ag2, and 71% for Te2. This yielded a refined formula of $Tl_2Ag_{11.54(7)}Te_{7.42(2)}$, and a final agreement factor of $R(F_o) = 0.039$ (observed data). Crystallographic data of this model are summarized in Table 4-2, atomic positions are listed in Table 4-3, and selected bond distances in Table 4-4. Analysis of a second crystal from a reaction repeated under the same conditions confirmed the above results, with occupancies of 95%, 96%, and 67% for Ag1, Ag2, and Te2, respectively, with $R(Fo) = 0.045$ (observed data).

Table 4-2: Crystallographic Details of the Subcell Refinement of $Tl_2Ag_{11.5}Te_{7.4}$

Formula	$Tl_2Ag_{11.54(7)}Te_{7.42(2)}$
Crystal System	Hexagonal
Space group	$P6_3$ (no. 173)
***a*, *c* [Å]**	11.4249(4), 4.6210(2)
***V* [Å^3]**	522.36(3)
Z	1
Density [g cm^{-3}]	8.26
Absorption coefficient [mm^{-1}]	36.03
***F*(000)**	1090
Crystal Size [mm]	$0.04 \times 0.04 \times 0.01$
Temperature (K)	296(2)
Radiation [Å]	0.71073
Total, Unique Data, *R*(int)	2268, 568, 0.046

Observed Data [I > 2σ(I)]	548
$R(F_o)$,[a] $R_w(F_o^2)$,[b] GOF (obs. Data)	0.039, 0.083, 1.08
Min., max. residual electron density [e Å^{-3}]	-2.56, 3.26

[a]$R(F_o) = \sum||F_o| - |F_c||/\sum|F_o|$.
[b]$R_w(F_o^2) = [\sum[w(F_o^2 - F_c^2)^2]/\sum[w(F_o^2)^2]]^{1/2}$, with F_o and F_c being the observed and calculated structure factors, respectively.

Table 4-3: Fractional atomic coordinates, equivalent isotropic displacement parameters, and occupancies of the subcell refinement of $Tl_2Ag_{11.5}Te_{7.4}$

	x	***y***	***z***	**U_{eq}/Å^2**	**occ.**
Tl1	1/3	2/3	0.1872(7)	0.0385(3)	1
Ag1	0.1511(2)	0.2800(2)	0.197(1)	0.0531(7)	0.973(8)
Ag2	0.4158(2)	0.0677(1)	0.182(1)	0.0458(6)	0.950(8)
Te1	0.4219(1)	0.3148(1)	0.1853(5)	0.0254(3)	1
Te2	0	0	0.15(1)	0.153(6)	0.71(1)

Table 4-4: Interatomic distances (Å) of the subcell of $Tl_2Ag_{11.5}Te_{7.4}$

Tl1–Te2	3×	3.545(3)	**Ag2–Te1**	2.878(5)
Tl1–Te1	3×	3.557(3)	**Ag2–Te1**	2.879(2)
Ag1–Te2		2.782(4)	**Ag2–Te1**	2.903(5)
Ag1–Te1		2.917(2)	**Ag1–Ag2**	2.967(2)
Ag1–Te1		2.964(4)	**Ag1–Ag2**	3.001(6)
Ag1–Te1		3.047(4)	**Ag1–Ag2**	3.107(6)
Ag2–Te1		2.789(2)		

The large anisotropy of Te2, along with the (physically impossible) short distances to itself of $c/2$ = 2.31 Å by symmetry, caused us to closely inspect the reciprocal space images, suspecting a supercell along the *c* axis that would resolve both issues. Indeed, additional so far not indexed

satellite reflections were observed, with spacing indicative of an incommensurate supercell along the *c* axis.

The modulated structure was solved using charge flipping in hyperspace as implemented in the program Superflip,[91] using the same crystal data. The initial model of the modulated structure reveals that the Tl and the Ag positions are only slightly affected by the modulation, as might be expected from their uniform displacement parameters from the subcell refinement. The same is true for one of the Te positions, Te1, while Te2 shows a very strong positional modulation in line with its highly anisotropic displacement parameters in the subcell refinement. The shape of this modulation indicates that the structure is in fact a composite, and Te2 was therefore modeled using an alternative *c* axis given by c^* (Te2) = $c^* \times (1 - q)$, with $q = -0.4403$, thus yielding a *c* axis of 3.212 Å. Even in this composite model, the Te2 position must be described by quite a large modulation, and in the final model the atomic surface of Te2 was modeled using a sawtooth wave. This model was refined using the software package JANA2006,[79] resulting in the formation of Te dimers and trimers along the *c* axis. According to this refinement, Te2 is fully occupied, but its repeat unit is smaller than the base cell because of the smaller c axis. With the *c* axis ratio being 4.626/3.212 = 1.44, it corresponds to a 144%/2 = 72% occupancy of Te2 with respect to the base cell (2 Te2 sites per base cell), comparable to the abovediscussed refined subcell refinement yielding an occupancy of 71(1)% for Te2 (Table 4-2).

The atomic modulation functions can be found in the Appendix (Figures A1-A6). Refining the structure as a composite had a small impact on the lattice parameters of the base cell as well, resulting in *a* = 11.438(1) Å and *c* = 4.6256(5) Å, space group $P6_3(00\gamma)s$, and space group $P6(00\gamma)s$ for the Te2 component. Final agreement parameters were $R1(\text{obs}) = 6.7\%$ for the main reflections,

*R*1(obs) = 12.7% for the first order satellites, and *R*1(obs) = 36.7% for the second order satellites. It should be noted that the second order satellites are very weak, and thus a poor fit between model and data is to be expected. Atomic positions are summarized in Table 4-5.

Table 4-5: Fractional atomic coordinates, equivalent isotropic displacement parameters, and occupancies of $Tl_2Ag_{11.5}Te_{7.4}$ from the composite refinement

	x	***y***	***z***	U_{eq}/Å^2	**occ.**
Tl1	1/3	2/3	0.1722(2)	0.0383(2)	1
Ag1	0.15114(8)	0.27998(9)	0.1606(5)	0.0517(4)	0.96
Ag2	0.41570(8)	0.06732(7)	0.1709(4)	0.0454(3)	0.95
Te1	0.42194(4)	0.31456(5)	0.17142(2)	0.0252(2)	1
Te2	0	0	0.19(1)	0.0762(7)	1

For the electronic structure calculations, four different models, all with fully occupied Ag sites, were chosen for the composite structure; all of them based on the subcell refinement summarized in Tables 3−4. For model I, that subcell was used directly, with only one Te atom in the chain, corresponding to the formula $Tl_2Ag_{12}Te_7$ in space group *P*3 (no. 143). The shortest Te−Te contact within the chain then equals the original *c* axis of 4.62 Å. For model II, we tripled the *c* axis and filled it with four Te atoms in the chain, resulting in a formula of $Tl_3Ag_{18}Te_{11}$ = $Tl_2Ag_{12}Te_{7.33}$ with Te trimers alternating with isolated Te atoms along *c*, i.e. Te−Te contacts along *c* of 3.00 Å−3.00 Å−3.93 Å−3.93 Å. For models III and IV, we doubled the *c* axis and filled it with three Te atoms in the chain per unit repeat, corresponding to the formula $Tl_4Ag_{24}Te_{15}$ = $Tl_2Ag_{12}Te_{7.5}$, allowing for a Te_2^{2-} pair (*d* = 2.78 Å) alternating with an isolated Te atom in the case of model III. In model IV, we imposed a formation of a linear Te atom chain with equidistant Te−Te distances of 2*c*/3 = 3.08 Å. These four model calculations were performed with 137, 43,

146, and 146 independent *k* points of the first Brillouin zone along the respective vectors of the reciprocal lattice, respectively.

4.3 Results and Discussion

The subcell of $Tl_2Ag_{12}Te_{7+\delta}$ is depicted in Figure 4-2a. It consists of a three-dimensional framework structure of covalently bound $AgTe_4$ tetrahedra, whose channels are filled by Tl atoms, which in turn are surrounded by six Te atoms in form of a trigonal prism at distances of 3.55 Å and 3.56 Å. The Ag−Te distances within the tetrahedra are with 2.78 Å − 3.05 Å inconspicuous, and the edge condensation of the AgTe4 tetrahedra allows for multiple Ag−Ag contacts between 2.97 and 3.11 Å. Those Ag−Ag interactions commonly occur in silver tellurides, as discussed for $BaAg_2Te_2$[92] or, most recently, $Tl_2NdAg_3Te_4$.[88] This structure is topologically equivalent with the $Zr_2Fe_{12}P_7$ type,[85] with the exception of the peculiar Te chain running along the *c* axis through the origin (Figure 4-2b). In contrast to $Zr_2Fe_{12}P_7$, there is more than one atom in this chain on (0, 0, *z*) of the title compound per repeat unit, which we refined to 1.42(2), corresponding to δ = 0.42(2) in the formula of $Tl_2Ag_{12}Te_{7+\delta}$. Kolis et al. made a similar observation in the case of $K_2Ag_{12}Se_{7.11}$.[86] Disordered chalcogen atom chains were also observed in $K_2Ag_{12}Se_7$[83] and $K_2Ag_{12}Te_7$,[84] respectively, albeit without Se or Te excess. It remains to be seen whether or not these cases should be treated as composite structures.

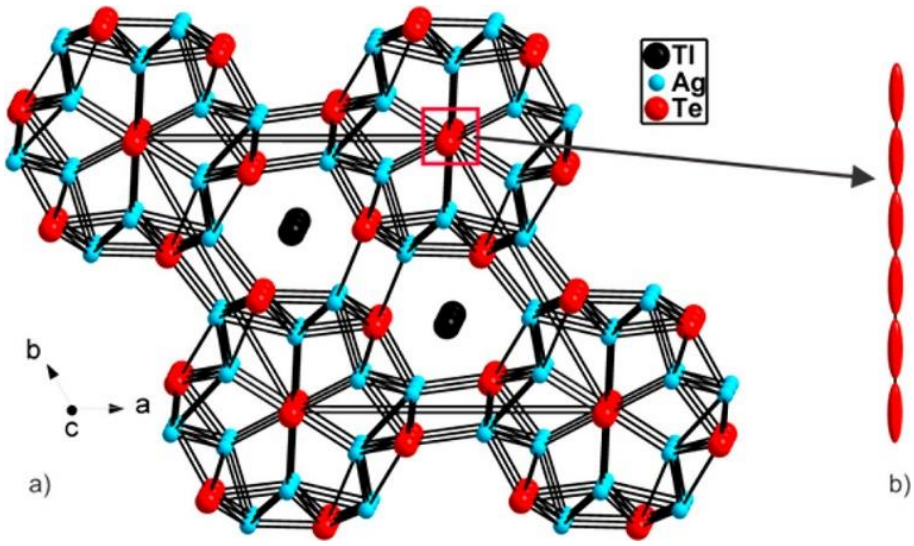

Figure 4-2: (a) Subcell of $Tl_2Ag_{12}Te_7$; (b) ellipsoid representation of the linear Te2 chain on (0, 0, z)

Our refinement as a composite structure showed that the linear Te2 chain in $Tl_2Ag_{12}Te_{7+\delta}$ is best described as consisting of Te_2 and Te_3 fragments with two different interatomic distances, namely 2.93 Å within these fragments and 3.66 Å between them (Figure 4-3). With that, the average repeat unit of a Te atom of the dimer is 1/2 (2.93 Å + 3.66 Å) = 3.295 Å and of a Te atom of the trimer is 1/3 (2 × 2.93 Å + 3.66 Å) = 3.173 Å. With *c*(Te2) = 3.212 Å, this results in a 1:2 ratio of dimers to trimers, because 1/3 × 3.295 Å + 2/3 × 3.173 Å = 3.214 Å.

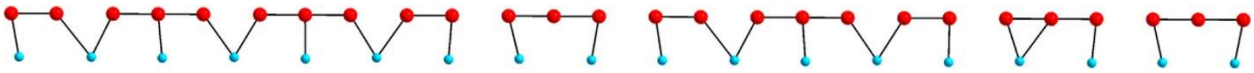

Figure 4-3: Section of the composite structure along the modulation (c) axis comprising Te dimers and trimers (shown with the neighboring Ag1 atoms.)

The example of the related semiconducting selenide, $Tl_2Ag_{12}Se_7$, showed the cations all to be in the expected +1 state, and the Se atoms to be 2−, according to $(Tl^+)_2(Ag^+)_{12}(Se^{2-})_7$. In the case of the telluride, the observed Te_2 and linear Te_3 fragments within the linear Te atom chain typically exists as Te_2^{2-} and Te_3^{4-}, isovalent with I_2 and I_3^-, respectively. A Te_4^{6-} unit occurs in $Ag_{10}Te_4Br_3$,[93] and a Te_2^{2-} unit loosely connected to an isolated Te^{2-} in $Ag_{23}Te_{12}Cl$ and $Ag_{23}Te_{12}Br$.[94]

Previously we have found such Te_2^{2-} dumbbells in $BaCu_{6-x}STe_6$ and $BaCu_{6-x}SeTe_6$,[95,96] and the Se analogue to Te_3^{4-} in $Ba_2Ag_4Se_5$,[97] the latter being a hypervalent 22 valence-electron unit with 4-electron-3-center bonds like I_3^-. The Sb atom equivalent of that, Sb_3^{7-}, is known from the $Ca_{14}AlSb_{11}$ type,[98] adopted by one of the leading high temperature thermoelectric materials, $Yb_{14}MnSb_{11}$.[99–101] Related linear Sb atom chains occur in another high performance thermoelectric, namely in *β*-Zn_4Sb_3.[102–104] These Sb atom chains consist of alternating Sb−Sb distances of 2.82 and 3.38 Å.

With 1.4 Te atoms per formula unit being in this chain, a good approximation would be a charge-balanced formula of $(Tl^+)_2(Ag^+)_{11.75}(Te^{2-})_6(Te_2^{2-})_{0.175}(Te_3^{4-})_{0.35}$; that is, the Te chain would be balanced by an Ag deficiency of 0.25 per formula unit, compared to a refined deficiency of 0.47(7).

To analyze the impact of different Te atoms chains, we calculated the electronic structures of four different models of the formulas $Tl_2Ag_{12}Te_7$ (1 Te atom per unit cell chain repeat of c = 4.62 Å), $Tl_2Ag_{12}Te_{7.33}$ (1.33 Te atoms per repeat, forming alternating Te_3 units and isolated Te atoms), and $Tl_2Ag_{12}Te_{7.5}$ (1.5 Te atoms per repeat, alternating Te pairs and isolated Te atoms in model III as well as equidistant Te atom chain with interatomic distances of 3.08 Å in model IV). The respective Te atom chains are depicted at the top of Figure 4-4, along with the calculated band structures of the three-dimensional models. Therein, the contributions of the p_z orbitals of the chain Te atoms, i.e. the *p* orbitals aligned along the chain direction, are emphasized via the fat band representation.

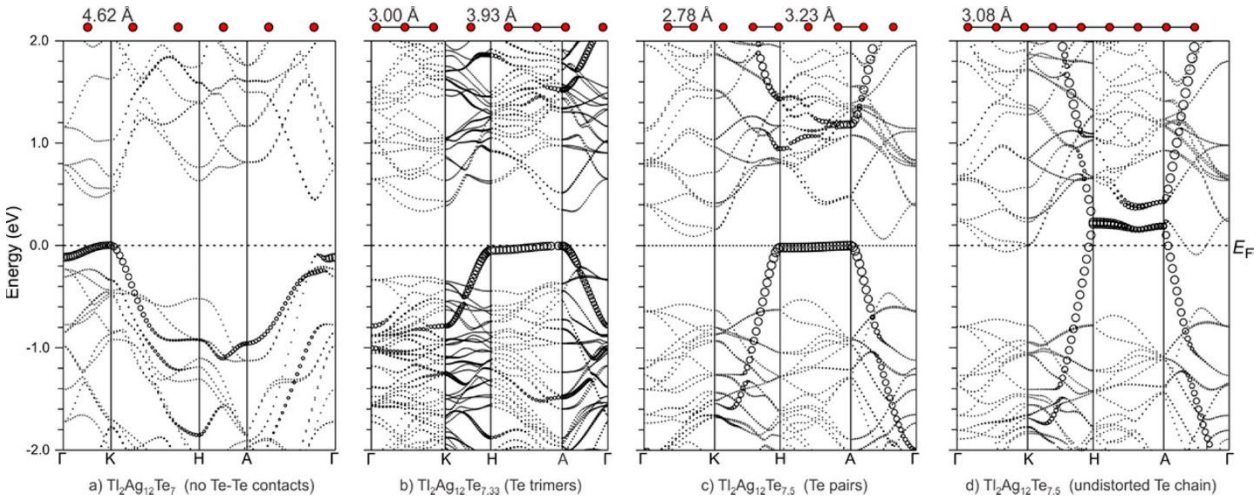

Figure 4-4: Band structures of (a) $Tl_2Ag_{12}Te_7$ without Te–Te contacts; (b) $Tl_2Ag_{12}Te_{7.33}$ with Te trimers; (c) $Tl_2Ag_{12}Te_{7.5}$ with Te pairs; (d) $Tl_2Ag_{12}Te_{7.5}$ with an undistorted Te chain. Γ: (0, 0, 0); K: (1/3, 1/3, 0); H: (1/3, 1/3, 1/2); A: (0, 0, 1/2) in fractional coordinates of the reciprocal lattice.

In case of the $Tl_2Ag_{12}Te_7$ model (model I, Figure 4-4a), the band structure is quite similar to the one of $Tl_2Ag_{12}Se_7$; as no significant Te−Te interactions exist, the *p* states of Te are all in the valence band (along with the Ag *d* states), with p_z having the largest dispersion along *c**, i.e. from K to H and from A → Γ. This model is semiconducting with a calculated band of 0.4 eV.

The $Tl_2Ag_{12}Te_{7.33}$ model (II) with an ordered Te atom chain is also semiconducting; with its Te_3^{4-} unit, antibonding Te−Te p_z states occur above the Fermi level in the conduction band (Figure 4-3b). In the formula $Tl_6Ag_{36}Te_{22}$, three Te atoms are part of the Te_3^{4-} anion, with the rest being isolated Te^{2-}, which results in the balanced formula $(Tl^+)_6(Ag^+)_{36}(Te^{2-})_{19}(Te_3^{4-})$. Such Te−Te, or Se−Se and Sb−Sb, interactions have been shown to decrease the band gap;[105,106] here the Te p_z states associated with the bonding in the Te_3^{4-} unit occur at the top of the valence band, thereby decreasing the calculated band gap to 0.32 eV. Moreover, these Te p_z states form a flat band at the top of the valence band from H → A (i.e., perpendicular to the chain direction), advantageous for a high Seebeck coefficient, and a steep band along the chain direction, i.e. from K → H and A

→ Γ, advantageous for high electrical conductivity along that direction. Correspondingly, the partial DOS from the Te p_z states exhibits a sharp peak at the top of the valence band (Figure A11).

The $Tl_2Ag_{12}Te_{7.5}$ model (III) with a differently ordered Te atom chain, namely alternating isolated Te atoms and Te_2^{2-} units, exhibits several comparable features (compare Figure 4-4c with 3-4b). The semiconducting properties can be understood on the basis of the charge-balanced formula $(Tl^+)_4(Ag^+)_{24}(Te^{2-})_{13}(Te_2^{2-})$. Noteworthy is the same flat band at the top of the valence band from H → A, and the steep band from K → H and A → Γ. This indicates that the exact Te concentration is not vital for either the semiconducting properties or the coexistence of a flat and a steep band below the Fermi level, as long as a distorted Te atom chain is present.

On the other hand, an undistorted Te atom chain as chosen in the model $Tl_2Ag_{12}Te_{7.5}$ with equidistant Te−Te distances of 3.08 Å (model IV) would lead to the presence of Te p_z states connecting the valence and the conduction band (Figure 4-4d), thereby destroying the band gap, as documented for such isolated undistorted chains as well.[107,108] Therefore, such a scenario would always result in metallic properties, at least along the *c* axis. It should be noted that the metallic properties are not directly related to the Te atom concentration but to the lack of an ordering within the chain. This is evident from a comparison of the two models (c and d) with the same Te amount but different Te chains as above-described.

The DSC scan for "$Tl_4Ag_{22}Te_{14.5}$" is displayed in Figure 4-5, showing that this phase decomposes at 670 K. The next peak, occurring at 715 K, could be the melting point of the impure tellurium, and the ones around 750 K the melting points of TlAgTe and $TlAg_9Te_5$.[109] This results in the following reactions at these temperatures (with L = liquid):

At 670 K: “$Tl_4Ag_{22}Te_{14.5}$“ ⇌ TlAgTe + $TlAg_9Te_5$ + “Te“ (1)

At 715 K: “Te“ ⇌ L (2)

At 750 K: $TlAg_9Te_5$ ⇌ Ag_2Te + L and TlAgTe ⇌ L’ (3)

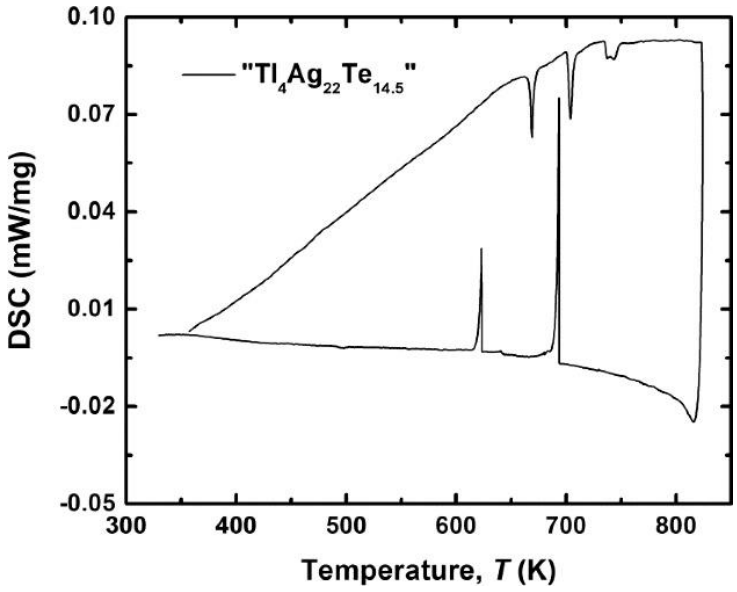

Figure 4-5: Differential scanning calorimetry of “$Tl_4Ag_{22}Te_{14.5}$”.

The electrical conductivity data confirm the abovementioned hypothesis that this material with an ordered Te atom chain is indeed intrinsically semiconducting, regardless of the exact Te content of the samples (Figure 4-6). A sharp, in part exponential increase is evident for each case, with the high temperature electrical conductivity being σ = 57 Ω^{-1} cm^{-1} around 525 K. Plotting ln σ vs 1/T of the three data sets resulted in linear curves in each case (Figure 4-5). The so derived experimental band gaps were 0.5 eV − 0.6 eV. For comparison, the same procedure yielded an experimental gap of 0.8 eV in the case of $Tl_2Ag_{12}Se_7$.

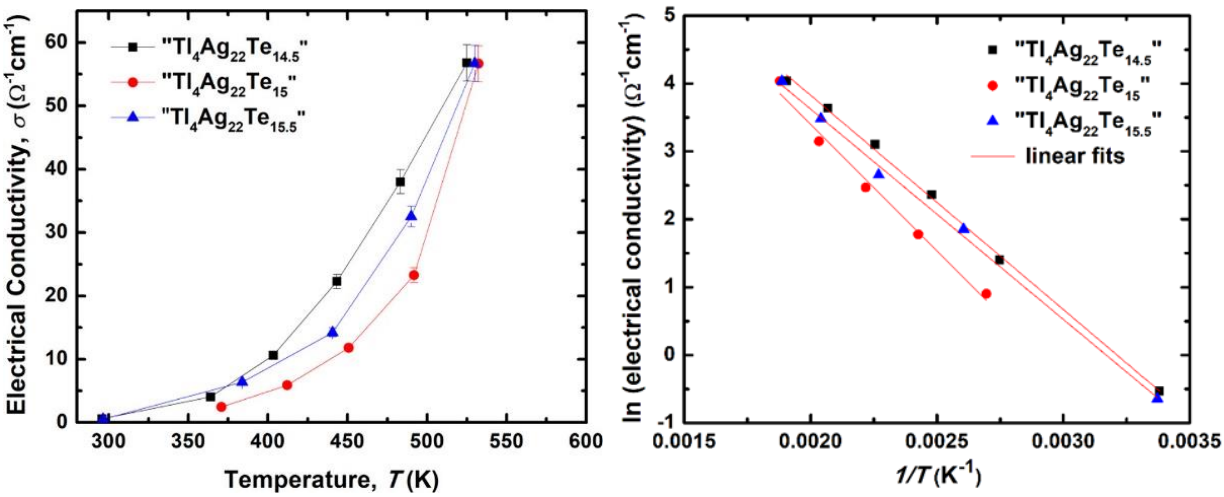

Figure 4-6: Electrical conductivity and linear fits of ln(electrical conductivity) versus 1/T.

With respect to the thermoelectric performance, σ = 57 Ω^{-1} cm^{-1} constitutes a positive change from the low electrical conductivity of the selenide $Tl_2Ag_{12}Se_7$ with σ = 2 Ω^{-1} cm^{-1} at 586 K. This is in part caused by the decrease in band gap, resulting in a higher carrier concentration at elevated temperatures, and in part by the existence of the steep bands coming from the ordered Te chain, which in turn enhance mobility.

The Seebeck coefficient (Figure 4-7) is also typical for intrinsic semiconductors, slowly decreasing from +550 µV K^{-1} and +630 µV K^{-1} at 300 K to approximately +300 µV K^{-1} at 525 K. Again, the three samples investigated here are remarkably similar despite their nominal differences in Te content, with the high temperature data being equivalent within error. These values are higher than those of the corresponding selenide, despite a higher electrical conductivity, a consequence of the additional flat band caused by the Te–Te interactions.

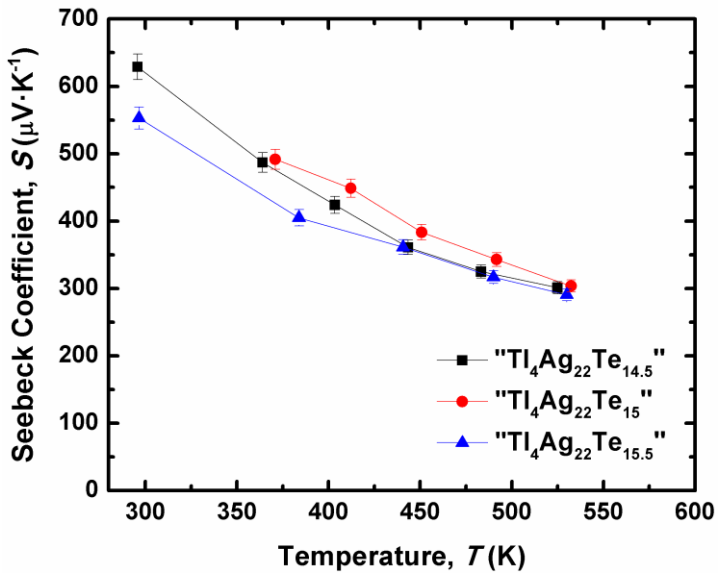

Figure 4-7: Seebeck coefficient of "$Tl_4Ag_{22}Te_{14.5}$", "$Tl_4Ag_{22}Te_{15}$" and "$Tl_4Ag_{22}Te_{15.5}$".

With regard to the thermoelectric performance point of view, the ultralow thermal conductivity of this material constitutes its best feature. As depicted in Figure 4-8, the total thermal conductivity values range from κ = 0.22 W m^{-1} K^{-1} to 0.28 W m^{-1} K^{-1} at all temperatures for all three samples, with the values being below 0.25 W m^{-1} K^{-1} below 400 K. Here, we used the Lorenz number for intrinsic semiconductors, L_0 = 1.5 × 10^{-8} V^2 K^{-2}. Even at the highest temperature and electrical conductivity, κ_e is below 0.05 W m^{-1} K^{-1}, and thus the minor contribution, compared to the lattice conductivity, which varies between 0.20 W m^{-1} K^{-1} and 0.25 W m^{-1} K^{-1}. Higher yet still very low values were found in $Ag_{10}Te_4Br_3$ (0.27 W m^{-1} K^{-1} and 0.43 W m^{-1} K^{-1}), the structure of which also exhibits a complex Ag atom network and hypervalent Te_4^{6-} units but is no misfit structure.[93]

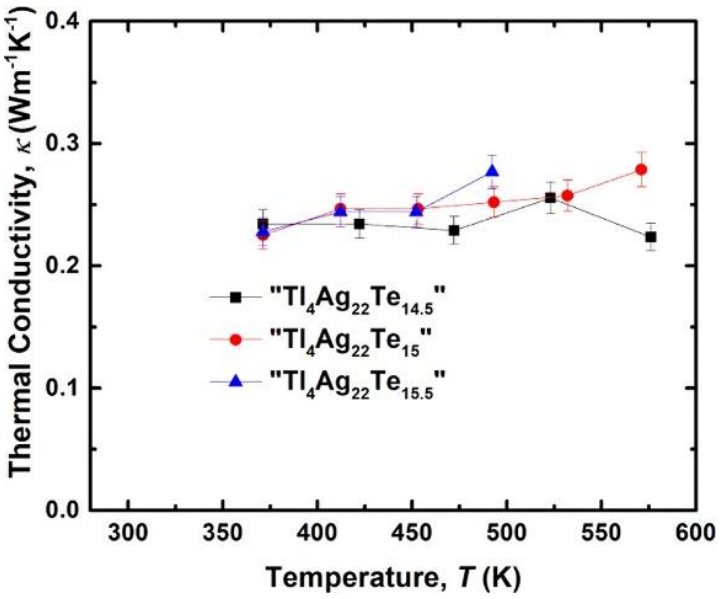

Figure 4-8: Thermal Conductivity of "$Tl_4Ag_{22}Te_{14.5}$", "$Tl_4Ag_{22}Te_{15}$" and "$Tl_4Ag_{22}Te_{15.5}$".

These values are not only significantly smaller than those of the benchmark thermoelectric material Bi_2Te_3 with κ_L = 1.5 W m^{-1} K^{-1},[110] and PbTe with κ_L = 2.2 W m^{-1} K^{-1} at room temperature,[111] but also lower than those of the corresponding selenide, $Tl_2Ag_{12}Se_7$, with κ values between 0.25 W m^{-1} K^{-1} and 0.44 W m^{-1} K^{-1} (comparable to the above-mentioned $Ag_{10}Te_4Br_3$). Thus, replacing Se with Te leads to the rare, most advantageous constellation that both the Seebeck coefficient and the electrical conductivity increase, while the thermal conductivity decreases. Moreover, the thermal conductivity of this composite is also significantly lower than that of the abovementioned misfits $(MS)_{1+x}(TiS_2)_2$ (with M = Sn, Pb, Bi),[112] (κ > 0.65 W m^{-1} K^{-1}), which attained zT_{max} = 0.37 at 700 K, and on par with the likely poorly conducting single crystals of $Bi_2[AE]_2Co_2O_y$ single crystals (AE = Ca, $Ca_{0.5}Sr_{0.5}$, Sr), with κ between 0.2 W m^{-1} K^{-1} and 0.28 W m^{-1} K^{-1} at room temperature.[113]

This extraordinarily low thermal conductivity is likely a consequence of several factors, namely the heavy constituent elements, the local distortions stemming from the

incommensurate composite nature of this structure, and the "dumbbell rattling" of the Te_2^{2-} pairs and Te_3^{4-} trimers. The effect of vibrating dumbbells is a striking illustration of the so-called "schwingendes Elementargebilde", as also found in β-Zn_4Sb_3 with κ_L = 1.3 W m^{-1} K^{-1} at room temperature.[114,115]

Figure 4-9 shows the result of combining the above-mentioned physical properties into *zT*. As a consequence of the exponentially increasing electrical conductivity with temperature, which outweighs the steadily decreasing Seebeck coefficient and the basically temperature-independent thermal conductivity, *zT* has a very strong temperature dependence, surpassing *zT* = 1 around 520 K. Such a high performance of a bulk material at these intermediate temperature is still rare, comparable with *n*-type Bi_2Te_3 (zT_{max} = 1.2 at 423 K)[116] and *p*-type $Tl_9Bi_{0.98}Te_6$ (zT_{max} = 1.1 at 500 K).[117] On the other hand, higher *zT* values were found at higher temperatures in different antimonides and tellurides, including in $Na_{0.95}Pb_{20}SbTe_{22}$ (zT_{max} = 1.7 at 650 K),[118] *β*-Zn_4Sb_3 (1.3 at 670 K),[102] $Tl_{8.10}Pb_{1.90}Te_6$ (1.5 at 680 K),[25] $Tl_{0.02}Pb_{0.98}Te$ (1.5 at 773 K),[119] $Ba_{0.08}La_{0.05}Yb_{0.04}Co_4Sb_{12}$ (1.7 at 850 K),[120] $Na_{0.02}Pb_{0.98}Se_{0.15}Te_{0.85}$ (1.8 at 850 K),[121] and $Yb_{14}Mn_{0.4}Al_{0.6}Sb_{11}$ (1.3 at 1275 K).[122]

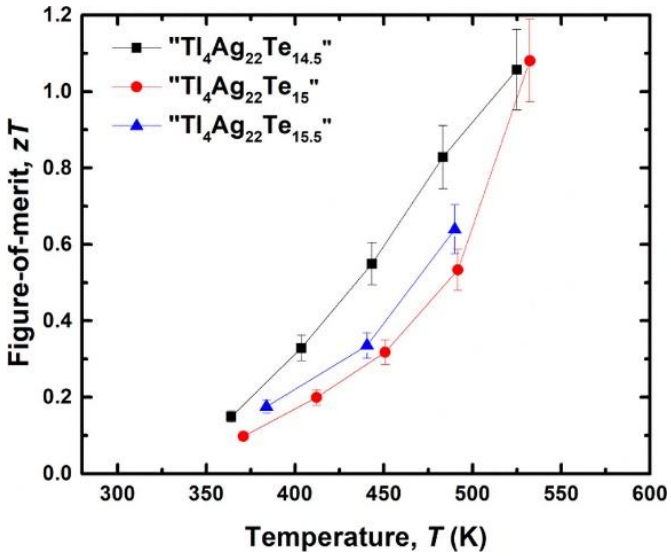

Figure 4-9: Thermoelectric figure-of-merit of "$Tl_4Ag_{22}Te_{14.5}$", "$Tl_4Ag_{22}Te_{15}$" and "$Tl_4Ag_{22}Te_{15.5}$".

The striking difference – in addition to the title compound being the only composite material of that list–is that $Tl_2Ag_{12}Te_{7+\delta}$ achieved its high *zT* value as an undoped semiconductor, i.e. its electrical performance is far from optimized.

4.4 Conclusions

$Tl_2Ag_{12}Te_{7+\delta}$ crystallizes in a variant of the $Zr_2Fe_{12}P_7$ type, consisting of a composite structure of two parts. The first structure is a three-dimensional framework of the stoichiometry $Tl_2Ag_{12}Te_6$, which includes the second structure, a linear Te atom chain, in its tunnels running along the *c* axis. This Te chain is comprised of Te_2^{2-} pairs and Te_3^{4-} trimers, the modulated sequence of which causes significant distortions of the surrounding three-dimensional $Tl_2Ag_{12}Te_6$ framework. Overall this material is bestowed with an ultralow thermal conductivity, caused by its heavy elements, the incommensurate modulation, and possibly "dumbbell rattling". Compared to the corresponding selenide, which adopts a different variant of the $Zr_2Fe_{12}P_7$ type, this material not only exhibits a lower thermal conductivity but also both a higher Seebeck

coefficient and a higher electrical conductivity, a consequence of special features in its band structure arising from the unique Te atom chain. Despite this material being an intrinsic semiconductor, its thermoelectric figure-of-merit surpasses unity. Future work will reveal how optimizing the electrical performance will further enhance the figure-of-merit. In parallel, we are investigating in how far Tl-free analogues, such as $K_2Ag_{12}Se_{7+\delta}$ and $K_2Ag_{12}Te_{7+\delta}$ exhibit comparable properties, noting that their previously reported structures are also based on disordered chalcogen atom chains.

Chapter 5: Thermoelectric Properties of In- and Yb-doped $TlSbTe_2$

5.1 Introduction

$TlSbTe_2$ was first reported in 1961, crystallizing in the $R\bar{3}m$ space group (α-$NaFeO_2$ type).[123] The electronic structure was calculated in 2008, demonstrating that it is a narrow gap semiconductor (when including spin-orbit coupling), as desired for thermoelectric materials.[124] The thermoelectric properties were published by Kurosaki *et al.* in 2004, who obtained a maximum *zT* of 0.87 at 715 K.[28]

In the present work, we report on the effects of doping In and Yb into $TlSbTe_2$. Indium prefers the +3 oxidation state, which is the same as that of Sb, so the substitution of In for Sb would not lead to a change in carrier concentration, but it may help to hamper phonon transfer in order to reduce the thermal conductivity. The preferred oxidation state of Yb is +2, which could be used to adjust the carrier concentration. Attempts with Sn and Pb resulted in the formation of side products, even at small concentrations of Sn/Pb. In addition, we optimized the consolidation process to achieve a denser pellet for better thermoelectric properties.

Since Sb_2Te_3[125], Bi_2Te_3[126] and $TlSbTe_2$[127] all crystallize in anisotropic structures, and polycrystalline $Bi_2Se_{0.3}Te_{2.7}$[128] and Bi_2Te_3[129] exhibit significant differences in their anisotropic physical properties measurements, we also investigated the anisotropy of the hot-pressed bulk $TlSbTe_2$.

5.2 Experimental Procedures

Stoichiometric amounts of the respective elements (Tl, granules, 6 mm,99.99%, Alfa Aesar; Sb power,100 mesh, 99.5%, Alfa Aesar; Te, broken ingots, 99.99%, Strem Chemicals; In powder,325 mesh,99.99%, Alfa Aesar; Yb powder,40 mesh, 99.9% (REO), Alfa Aesar) were weighed and placed into a silica tube in an argon filled glovebox. The tubes were heated up to 923 K for several hours and then water-quenched to room temperature.

The phase identification was performed, and the lattice parameters of the materials were obtained from General Structure Analysis System (GSAS)[46] using the EXPGUI interface[77] applying the LeBail method[130] .

For the anisotropy test, the bars were cut as shown in Figure 5-1. The current passed through Bar A (left) was perpendicular to the pressing direction, while that for Bar B (right) was parallel to the pressing orientation.

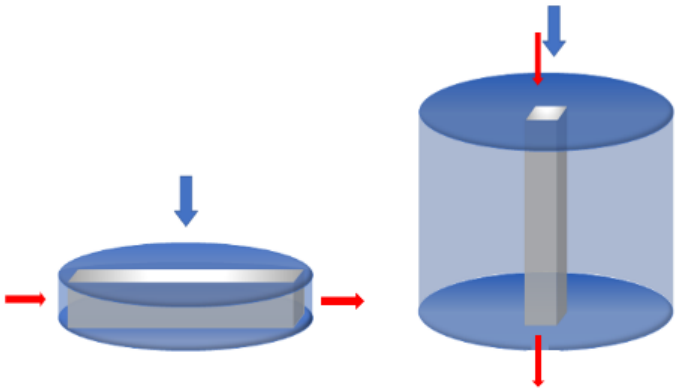

Figure 5-1: A schematic drawing for the cutting methods and the current flow directions used for the anisotropy test. The blue arrows illustrate the hot-pressing direction, and the red arrows demonstrate the direction of the applied current.

5.3 Results and Discussion

Powder X-ray diffraction patterns of the doped and undoped samples are presented in Figure 5-2. We did not use more than 3% In, because at that concentration extra peaks showed up in the PXRD, indicating that we went passed the solubility limit. The lattice parameter of the obtained materials did not exhibit any systematic changes (Table 5-1), which may be due to the small amounts of the dopants and the in part similar atomic radii. The refined powder diagrams can be found in Appendix Figure A7-A10.

Table 5-1: Refined Lattice Parameters.

Material	*a* (Å)	*α* (°)	*V* (Å^3)
Undoped $TlSbTe_2$	8.1229(3)	31.361(1)	128.850(1)
"$Tl_{0.98}In_{0.02}SbTe_2$"	8.1218(2)	31.367(1)	128.839(1)
"$TlSb_{0.98}In_{0.02}Te_2$"	8.1407(9)	31.494(1)	130.740(1)
"$Tl_{0.98}Yb_{0.02}SbTe_2$"	8.1329(5)	31.362(1)	129.330(1)

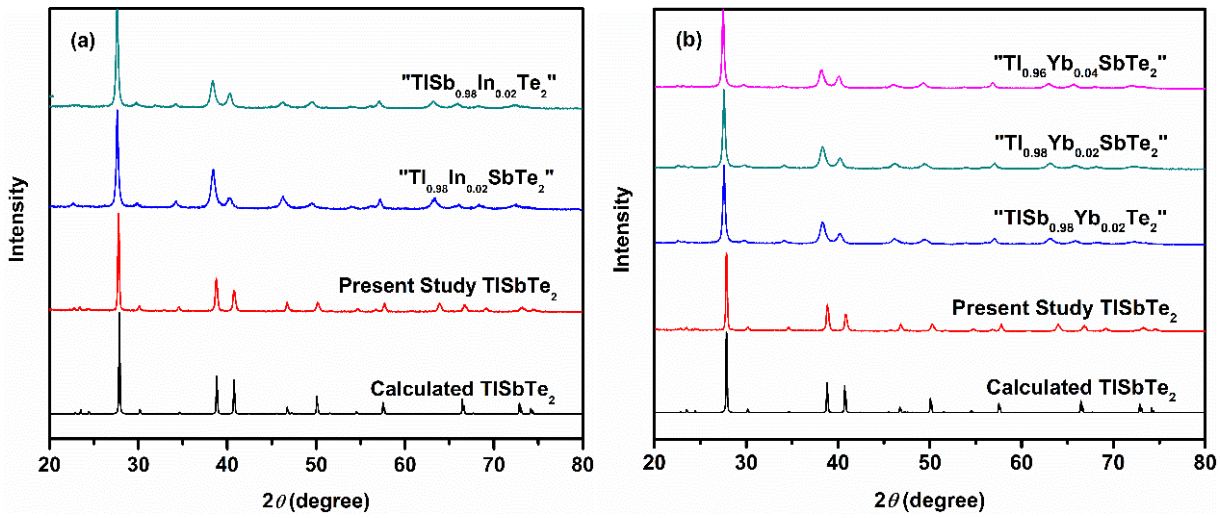

Figure 5-2: Left: Powder X-ray diffraction patterns for In-doped, and right: Yb-doped $TlSbTe_2$ samples.

Both $TlSbTe_2$ and Bi_2Te_3 crystallize in the rhombohedral crystal system, shown in Figure 5-3 in the hexagonal setting. The structures can both be described based on hexagonal close packing of Te atoms, with the cations in octahedral voids. Along the *c* axis, the sequence of the close-packed layers is Te-Tl-Te-Sb-Te-Tl-Te-Sb-...in $TlSbTe_2$ and Te-Bi-Te-Bi-Te-Te-Bi-Te-Bi-Te- in case of Bi_2Te_3. Each layer between two Te layers is filled with cations (either with Tl or with Sb) in case of $TlSbTe_2$, whereas every third layer between two Te layers is empty in Bi_2Te_3. Therefore, a different bonding situation exists in Bi_2Te_3, where the 5-layer sandwiches Te-Bi-Te-Bi-Te are held together only by van der Waals interactions, whereas there are always cation-anion bonds between the layers of $TlSbTe_2$. The former gives rise to significant differences in the physical properties measured parallel to the *ab* plane and to the *c* axis in case of Bi_2Te_3. Both the electrons and the phonons can travel faster parallel in the *ab* plane, resulting in a larger electrical and thermal conductivity in this direction. The electrical conductivity and thermal conductivity measured in plane of Bi_2Te_3 can be more than twice as high as measured out of plane, depending on the particle size and pressure utilized for sintering and temperature[131,132].

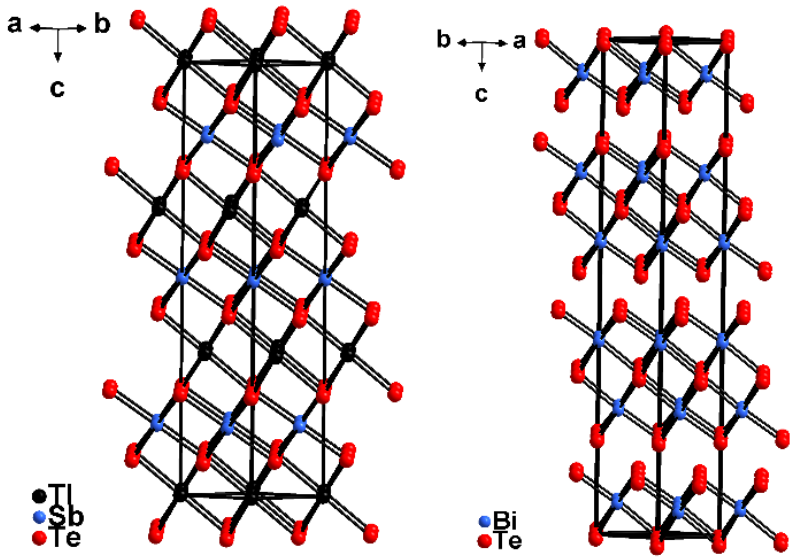

Figure 5-3: Crystal structure of $TlSbTe_2$ (left) and Bi_2Te_3 (right).

The electrical conductivity of undoped $TlSbTe_2$ decreases with an increasing temperature, as shown in Figure 5-4a, indicating its extrinsic semiconductor behavior. The electrical conductivity of $TlSbTe_2$ is about 750 Ω^{-1} cm^{-1} at 380 K, which is significantly higher than the 379 Ω^{-1} cm^{-1} of $AgSbTe_2$ prepared by a high pressure apparatus[133] and the 135 Ω^{-1} cm^{-1} of $AgSbTe_2$ prepared by melt spinning[134]. However, at around 520 K, the electrical conductivity of high pressure and high temperature prepared $AgSbTe_2$ is higher with 340 Ω^{-1} cm^{-1}, compared to $TlSbTe_2$ n with 280 Ω^{-1} cm^{-1} and $AgSbTe_2$ prepared by melt spinning with 175 Ω^{-1} cm^{-1}. At 380 K and 500 K, the electrical conductivity values of $TlSbTe_2$ are 750 and 300 Ω^{-1} cm^{-1}, which are much higher than that of Tl_9SbTe_6 with approximately 390 and 226 Ω^{-1} cm^{-1}[161]. $SnBi_2Te_4$, which also adopts a layered structure, exhibits a lower electrical conductivity at 380 K with 675 Ω^{-1} cm^{-1}, but higher at 500 K with 550 Ω^{-1} cm^{-1}.[135]

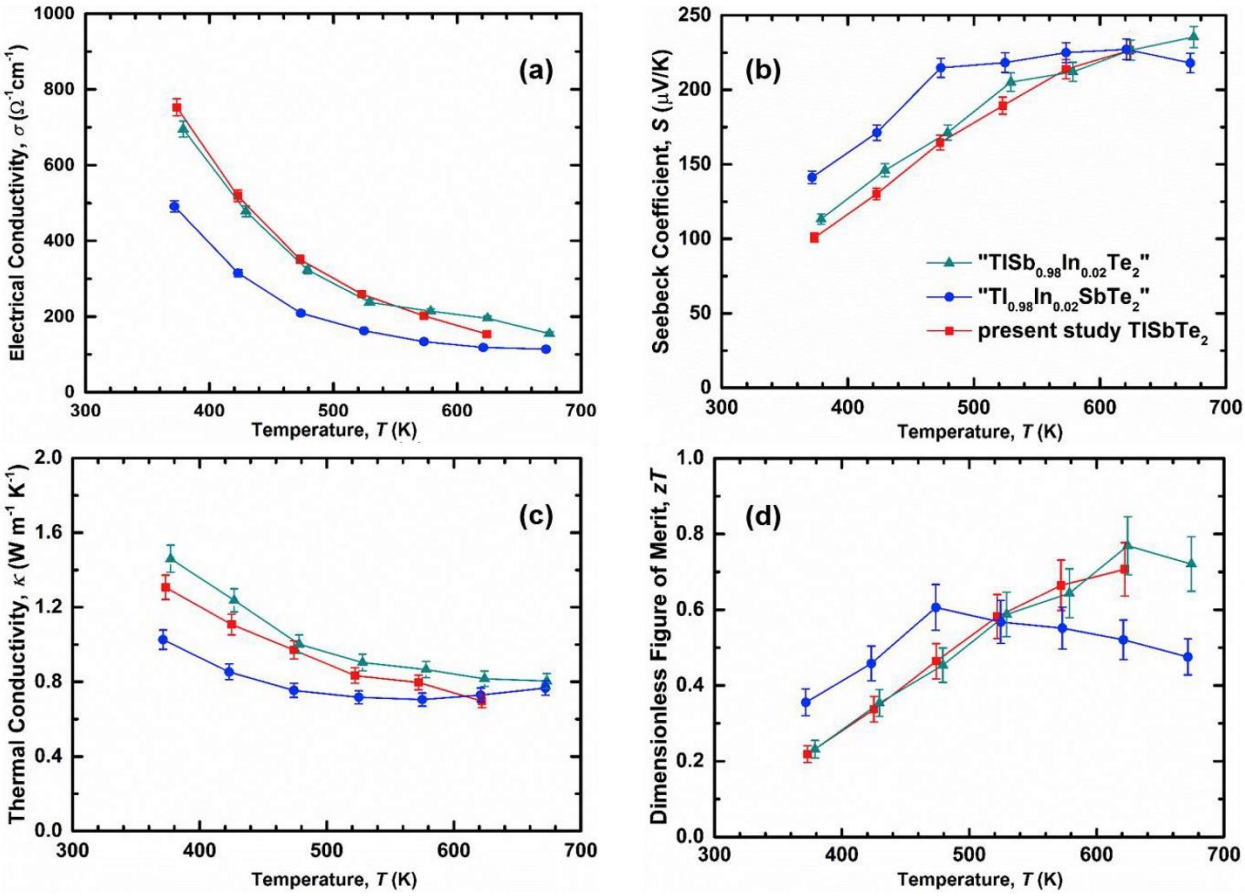

Figure 5-4: Temperature dependence of (a) electrical conductivity, (b) Seebeck coefficient, (c) thermal conductivity, and (d) figure of merit for present study $TlSbTe_2$ (red) and In-doped "$Tl_{0.98}SbIn_{0.02}Te_2$" (blue), and "$TlSb_{0.98}In_{0.02}Te_2$" (dark cyan).

This extrinsic semiconducting behavior was also revealed in other seemingly stoichiometric antimony or bismuth chalcogen-ides, such as in Bi_2Se_3[136], Bi_2Te_3[136,137], and Sb_2Te_3[43,136,138]. In these compounds, deviations from the ideal stoichiometry were often observed, as a result of an excess of the more electronegative element. This can further be explained by anti site defects: in case of Bi_2Te_3, Bi on a Te site (BiTe) can give rise to one hole, and TeBi provides one extra electron. Thusly both *p*- and *n*-type can be prepared. For Sb_2Te_3, only *p*-type thus far was obtained, because SbTe is preferred. For Bi_2Se_3, only *n*-type was observed experimentally, because SeBi and vacancies on the Se sites are the dominant defects. Moreover, Bi_2Se_3, Sb_2Te_3,

and Bi_2Te_3, always exhibit extrinsic conductivity behaviors rather than being intrinsically semiconducting. Like in Sb_2Te_3, SbTe is a likely defect, leading to the observed extrinsic *p*-type behavior. There is a similar effect for $AgSbTe_2$, whose pressed, formally undoped sample possessed a carrier concentration about 5×10^{19} cm^3.[134]

The Seebeck coefficient of undoped $TlSbTe_2$ increases with temperature (Figure 5-4b). Compared to other antimony/bismuth tellurides at 372 K, its Seebeck coefficient (S = 101 μV K^{-1}) is lower than that of Tl_9SbTe_6 (130 μV K^{-1}) ,[61] $SnBi_2Te_4$ (330 μV K^{-1}),[135] and $AgSbTe_2$ (265 μV K^{-1}).[44] At 622 K, its Seebeck value (227 μV K^{-1}) is higher than $SnBi_2Te_4$ (165 μV K^{-1}),[135] and $AgSbTe_2$ (265 μV K^{-1}).[44] The thermal conductivity slowly decreases from 1.31 W m^{-1} K^{-1} at 373 K to 0.70 W m^{-1} K^{-1} at 622 K (Figure 5-4c). Compared to other antimony/bismuth tellurides at 372 K, its thermal conductivity is higher than that of Tl_9SbTe_6 (0.62 W m^{-1} K^{-1}),[61] $SnBi_2Te_4$ (0.8 W m^{-1} K^{-1}),[135] and $AgSbTe_2$ (0.59 W m^{-1} K^{-1}).[44] At 622 K, its thermal conductivity is lower than that of $SnBi_2Te_4$ (1.6 W m^{-1} K^{-1}),[135] and higher than $AgSbTe_2$ (0.57 W m^{-1} K^{-1}).[44]

When doping In into the Tl site, we nominally inserted more electrons into the system, reducing the hole concentration. Correspondingly, the electrical conductivity of "$Tl_{0.98}In_{0.02}SbTe_2$" is decreased compared to the undoped $TlSbTe_2$, as shown in Figure 5-4a. At about 372 K, the electrical conductivity of "$Tl_{0.98}In_{0.02}SbTe_2$" is approximately 490 Ω^{-1} cm^{-1}, which is roughly 35% lower than the undoped sample; however, at 620 K, the difference is lowered down to 23%, where the formally undoped sample and "$Tl_{0.98}In_{0.02}SbTe_2$" exhibit σ = 154 Ω^{-1} cm^{-1} and 118 Ω^{-1} cm^{-1}, respectively. For "$TlSb_{0.98}In_{0.02}Te_2$", σ decreases from 695 Ω^{-1} cm^{-1} at 379 K to 155 Ω^{-1} cm^{-1} at 675 K, which is very comparable to the undoped sample through the whole measured temperature range.

A lower carrier concentration gives rise to a larger Seebeck coefficient, in accordance with the trends depicted in Figure 5-4b. "$Tl_{0.98}In_{0.02}SbTe_2$" has a Seebeck coefficient of 141 μV K^{-1} at 372 K, which is 40% higher than S = 101 μV K^{-1} of the undoped sample at that temperature. Their difference decreases as temperature increases, and at about 623 K, the Seebeck coefficient values of both samples reach 227 μV K^{-1}. The Seebeck coefficient of "$Tl_{0.98}In_{0.02}SbTe_2$" achieves its local maximum at this temperature, and a band gap of 0.28 eV is estimated via Goldsmid-Sharp: $E_g = 2e|S_{max}|T_{max}$.[139] For "$TlSb_{0.98}In_{0.02}Te_2$", the Seebeck coefficient increases from 113 to 235 μV K^{-1}, which is almost equivalent to the Seebeck curve of the undoped sample. When In is doped into the Sb site, the electrical conductivity and Seebeck coefficient do not change significantly in comparison to undoped $TlSbTe_2$, because we substitute one trivalent cation for another trivalent cation.

Lower carrier concentration occurs with lower κ_e, and thus also lower κ, in agreement with the data presented in Figure 5-4c. The thermal conductivity of "$Tl_{0.98}In_{0.02}SbTe_2$" decreases from 1.03 W m^{-1} K^{-1} at 371 K to its local minimum of 0.70 W m^{-1} K^{-1} at 575 K. For the undoped sample and "$TlSb_{0.98}In_{0.02}Te_2$", the thermal conductivity decreases with increasing temperature, and the values of "$TlSb_{0.98}In_{0.02}Te_2$" are slightly higher. At about 375 K and 623 K, the total thermal conductivity of the undoped sample and "$TlSb_{0.98}In_{0.02}Te_2$" are 1.31 and 1.46 W m^{-1} K^{-1} (11% difference), and 0.70 and 0.82 W m^{-1} K^{-1} (17% difference), respectively.

zT of "$Tl_{0.98}In_{0.02}SbTe_2$" increases to a maximum value of 0.61 at 480 K and then starts to decrease. It remains higher than the zT of undoped $TlSbTe_2$ until 530 K (zT = 0.59), as presented in Figure 5-4d. The maximum zT = 0.71 of the undoped sample and zT = 0.77 of "$TlSb_{0.98}In_{0.02}Te_2$" are obtained at about 622 K, with the difference of 8.5% being within experimental error.

Doping with Yb apparently has a smaller impact than doping with In. For the most part, the electrical conductivity data are equal within experimental error (Figure 5-5a), independent of the Yb concentration and whether Yb was planned to replace Tl or Sb. This can a consequence of self-compensation, or of Yb as a divalent cation replacing the monovalent Tl and trivalent Sb in equal amounts. Slight changes in the temperature dependence, however, cause the sample with nominally 2% Yb on the Tl site to exhibit the largest electrical conductivity at 625 K, namely 218 Ω^{-1} cm^{-1} compared to 154 Ω^{-1} cm^{-1} of undoped $TlSbTe_2$. The Seebeck coefficient of the undoped $TlSbTe_2$ is 227 µV K^{-1} at 625 K, which is slightly albeit significantly higher than 213 µV K^{-1} of "$Tl_{0.98}Yb_{0.02}SbTe_2$". The thermal conductivity of undoped $TlSbTe_2$, κ = 0.70 W m^{-1} K^{-1}, is insignificantly larger than the 0.68 W m^{-1} K^{-1} of "$Tl_{0.98}Yb_{0.02}SbTe_2$". "$Tl_{0.98}Yb_{0.02}SbTe_2$" achieves the overall highest zT at around 625 K (zT_{max} = 0.85; Figure 5(d)), and the highest zT was improved by 22% at 625 K after replacing 0.02 Tl per formula unit Yb.

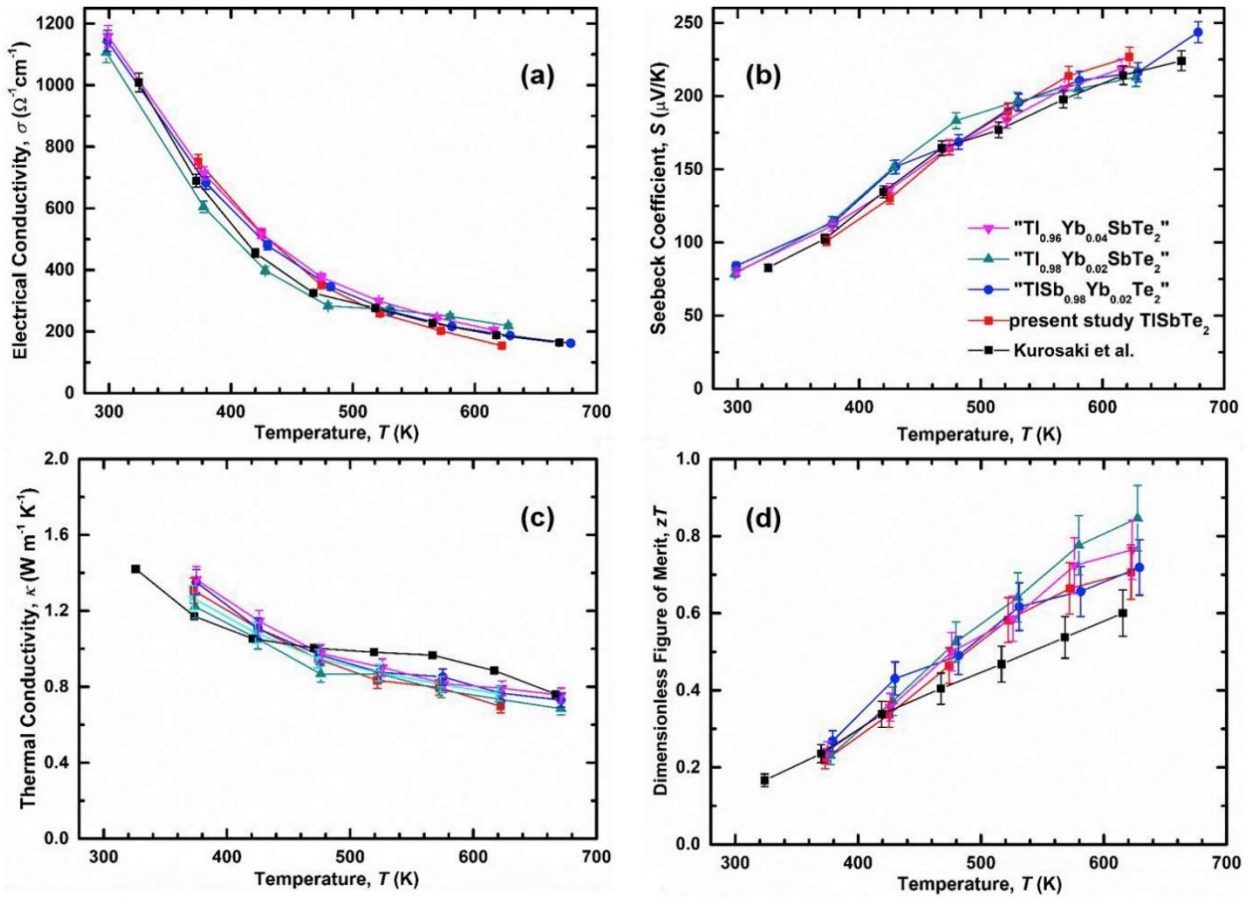

Figure 5-5: Temperature dependence of (a) electrical conductivity, (b) Seebeck coefficient, (c) thermal conductivity, and (d) figure of merit for Kurosaki et al. (black), present study $TlSbTe_2$ (red) and Yb-doped "$TlSb_{0.98}Yb_{0.02}Te_2$" (blue), "$Tl_{0.98}Yb_{0.02}SbTe_2$" (dark cyan). "$Tl_{0.96}Yb_{0.04}SbTe_2$" (magenta).

Next, we compare undoped $TlSbTe_2$ in the present study with the data from Kurosaki *et al.* The electrical conductivity and See-beck coefficient are very comparable, with our Seebeck coefficient being slightly higher and our electrical conductivity slightly lower, indicative of a smaller carrier concentration, i.e. fewer defects. The physical properties at 625 K for "$Tl_{0.98}Yb_{0.02}SbTe_2$", present study $TlSbTe_2$, and literature $TlSbTe_2$ are summarized in Table 1. The electrical conductivity of present study $TlSbTe_2$, σ = 154 Ω^{-1} cm^{-1}, is 20% lower than the 188 Ω^{-1} cm^{-1} of the literature $TlSbTe_2$; while the Seebeck coefficient of present study $TlSbTe_2$, S = 226 μV K^{-1}, is 5% higher than the 214 μV $K^{-1}$of the literature $TlSbTe_2$. The power factor of present study

$TlSbTe_2$ is 794 μW m^{-1} K^{-2}, which is roughly 10% lower than that of the literature $TlSbTe_2$, 860 μW m^{-1} K^{-2}. Correspondingly the thermal conductivity of our sample is lower, especially at elevated temperatures.

Table 5-2: Thermoelectric properties compared at 625 K.

	κ (W m^{-1} K^{-1})	**σ (Ω^{-1} cm^{-1})**	**S (μV K^{-1})**	***P.F.* (μW m^{-1} K^{-2})**	***zT***
literature $TlSbTe_2$	0.87	18	214	860	0.61
present study $TlSbTe_2$	0.7	154	227	794	0.71
"$TlSb_{0.98}In_{0.02}Te_2$"	0.82	196	227	1010	0.77
"$Tl_{0.98}Yb_{0.02}SbTe_2$"	0.73	218	213	990	0.85

zT obtained by Kurosaki *et al.* the undoped $TlSbTe_2$ in the present study, and the 2% Yb-doped sample are compared in Table 5-1. The overall enhancement in *zT* at about 620 K is almost 40%, by means of doping with Yb and optimizing the preparation conditions.

Compared to other advanced bulk state-of-the-art p-type thermoelectric materials at 620 K, such as zT = 0.45 for β-Cu_2Se[58], zT = 0.65 for ZnSb,[140] zT = 0.8 for PbTe,[141] zT = 1.6 for $AgSbTe_2$ prepared by melt spinning,[134] "$Tl_{0.98}Yb_{0.02}SbTe_2$" exhibits a competitive performance near 620 K with a value of 0.85. In addition, compared to other promising thallium telluride thermoelectric materials, this value is comparable to zT = 0.90 achieved by Tl_9SbTe_6 at 500 K,[61] and lower than zT = 1.1 of Tl_9BiTe_6 at 500 K,[61] zT = 1.26 of $Tl_{8.05}Sn_{1.95}Te_6$ at 700 K,[25] zT = 1.46 of $Tl_{8.10}Pb_{1.90}Te_6$ at 700 K,[25] and zT = 1.1 of $Tl_2Ag_{12}Te_{7-\delta}$ at 520 K.[142]

To test if the pressing procedure produced any preferred orientation for the polycrystalline pressed samples, potentially resulting in anisotropic behavior of the pressed pellets, we cut the "$Tl_{0.98}Yb_{0.02}SbTe_2$" samples in two different orientations, one perpendicular

to the pressing direction (Bar A, also shown in Figure 4), and the other one (Bar B) parallel to that direction, as described in the experimental procedures. The electrical conductivity and the Seebeck coefficient are not significantly different for the two differently pressed bars (Figure 6). This is likely a consequence of the three-dimensional network of Tl−Te and Sb−Te bonds, in contrast to the two-dimensional structure of Bi_2Te_3.

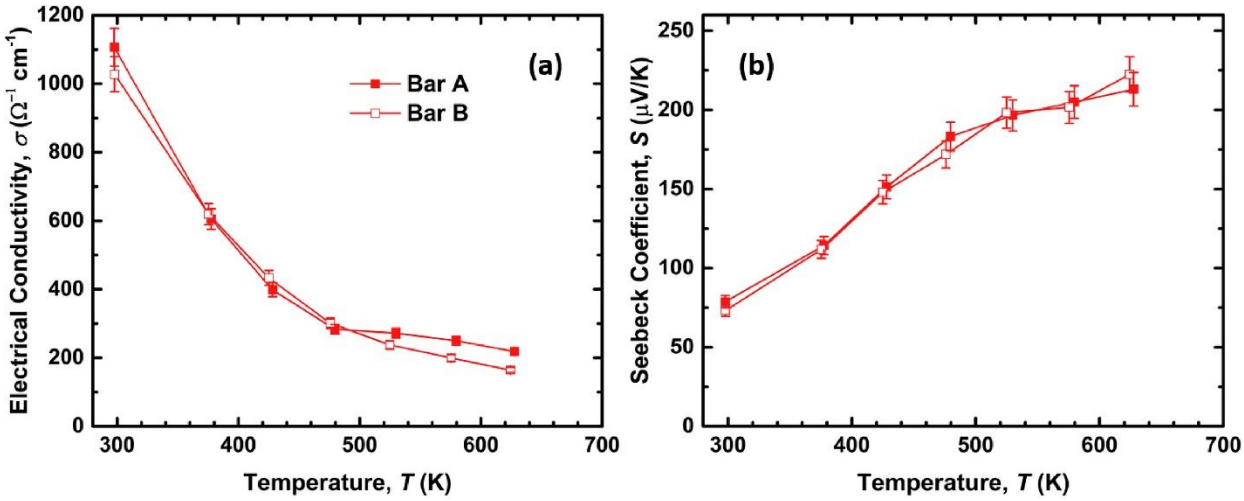

Figure 5-6: Temperature dependence of (a) electrical conductivity and (b) Seebeck coefficient of "$Tl_{0.98}Yb_{0.02}SbTe_2$", where Bar A was cut perpendicular to the pressing direction and Bar B was cut parallel to the pressing direction.

5.4 Conclusions

$TlSbTe_2$ is an extrinsic *p*-type semiconductor, bestowed with low thermal conductivity and moderate power factor. Compared to earlier work by Kurosaki *et al.*, we have achieved an improvement in *zT* by roughly 40% (from 0.61 to 0.85) at 625 K in *p*-type $TlSbTe_2$ by means of a partial substitution of Tl with Yb and optimizing the fabrication. In addition, we found that despite the layered character of these materials, the polycrystalline pressed pellets did not exhibit any distinct anisotropies, advantageous for device fabrication.

Chapter 6: Thermoelectric Properties of $Tl_4Ag_{18}Te_{11}$

6.1 Introduction

There are only two *n*-type thallium tellurides reported thus far, namely $TlBiTe_2$ and $Tl_2HgGeTe_4$, with only the thermoelectric properties of $TlBiTe_2$ determined at high temperatures.[26,143,144] Examples of state-of-the-art *n*-type thermoelectric materials include bismuth telluride,[128,145] lead telluride,[146,147] filled skutterudites[148,149] and Bi-doped magnesium silicide stannides,[14,150] all with *zT* values above unity. This chapter introduces the hitherto unknown properties of the *n*-type $Tl_4Ag_{18}Te_{11}$, which exhibits an ultralow thermal conductivity.

6.2 Experimental Procedures

The compounds were obtained via solid-state synthesis: stoichiometric amounts of the respective elements (Tl, granules, 6 mm, 99.99%, Alfa Aesar; Ag ingots, 100 mesh, 99.5%, Alfa Aesar; Te, broken ingots, 99.99%) were weighed. The tubes were heated up to 923 K for several hours in a resistance furnace, and then water-quenched to room temperature. The yielded ingots were ground into fine powder and annealed at 573 K for 72 hours. The densities for all the presented samples were higher than 95% of the theoretical density (8.43 g cm^{-3}).

The electronic structure of $Tl_4Ag_{18}Te_{11}$ was computed utilizing the WIEN2k package applying the full-potential linearized augmented plane wave (FP-LAPW) method with the density functional theory (DFT).[82,151] The generalized gradient approximation (GGA) from Perdew, Burke and Ernzerhof (PBE) was utilized for exchange and correlation energies.[80] Afterwards, the

modified Becke–Johnson (mBJ) potential was applied to obtain a more reliable band gap. For the self-consistent energy calculations, 99 independent k points were selected on a grid of 10 × 10 × 10 points spread out evenly throughout the Brillouin zone. The energy convergence was set to be 104 Ry for the self consistency.

Both DSC and TG were performed on an 80 mg powder sample of the nominal stoichiometry of $Tl_4Ag_{18}Te_{11}$. The measurement was conducted with a heating rate of 20 K min^{-1} up to 773 K. Low temperature specific heat measurements were performed with a Quantum Design PPMS Dynacool at WATLab. The experimentally determined *C* reached a plateau at 0.192 J g^{-1} K^{-1} (Figure 6-1), supporting the validity of using the Dulong–Petit value.

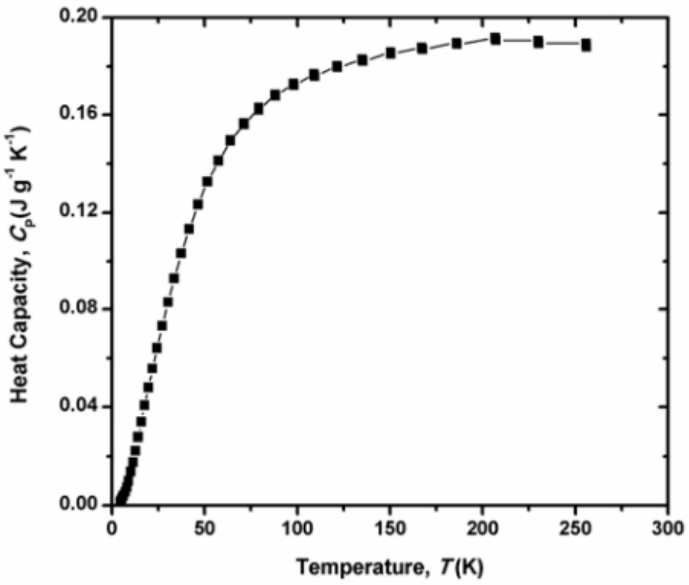

Figure 6-1: Specific heat of "$Tl_{4.05}Ag_{18}Te_{11}$".

6.3 Results and Discussion

In 1992, Moreau *et al*. determined the crystal structure of $Tl_4Ag_{18}Te_{11}$.[70] This crystal structure consists of $AgTe_4$ tetrahedra interconnected in three dimensions with Tl cations

occupying tunnels of this framework (Figure 6-2). The space group of $Tl_4Ag_{18}Te_{11}$ is $F\bar{4}3m$, a subgroup of the $K_4Ag_{18}Te_{11}$ space group $Fm\bar{3}m$,[152] due to the disordered Tl atom positions occupying an additional Wyckoff site. The lattice parameter of $Tl_4Ag_{18}Te_{11}$ was published to be a = 18.717(8) Å, and the unit cell volume V = 6557.1 Å^3. The Tl atom positions in the cubic (Tl1 atoms) and antiprismatic (Tl2 atoms) voids are 100% occupied, but disordered within the cuboctahedral (Tl3 atoms) voids. In $K_4Ag_{18}Te_{11}$, all the potassium atoms were determined to be located in the centers of the respective polyhedra. However, the large anisotropic displacement parameter of the K3 atom (U_{eq} = 0.067(6) Å^2, compared to K1 with 0.016(2) Å^2 and K2 with 0.013(1) Å^2), may indicate a tendency towards disorder in that cage as well.

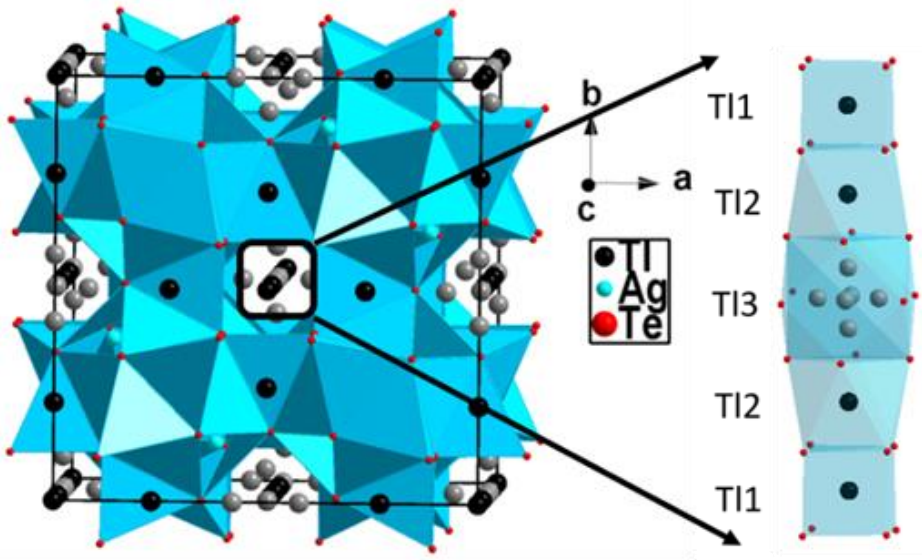

Figure 6-2: Left: crystal structure of $Tl_4Ag_{18}Te_{11}$. Blue polyhedra; $AgTe_4$ tetrahedra; grey circles: disordered Tl3 atoms; right: arrangements of Tl atoms in the chain along the c axis.

The shortest distance between the Tl2 atom and the disordered Tl3 atom is 3.57 Å as a consequence of its displacement from the center of its polyhedron. Typical homonuclear Tl–Tl distances in thallium chalcogenides, such as Tl_5Te_3,[153] Tl_9BiTe_6,[117] and Tl_4ZrTe_4,[154] are in the range of 3.5 Å to 4.0 Å. While the cuboctahedron cannot accommodate two Tl atoms, two Ag atoms

would fit, with an Ag–Ag distance of 3.0 Å, thereby allowing for a cation excess and thus extra electrons causing *n*-type conduction.

The Tl1–Te distances in the $Tl1Te_6$ cube are between 3.47 Å and 3.58 Å, and the Tl2–Te distances in the $Tl2Te_6$ antiprism between 3.62 Å and 3.69 Å. On the other hand, the Tl3 atoms occupy the void in a cuboctahedron, whose center is too far away (5.04 Å) from the surrounding twelve Te atoms for regular Tl3–Te bonds. Consequently, the Tl3 positions were refined to be disordered in that cage, resulting in six sites, each with a 16.7% occupancy. Each of these sites participates in four short Tl3–Te bonds of 3.32 Å, and larger contacts with the next four Te atoms at a distance of 4.42 Å. This situation is reminiscent of the guest atoms in the icosahedral cages of the filled skutterudites[71–73] and in the tetrakaidecahedral holes of the clathrates.[4,74,75]

The distances between all the Te atoms are larger than 4 Å, so their oxidation states are assigned as Tl^+, Ag^+, and Te^{2-}, resulting in a charge balanced formula of $(Tl^+)_4(Ag^+)_{18}(Te^{2-})_{11}$. The Ag atoms in this compound form Ag_{12} clusters that are three-dimensionally interconnected by Ag_2 dumbbells. d^{10}–d^{10} Ag–Ag interactions of the order of 3 Å are thus present in this structure, which are common in silver chalcogenides, such as $Tl_2Ag_{12}Te_7$,[142] $Tl_2Ag_{12}Se_7$, $K_4Ag_{18}Te_{11}$, and $TlNdAg_2S_3$.[155]

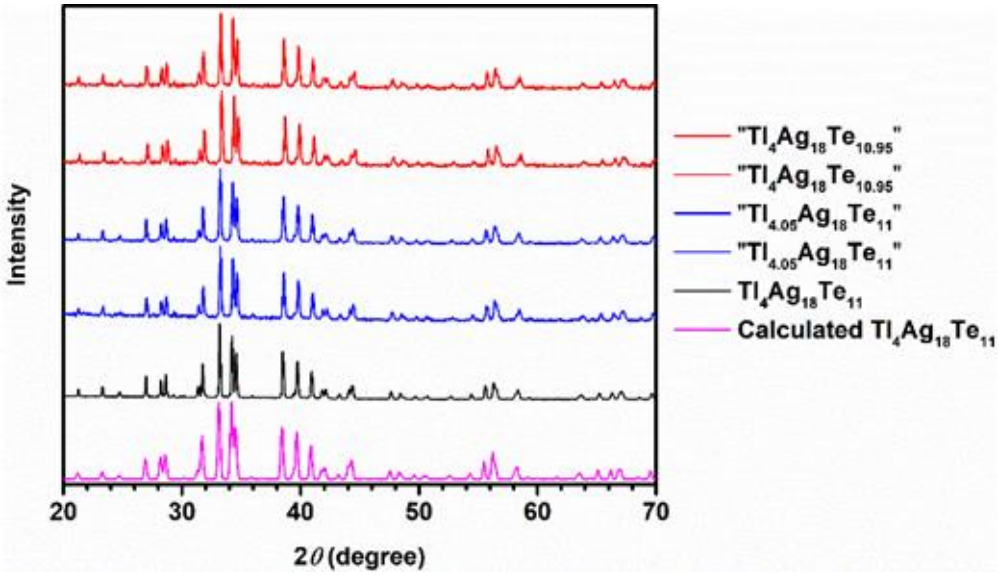

Figure 6-3: PXRD pattern of calculated $Tl_4Ag_{18}Te_{11}$, experimental $Tl_4Ag_{18}Te_{11}$, "$Tl_{4.05}Ag_{18}Te_{11}$", "$Tl_4Ag_{18}Te_{10.95}$", and repeat samples of the latter two.

The PXRD patterns of the synthesized samples are presented in Figure 6-3. No significant amount of impurities or side products were detected in any sample. The atomic percentages (at%) obtained by EDX analysis are presented in Table 6-1. The amount of Te is very close to the nominal percent for all the samples. The at% of Tl are between 0.4–0.7% higher and 0.3–0.5% lower than the theoretical percentages in case of Ag. The two samples with the same nominal formula reveal similar elemental ratios, indicating the samples are reproducible. The standard deviations are 0.1–0.6%, demonstrating that homogeneous samples were obtained. The elemental distribution of "$Tl_{4.05}Ag_{18}Te_{11}$" are quite even and presented in Figure 6-4.

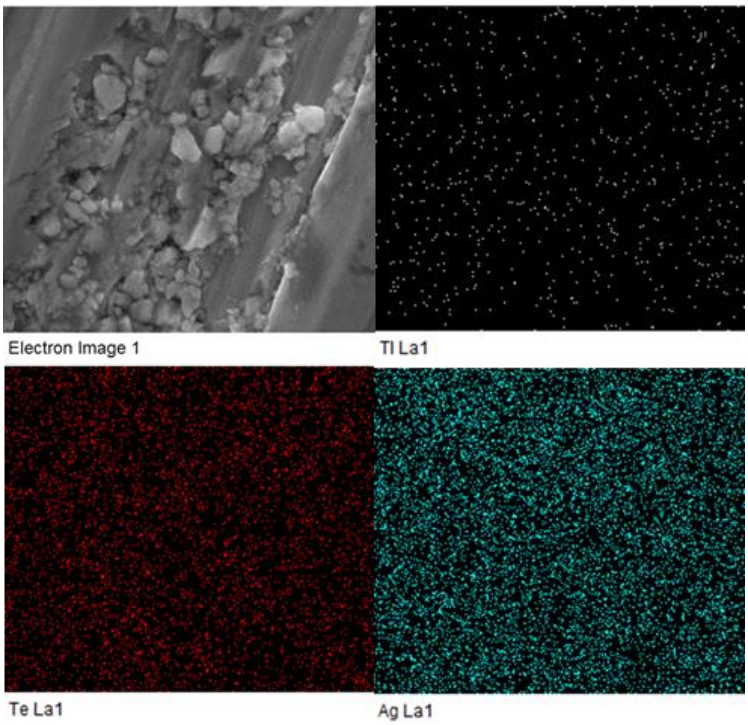

Figure 6-4: EDX images of "$Tl_{4.05}Ag_{18}Te_{11}$". Each image corresponds to a width of 13 μm.

Table 6-3: Experimental atomic-% (standard deviation)/nominal at-% of the different elements determined via EDX

		at.-% Tl	at.-% Ag	at.-% Te
	$Tl_4Ag_{18}Te_{11}$	12.8(1)/12.1	53.9(2)/54.5	33.3(2)/33.3
■	**"$Tl_{4.05}Ag_{18}Te_{11}$"**	12.7(4)/12.3	54.0(4)/54.5	33.4(2)/33.3
★	**"$Tl_{4.05}Ag_{18}Te_{11}$"**	12.7(2)/12.3	54.1(3)/54.5	33.3(1)/33.3
■	**"$Tl_4Ag_{18}Te_{10.95}$"**	12.7(4)/12.1	54.2(6)/54.6	33.1(2)/33.2
★	**"$Tl_4Ag_{18}Te_{10.95}$"**	12.5(6)/12.1	54.3(6)/54.6	33.1(2)/33.2

The electronic structure is determined based on an *I*4*mm* space group model, where one of the six disordered Tl3 sites are treated as 100% occupied, with the other five removed, as shown in Figure 6-5a. The density of states (DOS) of $Tl_4Ag_{18}Te_{11}$ is shown in Figure 6-5b. From 6.5 eV to 3 eV, the DOS is dominated by Ag-*d* orbitals, from 2 eV to the Fermi level (E_F), it is mainly composed of Te-*p* orbitals and Ag-*d* orbitals and above E_F to 3 eV, the states contain (empty) Ag-

s and Ag-*p* states, with some contributions from covalent mixing with Te-*p* states. The Tl states have only negligible contributions, partially caused by the small ratio of Tl in this material and the Tl-*s* states appearing to be below the selected energy range. The band structure (shown in Figure 6-5c) reveals a zero band gap, with the valence band slightly in contact with the conduction band without any overlapping, notably known as the Dirac-semimetallic band structure. A similar band structure was determined for $K_4Ag_{18}Te_{11}$, with zero band gap. The flat bands just below the Fermi energy and the steep bands just above the Fermi energy predict that this material could possibly possess a high Seebeck coefficient and a high electrical conductivity.

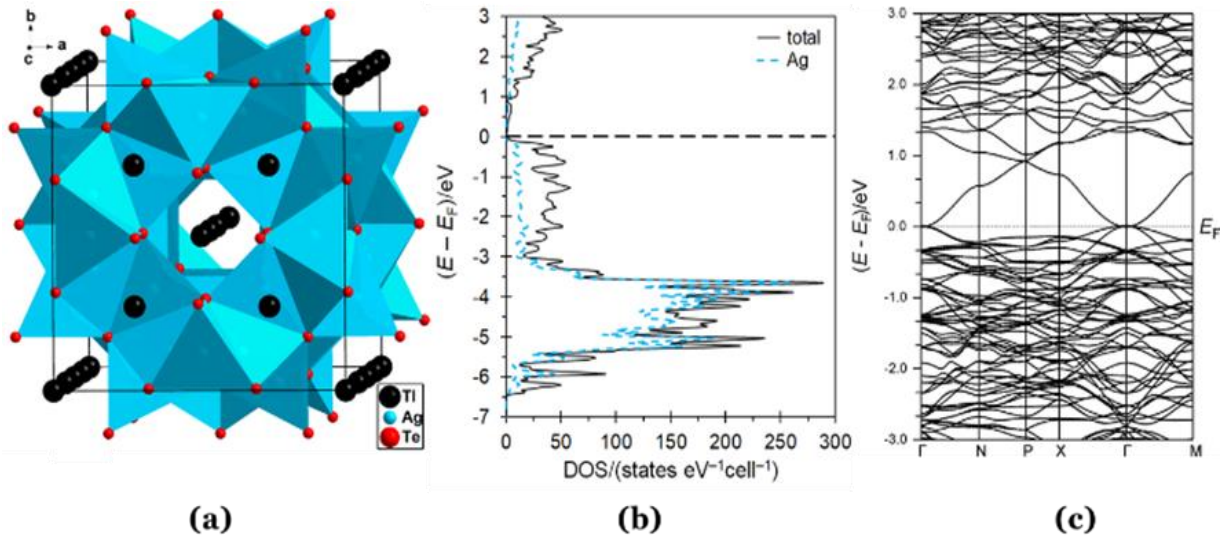

Figure 6-5: (a) I4mm structure model; (b) density of states (DOS); (c) band structure of the I4mm model of $Tl_4Ag_{18}Te_{11}$

The thermal behavior of $Tl_4Ag_{18}Te_{11}$ were investigated by DSC and TG measurements, and the data is plotted in Figure 6-6. The curve of TG indicates a weight gain smaller than 1%. The DSC curve reveals that $Tl_4Ag_{18}Te_{11}$ melts incongruently starting from 723 K. According to the Tl_2Te–Ag_2Te phase diagram published in 1990,[156] the melting processes can be interpreted as (with L = liquid):

At 723 K: $Tl_4Ag_{18}Te_{11} \rightarrow TlAg_{5.14}Te_{3.14} + L$

At 729 K: $TlAg_{5.14}Te_{3.14} \rightarrow TlAg_9Te_5 + L'$

At 780 K: $TlAg_9Te_5 \rightarrow Ag_2Te + L''$

(At 1228 K: $Ag_2Te \rightarrow L'''$)

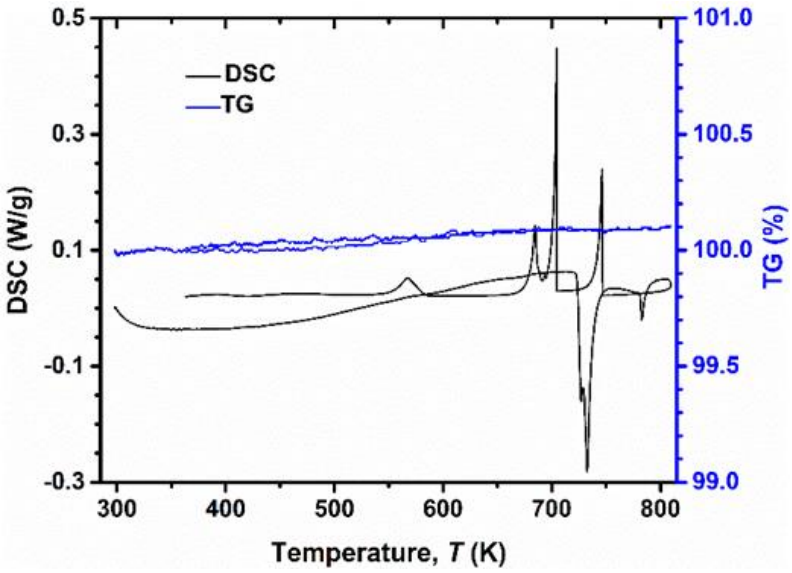

Figure 6-6: DSC and TG plots of $Tl_4Ag_{18}Te_{11}$.

However, the last process occurs outside of the temperature range we measured. The small exothermic peak presented at 570 K might correspond to the peritectic point of TlTe.[157] The PXRD pattern obtained after this DSC measurement reveals a mixture of phases caused by the fast cooling process going through peritectic points.

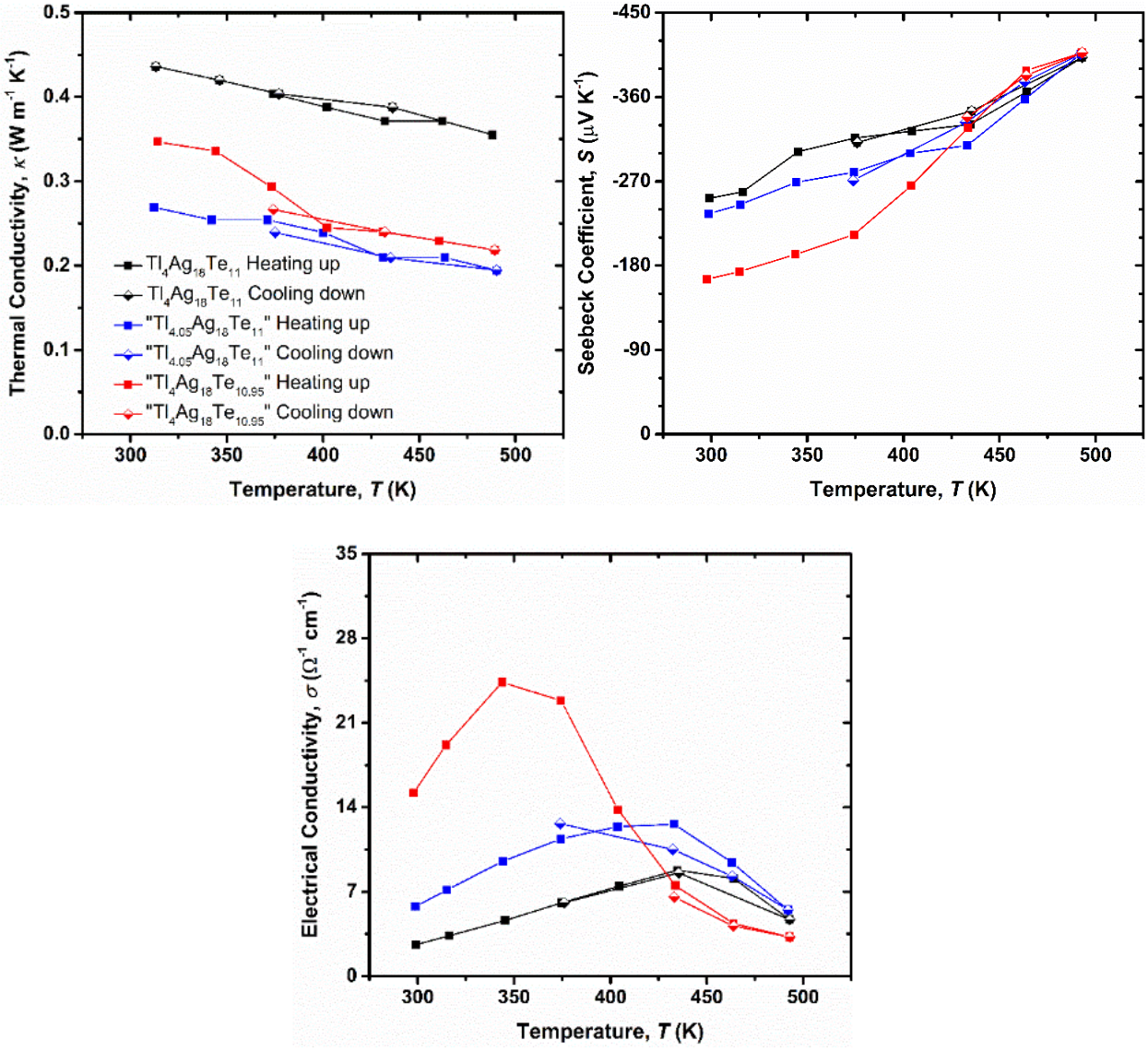

Figure 6-7: The properties measured as temperature increases and reduces.

All the physical properties obtained during cooling agree with the data obtained during heating, proving the data are reproducible (Figure 6-7). The Seebeck coefficients of all samples are negative (Figure 6-8a), which indicates that they are *n*-type semiconductors. This may be a consequence of a small amount of nonstoichiometric defects, such as two Ag cations replacing one Tl atom in the cuboctahedron of Te atoms, leading to a small amount of excess electrons.

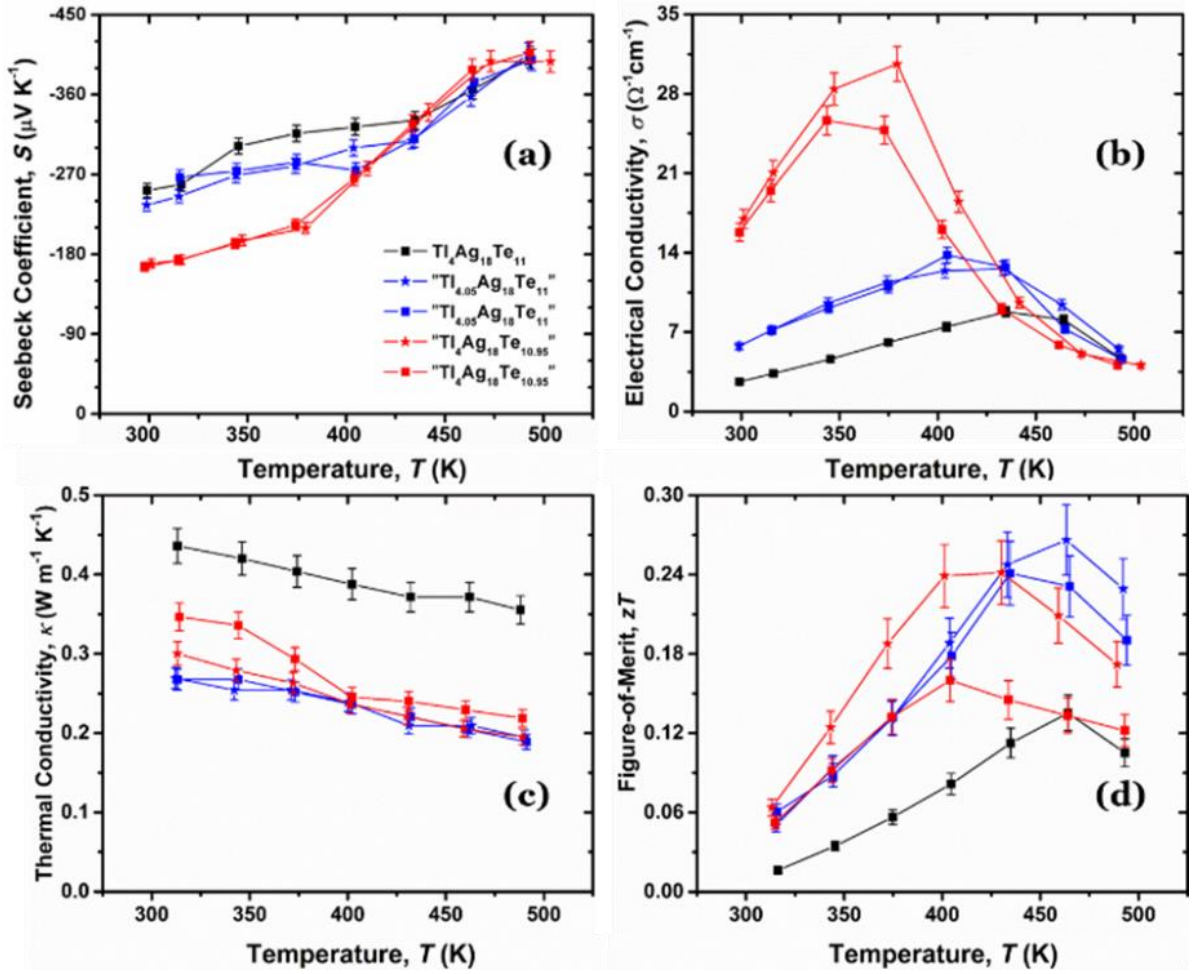

Figure 6-8: The physical properties of $Tl_4Ag_{18}Te_{11}$ (a) Seebeck coefficient, (b) electrical conductivity, (c) thermal conductivity, and (d) figure-of-merit versus temperature.

The absolute Seebeck values increase with a slower rate below 400 K, and then with a larger slope above 400 K. *S* of $Tl_4Ag_{18}Te_{11}$ ranges from -250 μV K^{-1} at room temperature to -400 μV K^{-1} at 500 K. The absolute Seebeck values of ''$Tl_{4.05}Ag_{18}Te_{11}$'' (with *S* = -240 μV K^{-1} at 300 K to *S* = -300 μV K^{-1} at 420 K) and ''$Tl_4Ag_{18}Te_{10.95}$'' (*S* = -160 μV K^{-1} at 300 K to -270 μV K^{-1} at 420 K) are both lower compared to $Tl_4Ag_{18}Te_{11}$ up to 420 K. Beyond that, all curves merge to equivalent values within experimental error. The maximum absolute Seebeck value of $TlBiTe_2$ is much lower than the one of $Tl_4Ag_{18}Te_{11}$ (with *S* = -75 μV K^{-1} at 760 K).[26] The absolute Seebeck coefficient values of $Tl_4Ag_{18}Te_{11}$ are also much higher than the values of $Mg_2Si_{0.325}Sn_{0.645}Bi_{0.03}$ (*S* = -115 μV K^{-}

[1] at 300 K to -215 μV K^{-1} at 773 K),[14] and the values of $Bi_2Te_{2.79}Se_{0.21}$ (*S* = -115 μV K^{-1} at 300 K to -150 μV K^{-1} at 540 K).[150]

As displayed in Figure 6-8b, the electrical conductivity of stoichiometric $Tl_4Ag_{18}Te_{11}$ increases as temperature increases to a maximum of σ = 9 Ω^{-1} cm^{-1} at 435 K, and then it starts to rapidly decrease. The four non-stoichiometric materials exhibit higher electrical conductivity at low temperature, indicative of more extrinsic charge carriers, in line with their lower absolute Seebeck values. For ''$Tl_{4.05}Ag_{18}Te_{11}$'', the electrical conductivity increases to a maximum of σ = 13 Ω^{-1} cm^{-1} at 435 K. For ''$Tl_4Ag_{18}Te_{10.95}$'', the electrical conductivity of the two different samples have some minor differences while generally exhibiting the same slope – the higher one reaches its electrical conductivity maximum value of 31 Ω^{-1} cm^{-1} at 380 K, which is almost 30 times lower than in $TlBiTe_2$,[26] 40 times lower than in $Bi_2Te_{2.79}Se_{0.21}$,[150] and 70 times lower than in $Mg_2Si_{0.325}Sn_{0.645}Bi_{0.03}$.[14] The differences between these two samples with the same nominal formula ''$Tl_4Ag_{18}Te_{10.95}$'' may be caused by weighing errors leading to small differences in the actual composition. E.g., an error of 0.5 mg would correspond to 0.09% Tl or 0.05% Te. Above 425 K, the electrical conductivity curves of all materials merge together, because more intrinsic charge carriers are thermally activated, eliminating the differences in the initial carrier concentration.

The samples all possess very low thermal conductivity for the whole temperature range, and their thermal conductivity decreases as temperature increases due to increased phonon Umklapp scattering,[158] as shown in Figure 6-8c. The thermal conductivity of $Tl_4Ag_{18}Te_{11}$ ranges from 0.44 W m^{-1} K^{-1} at 320 K to 0.35 W m^{-1} K^{-1} at 500 K. The thermal conductivity of ''$Tl_{4.05}Ag_{18}Te_{11}$'' is the lowest in this series, ranging from 0.27 W m^{-1} K^{-1} at 320 K to 0.19 W m^{-1} K^{-1} at 500 K. The

two sets of thermal conductivity data obtained from the two different samples of ''$Tl_{4.05}Ag_{18}Te_{11}$'' correspond with each other very well.

For comparison, these values are almost ten times lower than the thermal conductivity of $TlBiTe_2$,[26] 17 times lower than in $Mg_2Si_{0.325}Sn_{0.645}Bi_{0.03}$ (κ =3W m^{-1} K^{-1} at 500 K),[14] and nine times lower than in $Bi_2Te_{2.79}Se_{0.21}$ (1.6 W m^{-1} K^{-1} at 500 K).[150] The comparison of total thermal conductivity between ''$Tl_{4.05}Ag_{18}Te_{11}$'' with five other state-of-the-art thermoelectric materials is presented in Figure 6-9, demonstrating the thermal conductivity of ''$Tl_{4.05}Ag_{18}Te_{11}$'' is extremely low. The range of thermal conductivity of bulk nanostructured Bi_2Te_3,[159] $Pb_{0.98}Tl_{0.02}Te$,[119] BiSbTe,[160] $Cu_{1.98}Ag_{0.02}Te$,[58] and $Ag_{1-x}Pb_{18}SbTe_{20}$[161] is approximately 0.4–2.2 W m^{-1} K^{-1}, and their maximum *zT* values all exceed unity.

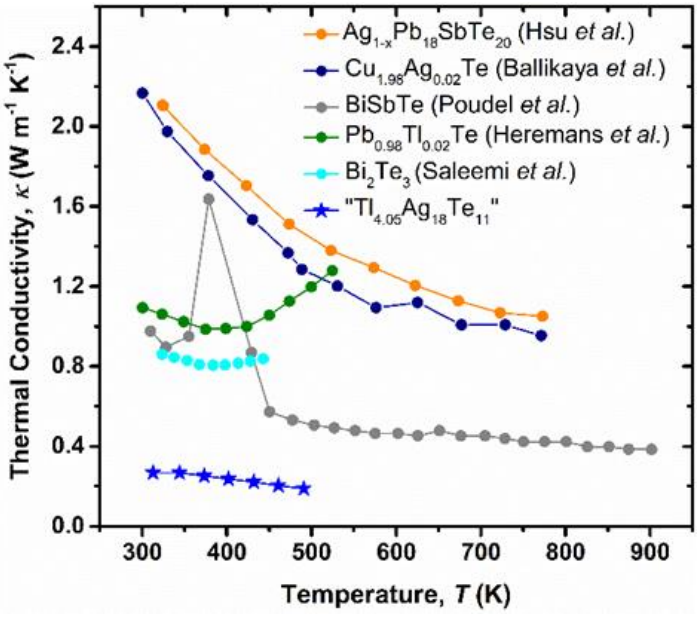

Figure 6-9: Thermal conductivity comparison with other state-of-the-art thermoelectric materials.

The Lorenz number L_0 was calculated from the measured Seebeck coefficient values based on the single Kane band model.[162] Due to the small electrical conductivity, the electrical thermal conductivity is only a minor contribution (its maximum value reaches 0.008 W m^{-1} K^{-1}at

430 K), and the lattice thermal conductivity is about 0.26 W m^{-1} K^{-1} at 320 K and 0.18 W m^{-1} K^{-1} at 500 K.

This ultralow thermal conductivity correlates nicely with the low Debye temperature of ϑ_D = 98 K obtained from of fit of the specific heat measurement. For comparison, PbTe has a Debye temperature of 177 K, and the binary thallium tellurides Tl_2Te, Tl_5Te_3, TlTe, and Tl_2Te_3 all comparable values between 107 K and 124 K.[27] The Debye temperature is directly proportional to the speed of sound:

$$\vartheta_D = \frac{\hbar}{k_B}(6\pi^2 n_a)^{1/3} v_S$$

Therein, $\hbar$ is the reduced Planck constant, k_B the Boltzmann constant, n_a the number density of atoms {number of atoms/cell/ (unit cell volume)}, and v_S the arithmetic average of the speed of sound. v_S in turn is proportional to the minimum thermal conductivity of both Clarke[16] and Cahill[17], recently compared to the ''diffuson thermal conductivity'' by Snyder's group[18]:

$$\text{Cahill: } \kappa_{glass} = 1.21 n^{2/3} k_B v_S$$

$$\text{Clarke: } \kappa_{min} = 0.93 n^{2/3} k_B v_S$$

$$\text{Snyder: } \kappa_{diff} = 0.76\, n^{2/3} k_B v_S$$

To derive the equation for κ_{diff}, thermal transport was based on diffusons instead of on phonons as used for κ_{glass}. This results in lower values for all materials, and may well correspond to the lowest possible thermal conductivity. Using v_S = 1385 m s^{-1} as calculated from ϑ_D = 98 K, we obtain κ_{glass} = 0.27 W m^{-1} K^{-1}, κ_{min} = 0.21 W m^{-1} K^{-1}, and κ_{diff} = 0.17 W m^{-1} K^{-1}. These numbers show that ''$Tl_{4.05}Ag_{18}Te_{11}$'' exhibits a thermal conductivity below the so-called glass limit according to Cahill, but not below the diffuson limit.

This extraordinary low thermal conductivity is likely caused by Tl disorders, heavy composing elements, and the large unit cell, which all contribute to reducing the mean free path length of the phonons travelling though the lattice. The disorder effect to lower thermal conductivity was thoroughly discussed in many previously published articles, such as for $Tl_2Ag_{12}Te_{7+\delta}$,[142] Cu_2Se,[163] and $Ba_3Cu_{16-x}(S,Te)_{11}$.[164] The ''cage rattling'' mechanism, where Tl3 atoms exhibit concerted rattling in a cage of Te atoms, is known to be important as well. Best known examples of this phenomenon are the filled skutterudites[165–167] and clathrates.[4,74,75,168] This concerted rattling phenomenon was also observed in $CsAg_5Te_3$, which owns an ultralow lattice thermal conductivity of 0.14 W m^{-1} K^{-1} at 727 K, and a Debye temperature of 118 K.[63] Furthermore, heavy elements tend to vibrate with a smaller amplitude because of the inertial resistance provided by the heavy nucleus, and thus cause a lower phonon transfer effect to the neighboring atoms. The principles of how larger unit cells and more complex crystal structures lower the lattice thermal conductivity were reviewed in 2010.[169]

The figure-of-merit curves of the samples are plotted in Figure 6-8d. The stoichiometric $Tl_4Ag_{18}Te_{11}$ sample achieves a maximum *zT* value of 0.13 at 470 K; whereas the *zT* of ''$Tl_{4.05}Ag_{18}Te_{11}$'' is twice as large, reaching a maximum of 0.26 at 465 K. The highest *zT* of ''$Tl_{4.05}Ag_{18}Te_{11}$'' is higher than the maximum *zT* of $TlBiTe_2$ which was achieved at 760 K with a value of 0.15.[26] However, it is still low in comparison to $Mg_2Si_{0.325}Sn_{0.645}Bi_{0.03}$, whose maximum *zT* is 1.35 at 773 K,[14] and $Bi_2Te_{2.79}Se_{0.21}$ whose maximum *zT* is 0.9 at 430 K.[150] For the two ''$Tl_4Ag_{18}Te_{10.95}$'' samples, the one with higher electrical conductivity exhibits the higher *zT* of 0.24 between 400 K and 425 K. These relatively low *zT* values could likely be significantly improved if the carrier concentration could be optimized via doping with heteroelements.

6.4 Conclusions

Thallium chalcogenides are known to rarely perform as *n*-type semiconductors; however, we found that $Tl_4Ag_{18}Te_{11}$ is an *n*-type material. The thermal behaviour of $Tl_4Ag_{18}Te_{11}$ was investigated by DSC, illustrating its incongruent melting at 723 K. The samples prepared and investigated are homogenous, and the physical properties of the samples are reproducible. All the samples have negative Seebeck coefficient values throughout the temperature range of 300–500 K, indicating that the majority of charge carriers are electrons. ''$Tl_{4.05}Ag_{18}Te_{11}$'' has the lowest thermal conductivity of 0.19 W m^{-1} K^{-1} at 500 K, which is extraordinary low compared to other thermoelectric materials. This is mainly a consequence of the disordered heavy Tl atoms filling the cuboctahedral cages and the complex crystal structure built by heavy elements.

The highest dimensionless figure-of-merit, *zT*, is about 0.26 obtained by the sample with the nominal formula of ''$Tl_{4.05}Ag_{18}Te_{11}$'' at 475 K, which is twice as high as the maximum *zT* of $Tl_4Ag_{18}Te_{11}$. Doping with other elements in order to optimize the thermoelectric properties, which are at this moment negatively affected by the low electrical conductivity, will be performed in the near future. Overall, $Tl_4Ag_{18}Te_{11}$ based materials will provide a promising *n*-type thermoelectric material, if their carrier concentrations can be enhanced.

Chapter 7: Summary and Outlook

In this thesis, the thermoelectric properties and syntheses of one thallium selenide and three thallium tellurides have been successfully investigated. The relationship between the complex structures and the ultralow thermal conductivity was further studied.

In Chapter 3, a new Tl-Ag-Se phase was discovered and the crystal structure was solved as a commensurate superstructure, which is a √3 × √3 × 1 super cell of the $Zr_2Fe_{12}P_7$ type. This material is bestowed with an ultralow thermal conductivity, but due to the low electrical conductivity, this material needs to be further doped in order to enhance the TE performance. This material has been confirmed as a *p*-type material below 380 K. The phase transition at about 410 K needs more investigations.

In Chapter 4, the incommensurate misfit structure of $Tl_2Ag_{12}Te_{7+\delta}$ was successfully determined, resolving the problematic original crystal structure with impossibly short Te-Te bond distances. $Tl_2Ag_{12}Te_{7+\delta}$ is also considered to be the best performing thermoelectric material with a misfit structure to date due to its extraordinarily low thermal conductivity (0.25 W m^{-1} K^{-1} and a high figure-of-merit of up to 1.1 at 525 K). However, since $Tl_2Ag_{12}Te_{7+\delta}$ is an intrinsic semiconductor, further improvements can probably be achieved by optimizing its carrier concentration through doping.

In Chapter 5, the anisotropic transport properties of TlSbTe2 were examined and compared to those of Bi_2Te_3. Although $TlSbTe_2$ still crystallizes in a layered structure, the covalent interactions between the layers diminish the anisotropy. The figure of merit of $TlSbTe_2$ was

overall improved by about 39% by optimizing the sintering process and 2% atomic Yb-doping (zT = 0.85 at 620 K).

In Chapter 6, one rare *n*-type thallium silver telluride, $Tl_4Ag_{18}Te_{11}$, with an extremely low thermal conductivity of 0.19 W m^{-1} K^{-1} was also studied. This material adopts a rattling crystal structure, which is considered to be the main reason for the low thermal conductivity. Through improving the conductivity of the sample by adding excess Tl into the compound, its zT doubled, indicating that slight improvements to the conductivity of samples with ultralow thermal conductivity can significantly improve the TE figure of merit.

Our studies spark the possibility of utilizing materials with misfit structures for potential TE applications. Further studies can be attempted in the way of designing more misfit structures with more economically and environmentally friendly elements.

References

(1) Le Roy, J.; Moreau, J. M.; Brun, G.; Liautard, B. A New Phase in the TlAgTe System: Crystal Structure of Tl4Ag24-XTe15-Y. *J. Alloys Compd.* **1992**, *186* (2), 249–254.

(2) He, J.; Tritt, T. M. Advances in Thermoelectric Materials Research: Looking Back and Moving Forward. *Science (80-.).* **2017**, *357*, 1369/1-1369/9.

(3) Shi, Y.; Sturm, C.; Kleinke, H. Chalcogenides as Thermoelectric Materials. *J. Solid State Chem.* **2019**, *270*, 273–279.

(4) Kleinke, H. New Bulk Materials for Thermoelectric Power Generation: Clathrates and Complex Antimonides. *Chem. Mater.* **2010**, *22* (3), 604–611.

(5) Snyder, G. J.; Toberer, E. S. Complex Thermoelectric Materials. *Nat. Mater.* **2008**, *7* (2), 105–114.

(6) Welch, R.; Limonadi, D.; Manning, R. Systems Engineering the Curiosity Rover: A Retrospective. In *Proceedings of 2013 8th International Conference on System of Systems Engineering: SoSE in Cloud Computing and Emerging Information Technology Applications, SoSE 2013*; 2013.

(7) Wang, Q.; Liu, J. A Chang'e-4 Mission Concept and Vision of Future Chinese Lunar Exploration Activities. *Acta Astronaut.* **2016**, *127*, 678–683.

(8) Yan, J.; Liao, X.; Yan, D.; Chen, Y. Review of Micro Thermoelectric Generator. *J. Microelectromechanical Syst.* **2018**, *27* (1), 1–18.

(9) Goldsmid, H. J. *The Physics of Thermoelectric Energy Conversion*; 2017.

(10) Chester, G. V.; Thellung, A. The Law of Wiedemann and Franz. *Proc. Phys. Soc.* **1961**, *77*, 1005.

(11) Lee, J. S.; Park, H. Carnot Efficiency Is Reachable in an Irreversible Process. *Sci. Rep.* **2017**, *10725*, 10664/1-9.

(12) Sturm, C.; Jafarzadeh, P.; Kleinke, H. Thermoelectric Nanomaterials. In *Comprehensive Nanoscience and Nanotechnology*; 2019.

(13) Jafarzadeh, P.; Rodrigues, M. R.; Shi, Y.; Assoud, A.; Zou, T.; Kycia, J. B.; Kleinke, H. Effect of Mixed Occupancies on the Thermoelectric Properties of BaCu6-: X Se1- y Te6+ y Polychalcogenides. *Dalt. Trans.* **2019**, *48*, 9357–9364.

(14) Macario, L. R.; Cheng, X.; Ramirez, D.; Mori, T.; Kleinke, H. Thermoelectric Properties of Bi-Doped Magnesium Silicide Stannides. *ACS Appl. Mater. Interfaces* **2018**, *10*, 40585–40591.

(15) Fu, C.; Xie, H.; Zhu, T. J.; Xie, J.; Zhao, X. B. Enhanced Phonon Scattering by Mass and Strain Field Fluctuations in Nb Substituted FeVSb Half-Heusler Thermoelectric Materials. *J. Appl. Phys.* **2012**, *112*, 124915/1-4.

(16) Clarke, D. R. Materials Selections Guidelines for Low Thermal Conductivity Thermal Barrier Coatings. *Surf. Coatings Technol.* **2003**, *163–164*, 67–74.

(17) Cahill, D. G.; Watson, S. K.; Pohl, R. O. Lower Limit to the Thermal Conductivity of Disordered Crystals. *Phys. Rev. B* **1992**, *46*, 6131–6140.

(18) Agne, M. T.; Hanus, R.; Snyder, G. J. Minimum Thermal Conductivity in the Context of: Diffuson - Mediated Thermal Transport. *Energy Environ. Sci.* **2018**, *11*, 609–616.

(19) van Smaalen, S. *Incommensurate Crystallography*; 2008.

(20) Sato, N.; Ouchi, H.; Takagiwa, Y.; Kimura, K. Glass-like Lattice Thermal Conductivity and Thermoelectric Properties of Incommensurate Chimney-Ladder Compound FeGeγ. *Chem. Mater.* **2016**, *28* (2), 529–533.

(21) Kikuchi, Y.; Miyazaki, Y.; Saito, Y.; Hayashi, K.; Yubuta, K.; Kajitani, T. Enhanced Thermoelectric Performance of a Chimney-Ladder (Mn 1-XCr x)Si γ (Γ∼ 1:7) Solid Solution. *Jpn. J. Appl. Phys.* **2012**, *51*, 085801-1/5.

(22) Wang, F.; Veremchuk, I.; Lidin, S. Tuning Crystal Structures and Thermoelectric Properties through Al Doping in ReSi1.75. *Eur. J. Inorg. Chem.* **2017**, *2017*, 47–55.

(23) Snyder, G. J.; Caillat, T.; Fleurial, J. P. Thermoelectric Properties of the Incommensurate Layered Semiconductor GexNbTe2. *J. Mater. Res.* **2000**, *15*, 2789–2793.

(24) Sharp, J. W.; Sales, B. C.; Mandrus, D. G.; Chakoumakos, B. C. Thermoelectric Properties of Tl2SnTe5 and Tl2GeTe5. *Appl. Phys. Lett.* **1999**.

(25) Guo, Q.; Assoud, A.; Kleinke, H. Improved Bulk Materials with Thermoelectric Figure-of-Merit Greater than 1: Tl10-XSnxTe6 and Tl10-XPbxTe6. *Adv. Energy Mater.* **2014**, *4* (14), 1400348/1-1400348/8.

(26) Kurosaki, K.; Kosuga, A.; Yamanaka, S. Thermoelectric Properties of TlBiTe2. *J. Alloys Compd.* **2003**, *351*, 279–282.

(27) Matsumoto, H.; Kurosaki, K.; Goto, K.; Muta, H.; Yamanaka, S. Thermoelectric Properties of Ag8Tl2Te5 and AgTl3Te2. In *International Conference on Thermoelectrics, ICT, Proceedings*; 2007; pp 94–98.

(28) Kurosaki, K.; Uneda, H.; Muta, H.; Yamanaka, S. Thermoelectric Properties of Thallium Antimony Telluride. *J. Alloys Compd.* **2004**, *376* (1–2), 43–48.

(29) Assoud, A.; Shi, Y.; Guo, Q.; Kleinke, H. Crystal and Electronic Structure of the New Quaternary Sulfides TlLnAg<inf>2</Inf>S<inf>3</Inf>(Ln = Nd, Sm and Gd). *J. Solid State Chem.* **2017**, *256*.

(30) Sankar, C. R.; Assoud, A.; Kleinke, H. New Layered-Type Quaternary Chalcogenides, Tl2PbMQ4 (M = Zr, Hf; Q = S, Se): Structure, Electronic Structure, and Electrical Transport Properties. *Inorg. Chem.* **2013**, *52*, 13869–13874.

(31) Aswathy, V. S.; Sankar, C. R.; Varma, M. R.; Assoud, A.; Bieringer, M.; Kleinke, H. Thermoelectric Properties and Thermal Stability of Layered Chalcogenides, TlScQ 2 , Q = Se, Te. *Dalt. Trans.* **2017**, *46*, 17053–17060.

(32) Harman, T. C.; Paris, B.; Miller, S. E.; Goering, H. L. Preparation and Some Physical Properties of Bi 2 Te 3, Sb 2 Te 3, and As 2 Te 3. *J. Phys. Chem. Solids* **1957**, *2* (3), 181–190.

(33) Hao, F.; Qiu, P.; Tang, Y.; Bai, S.; Xing, T.; Chu, H. S.; Zhang, Q.; Lu, P.; Zhang, T.; Ren, D.; Chen, J.; Shi, X.; Chen, L. High Efficiency Bi2Te3-Based Materials and Devices for Thermoelectric Power Generation between 100 and 300 °c. *Energy Environ. Sci.* **2016**, *9*, 3120–3127.

(34) Shen, J. J.; Zhu, T. J.; Zhao, X. B.; Zhang, S. N.; Yang, S. H.; Yin, Z. Z. Recrystallization Induced in Situ Nanostructures in Bulk Bismuth Antimony Tellurides: A Simple Top down Route and Improved Thermoelectric Properties. *Energy Environ. Sci.* **2010**, *3*, 1519–1523.

(35) Lv, H. Y.; Liu, H. J.; Shi, J.; Tang, X. F.; Uher, C. Optimized Thermoelectric Performance of Bi2Te3 Nanowires. *J. Mater. Chem. A* **2013**, *1*, 6831–6838.

(36) Venkatasubramanian, R.; Slivola, E.; Colpitts, T.; O'Quinn, B. Thin-Film Thermoelectric Devices

with High Room-Temperature Figures of Merit. *Nature* **2001**, *413* (6856), 597–602.

(37) Lalonde, A. D.; Pei, Y.; Wang, H.; Jeffrey Snyder, G. Lead Telluride Alloy Thermoelectrics. *Mater. Today* **2011**, *14*, 526–532.

(38) Gelbstein, Y.; Dashevsky, Z.; Dariel, M. P. High Performance N-Type PbTe-Based Materials for Thermoelectric Applications. *Phys. B* **2005**, *363*, 196–205.

(39) Pei, Y.; LaLonde, A.; Iwanaga, S.; Snyder, G. J. High Thermoelectric Figure of Merit in Heavy Hole Dominated PbTe. *Energy Environ. Sci.* **2011**, *4*, 2085–2089.

(40) Hsu, K.; Loo, S.; Guo, F.; Chen, W.; Dyck, J.; Uher, C.; Hogan, T.; Polychroniadis, E.; Kanatzidis, M. Cubic AgPbmSbTe2+m: Bulk Thermoelectric Materials with High Figure of Merit. *Science (80-.).* **2004**, *303*, 818–821.2

(41) Quarez, E.; Hsu, K. F.; Pcionek, R.; Frangis, N.; Polychroniadis, E. K.; Kanatzidis, M. G. Nanostructuring, Compositional Fluctuations, and Atomic Ordering in the Thermoelectric Materials AgPbmSbTe2+m. The Myth of Solid Solutions. *J. Am. Chem. Soc.* **2005**.

(42) Zhao, L. D.; Chang, C.; Tan, G.; Kanatzidis, M. G. SnSe: A Remarkable New Thermoelectric Material. *Energy Environ. Sci.* **2016**, *9*, 3044–3060.

(43) Das, D.; Malik, K.; Deb, A. K.; Dhara, S.; Bandyopadhyay, S.; Banerjee, A. Defect Induced Structural and Thermoelectric Properties of Sb2Te3 Alloy. *J. Appl. Phys.* **2015**, *118* (045102), 1–7.

(44) Du, B.; Li, H.; Xu, J.; Tang, X.; Uher, C. Enhanced Figure-of-Merit in Se-Doped p-Type AgSbTe2 Thermoelectric Compound. *Chem. Mater.* **2010**, *22* (19), 5521–5527.

(45) Shi, X.; Chen, Z. G.; Liu, W.; Yang, L.; Hong, M.; Moshwan, R.; Huang, L.; Zou, J. Achieving High Figure of Merit in P-Type Polycrystalline Sn0.98Se via Self-Doping and Anisotropy-Strengthening. *Energy Storage Mater.* **2018**, *10*, 130–138.

(46) Larson, A. C.; Von Dreele, R. B. General Structure Analysis System (GSAS); Report LAUR 86-748; Los Alamos National Laboratory: Los Alamos, NM, 2000. *There is no Corresp. Rec. this Ref.* **2000**, *241*, 114–119.

(47) He, Y.; Day, T.; Zhang, T.; Liu, H.; Shi, X.; Chen, L.; Snyder, G. J. High Thermoelectric Performance in Non-Toxic Earth-Abundant Copper Sulfide. *Adv. Mater.* **2014**.

(48) Zhao, L.; Wang, X.; Fei, F. Y.; Wang, J.; Cheng, Z.; Dou, S.; Wang, J.; Snyder, G. J. High Thermoelectric and Mechanical Performance in Highly Dense Cu2-XS Bulks Prepared by a Melt-Solidification Technique. *J. Mater. Chem. A* **2015**, *3* (18), 9432–9437.

(49) Zhao, K.; Blichfeld, A. B.; Chen, H.; Song, Q.; Zhang, T.; Zhu, C.; Ren, D.; Hanus, R.; Qiu, P.; Iversen, B. B.; Xu, F.; Snyder, G. J.; Shi, X.; Chen, L. Enhanced Thermoelectric Performance through Tuning Bonding Energy in Cu 2 Se 1-x S x Liquid-like Materials. *Chem. Mater.* **2017**, *3*, 9432–9437.

(50) Zhao, K.; Blichfeld, A. B.; Eikeland, E.; Qiu, P.; Ren, D.; Iversen, B. B.; Shi, X.; Chen, L. Extremely Low Thermal Conductivity and High Thermoelectric Performance in Liquid-like Cu 2 Se 1-: X S x Polymorphic Materials. *J. Mater. Chem. A* **2017**, *5*, 18148–18156.

(51) Zhao, K.; Qiu, P.; Song, Q.; Blichfeld, A. B.; Eikeland, E.; Ren, D.; Ge, B.; Iversen, B. B.; Shi, X.; Chen, L. Ultrahigh Thermoelectric Performance in Cu 2−y Se 0.5 S 0.5 Liquid-like Materials. *Mater. Today Phys.* **2017**, *1*, 14–23.

(52) He, Y.; Lu, P.; Shi, X.; Xu, F.; Zhang, T.; Snyder, G. J.; Uher, C.; Chen, L. Ultrahigh Thermoelectric Performance in Mosaic Crystals. *Adv. Mater.* **2015**.

(53) Liu, H.; Shi, X.; Xu, F.; Zhang, L.; Zhang, W.; Chen, L.; Li, Q.; Uher, C.; Day, T.; Snyder Jeffrey, G. Copper Ion Liquid-like Thermoelectrics. *Nat. Mater.* **2012**, *11*, 422–425.

(54) Yu, B.; Liu, W.; Chen, S.; Wang, H.; Wang, H.; Chen, G.; Ren, Z. Thermoelectric Properties of Copper Selenide with Ordered Selenium Layer and Disordered Copper Layer. *Nano Energy* **2012**.

(55) Su, X.; Fu, F.; Yan, Y.; Zheng, G.; Liang, T.; Zhang, Q.; Cheng, X.; Yang, D.; Chi, H.; Tang, X.; Zhang, Q.; Uher, C. Self-Propagating High-Temperature Synthesis for Compound Thermoelectrics and New Criterion for Combustion Processing. *Nat. Commun.* **2014**, *5*, 4908/1--7.

(56) Zhao, L. L.; Wang, X. L.; Wang, J. Y.; Cheng, Z. X.; Dou, S. X.; Wang, J.; Liu, L. Q. Superior Intrinsic Thermoelectric Performance with ZT of 1.8 in Single-Crystal and Melt-Quenched Highly Dense Cu2-XSe Bulks. *Sci. Rep.* **2015**, *5* (7671), 1–6.

(57) Gahtori, B.; Bathula, S.; Tyagi, K.; Jayasimhadri, M.; Srivastava, A. K.; Singh, S.; Budhani, R. C.; Dhar, A. Giant Enhancement in Thermoelectric Performance of Copper Selenide by Incorporation of Different Nanoscale Dimensional Defect Features. *Nano Energy* **2015**, *13*, 36–46.

(58) Ballikaya, S.; Chi, H.; Salvador, J. R.; Uher, C. Thermoelectric Properties of Ag-Doped Cu2Se and Cu2Te. *J. Mater. Chem. A* **2013**, *1*, 12478–12484.

(59) He, Y.; Zhang, T.; Shi, X.; Wei, S. H.; Chen, L. High Thermoelectric Performance in Copper Telluride. *NPG Asia Mater.* **2015**, *7* (e210), 1–7.

(60) Wölfing, B.; Kloc, C.; Teubner, J.; Bucher, E. High Performance Thermoelectric Tl9BiTe6 with an Extremely Low Thermal Conductivity. *Phys. Rev. Lett.* **2001**, *86* (19), 4350–4353.

(61) Guo, Q.; Chan, M.; Kuropatwa, B. A.; Kleinke, H. Enhanced Thermoelectric Properties of Variants of Tl9SbTe6 and Tl9BiTe6. *Chem. Mater.* **2013**, *25* (20), 4097–4104.

(62) Kurosaki, K.; Kosuga, A.; Muta, H.; Uno, M.; Yamanaka, S. Ag9TlTe5: A High-Performance Thermoelectric Bulk Material with Extremely Low Thermal Conductivity. *Appl. Phys. Lett.* **2005**, *87* (6), 061919/1-06919/3.

(63) Lin, H.; Tan, G.; Shen, J. N.; Hao, S.; Wu, L. M.; Calta, N.; Malliakas, C.; Wang, S.; Uher, C.; Wolverton, C.; Kanatzidis, M. G. Concerted Rattling in CsAg5Te3Leading to Ultralow Thermal Conductivity and High Thermoelectric Performance. *Angew. Chemie - Int. Ed.* **2016**, *55*, 11431–11436.

(64) Shen, X.; Yang, C. C.; Liu, Y.; Wang, G.; Tan, H.; Tung, Y. H.; Wang, G.; Lu, X.; He, J.; Zhou, X. High-Temperature Structural and Thermoelectric Study of Argyrodite Ag 8 GeSe 6. *ACS Appl. Mater. Interfaces* **2019**, *11*, 2168–2176.

(65) Charoenphakdee, A.; Kurosaki, K.; Muta, H.; Uno, M.; Yamanaka, S. Reinvestigation of the Thermoelectric Properties of Ag8GeTe 6. *Phys. Status Solidi - Rapid Res. Lett.* **2008**, *2*, 65–67.

(66) Li, W.; Lin, S.; Ge, B.; Yang, J.; Zhang, W.; Pei, Y. Low Sound Velocity Contributing to the High Thermoelectric Performance of Ag8SnSe6. *Adv. Sci.* **2016**, *3*, 1600196/1-7.

(67) Charoenphakdee, A.; Kurosaki, K.; Muta, H.; Uno, M.; Yamanaka, S. Ag8SiTe6: A New Thermoelectric Material with Low Thermal Conductivity. *Jpn. J. Appl. Phys.* **2009**, *48*, 011603/1-3.

(68) Heep, B. K.; Weldert, K. S.; Krysiak, Y.; Day, T. W.; Zeier, W. G.; Kolb, U.; Snyder, G. J.; Tremel, W. High Electron Mobility and Disorder Induced by Silver Ion Migration Lead to Good Thermoelectric Performance in the Argyrodite Ag 8 SiSe 6. *Chem. Mater.* **2017**, *29*, 4833–4839.

(69) Kurosaki, K.; Goto, K.; Muta, H.; Yamanaka, S. Enhancement of Thermoelectric Figure of Merit of

AgTlTe by Tuning the Carrier Concentration. *J. Appl. Phys.* **2007**, *102* (2), 023707/1-023707/5.

(70) Moreau, J. M.; Allemand, J.; Brun, G.; Liautard, B. A New Phase in the TlAgTe System: Crystal Structure of Tl4Ag18Te11. *J. Alloys Compd.* **1992**, *178* (1–2), 85–90.

(71) Eilertsen, J.; Rouvimov, S.; Subramanian, M. A. Rattler-Seeded InSb Nanoinclusions from Metastable Indium-Filled In 0.1Co 4Sb 12 Skutterudites for High-Performance Thermoelectrics. *Acta Mater.* **2012**, *60*, 2178–2185.

(72) Lee, C. H.; Hase, I.; Sugawara, H.; Yoshizawa, H.; Sato, H. Low-Lying Optical Phonon Modes in the Filled Skutterudite CeRu 4Sb12. *J. Phys. Soc. Japan* **2006**, *75*, 123602/1-123602/4.

(73) Slack, G. A. Design Concepts for Improved Thermoelectric Materials. *Mat. Res. Soc. Symp. Proc.* **1997**, *478* (Thermoelectric Materials--New Directions and Approaches), 47–54.

(74) Christensen, M.; Johnsen, S.; Iversen, B. B. Thermoelectric Clathrates of Type I. *Dalt. Trans.* **2010**, *39*, 978–992.

(75) Takabatake, T.; Suekuni, K.; Nakayama, T.; Kaneshita, E. Phonon-Glass Electron-Crystal Thermoelectric Clathrates: Experiments and Theory. *Rev. Mod. Phys.* **2014**, *86*, 669–716.

(76) Kurosaki, K.; Uneda, H.; Muta, H.; Yamanaka, S. Thermoelectric Properties of Thallium Antimony Telluride. *J. Alloy. Compd.* **2004**, *376* (1–2), 43–48.

(77) Toby, B. H. General Structure Analysis System - GSAS / EXPGUI, A Graphical User Interface for GSAS. *J. Appl. Crystallogr.* **2001**, *34*, 210.

(78) Sheldrick, G. M. A Short History of SHELX. *Acta Crystallogr. A* **2008**, *64*, 112–122.

(79) Petrícek, V.; Dušek, M.; Palatinus, L. Crystallographic Computing System JANA2006: General Features. *Zeitschrift fur Kristallographie*. 2014, pp 345–352.

(80) Perdew, J. P.; Burke, K.; Ernzerhof, M. Generalized Gradient Approximation Made Simple. *Phys. Rev. Lett.* **1996**, *77* (18), 3865–3868.

(81) Koller, D.; Tran, F.; Blaha, P. Improving the Modified Becke-Johnson Exchange Potential. *Phys. Rev. B - Condens. Matter Mater. Phys.* **2012**, *85*, 155109/1-8.

(82) Blaha, P.; Schwarz, K.; Madsen, G. K. H.; Kvasnicka, D.; Luitz, J. *WIEN2k, An Augmented Plane Wave + Local Orbitals Program for Calculating Crystal Properties*; Schwarz, K., Ed.; Techn. Universität Wien, Austria, 2001.

(83) Wood, P. T.; Pennington, W. T.; Kolis, J. W. Synthesis of Novel Solid-State Compounds in Supercritical Solvents: Preparation and Structure of K2Ag12Se7 in Supercritical Ethylenediamine. *J. Am. Chem. Soc.* **1992**, *114* (23), 9233–9235.

(84) Pertlik, F. Preparation and Crystal Structure of K2Ag12Te7. *Monatsh. Chem.* **2001**, *132* (12), 1509–1513.

(85) Ganglberger, E. Die Kristallstruktur von Fe2Zr2P7. *Monatsh. Chem.* **1968**, *99*, 557–568.

(86) Emirdag, M.; Schimek, G. L.; Pennington, W. T.; Kolis, J. W. Synthesis of Two New Metallic Alkali Metal Silver Selenides, K2Ag12Se7.11and RbAg5Se3, from Supercritical Ethylenediamine. *J. Solid State Chem.* **1999**, *144* (2), 287–296.

(87) Spek, A. L. Structure Validation in Chemical Crystallography. *Acta Crystallogr. D* **2009**, *65*, 148–155.

(88) Assoud, A.; Guo, Q.; Sankar, C. R.; Kleinke, H. Crystal Structure, Electronic Structure and Physical Properties of the New Quaternary Chalcogenides Tl2NdAg3Se4 and Tl2NdAg3Te4. *Inorg. Chem. Front.* **2017**, *4* (2), 315–323.

(89) Babanly, M. B.; Kuliev, A. A. Phase Equilibria and Thermodynamic Properties of the Ag-Se-Tl System. *Russ. J. Inorg. Chem.* **1982**, *27* (9), 1336–1339.

(90) Kurosaki, K.; Kosuga, A.; Muta, H.; Uno, M.; Yamanaka, S. Ag9TlTe5: A High-Performance Thermoelectric Bulk Material with Extremely Low Thermal Conductivity. *Appl. Phys. Lett.* **2005**, *87*, 061919/1-3.

(91) Palatinus, L.; Chapuis, G. SUPERFLIP - A Computer Program for the Solution of Crystal Structures by Charge Flipping in Arbitrary Dimensions. *J. Appl. Crystallogr.* **2007**, *40* (4), 786–790.

(92) Assoud, A.; Cui, Y.; Thomas, S.; Sutherland, B.; Kleinke, H. Structure and Physical Properties of the New Telluride BaAg2Te2 and Its Quaternary Variants BaCudAg2–DTe2. *J. Solid State Chem.* **2008**, *181*, 2024–2030.

(93) Nilges, T.; Lange, S.; Bawohl, M.; Deckwart, J. M.; Janssen, M.; Wiemhöfer, H. D.; Decourt, R.; Chevalier, B.; Vannahme, J.; Eckert, H.; Weihrich, R. Reversible Switching between P- and n-Type Conduction in the Semiconductor Ag10Te4Br3. *Nat. Mater.* **2009**, *8* (2), 101–108.

(94) Lange, S.; Nilges, T. Ag10Te4Br3: A New Silver(I) (Poly)Chalcogenide Halide Solid Electrolyte. *Chem. Mater.* **2006**, *18*, 2538–2544.

(95) Mayasree, O.; Sankar, C. R.; Cui, Y.; Assoud, A.; Kleinke, H. Synthesis, Structure and Thermoelectric Properties of Barium Copper Polychalcogenides with Chalcogen-Centered Cu Clusters and Te22– Dumbbells. *Eur. J. Inorg. Chem.* **2011**, 4037–4042.

(96) Oudah, M.; Kleinke, K. M.; Kleinke, H. Thermoelectric Properties of the Quaternary Chalcogenides BaCu5.9STe6 and BaCu5.9SeTe6. *Inorg. Chem.* **2015**, *54*, 845–849.

(97) Assoud, A.; Xu, J.; Kleinke, H. Structures and Physical Properties of New Semiconducting Polyselenides Ba2CudAg4-DSe5 with Unprecedented Linear Se34- Units. *Inorg. Chem.* **2007**, *46*, 9906–9911.

(98) Cordier, G.; Schäfer, H.; Stelter, M. Darstellung Und Struktur Der Verbindung Ca14AlSb11. *Z. Anorg. Allg. Chem.* **1984**, *519*, 183–188.

(99) Brown, S. R.; Kauzlarich, S. M.; Gascoin, F.; Snyder, G. J. Yb 14 MnSb 11 : New High Efficiency Thermoelectric Material for Power Generation. *Chem. Mater.* **2006**, *18* (7), 1873–1877.

(100) Bux, S. K.; Zevalkink, A.; Janka, O.; Uhl, D.; Kauzlarich, S.; Snyder, J. G.; Fleurial, J.-P. Glass-like Lattice Thermal Conductivity and High Thermoelectric Efficiency in Yb9Mn4.2Sb9. *J. Mater. Chem. A* **2014**, *2* (1), 215–220.

(101) Grebenkemper, J. H.; Hu, Y.; Barrett, D.; Gogna, P.; Huang, C.-K.; Bux, S. K.; Kauzlarich, S. M. High Temperature Thermoelectric Properties of Yb14MnSb11 Prepared from Reaction of MnSb with the Elements. *Chem. Mater.* **2015**, *27* (16), 5791–5798.

(102) Caillat, T.; Fleurial, J.-P.; Borshchevsky, A. Preparation and Thermoelectric Properties of Semiconducting Zn4Sb3. *J. Phys. Chem. Solids* **1997**, *58* (7), 1119–1125.

(103) Mozharivskyj, Y.; Janssen, Y.; Harringa, J. L.; Kracher, A.; Tsokol, A. O.; Miller, G. J. Zn13Sb10: A Structural and Landau Theoretical Analysis of Its Phase Transitions. *Chem. Mater.* **2006**, *18*, 822–831.

(104) Snyder, G. J.; Christensen, M.; Nishibori, E.; Caillat, T.; Iversen, B. B. Disordered Zinc in Zn4Sb3 with Phonon-Glass and Electron-Crystal Thermoelectric Properties. *Nat. Mater.* **2004**, *3*, 458–463.

(105) Assoud, A.; Soheilnia, N.; Kleinke, H. Band Gap Tuning in New Strontium Seleno-Stannates. *Chem. Mater.* **2004**, *16*, 2215–2221.

(106) Xu, J.; Kleinke, H. Unusual Sb–Sb Bonding in High Temperature Thermoelectric Materials. *J. Comput. Chem.* **2008**, *29*, 2134–2143.

(107) Kleinke, H. Zr1-XTixSb: A Novel Antimonide on the Quasibinary Section ZrSb-TiSb with a Complex Crystal Structure Exhibiting Linear Sb Chains and Fragments of the TiSb Structure. *J. Am. Chem. Soc.* **2000**, *122* (5), 853–860.

(108) Papoian, G. A.; Hoffmann, R. Hypervalent Bonding in One, Two, and Three Dimensions: Extending the Zintl-Klemm Concept to Nonclassical Electron-Rich Networks. *Angew. Chem. Int. Ed.* **2000**, *39*, 2408–2448.

(109) Gawel, W.; Zaleska, E.; Terpilowski, J. Phase Equilibria in the Tl2Te-Ag2Te System. *J. Therm. Anal.* **1987**, *32* (1), 227–235.

(110) da Silva, L. W.; Kaviany, M. Micro-Thermoelectric Cooler: Interfacial Effects on Thermal and Electrical Transport. *Int. J. Heat Mass Transf.* **2004**, *47*, 2417–2435.

(111) Kanatzidis, M. G. Nanostructured Thermoelectrics. The New Paradigm? *Chem. Mater.* **2010**, *22* (3), 648–659.

(112) Wan, C.; Wang, Y.; Wang, N.; Koumoto, K. Low-Thermal-Conductivity (MS)1+x(TiS2)2 (M = Pb, Bi, Sn) Misfit Layer Compounds for Bulk Thermoelectric Materials. *Materials (Basel).* **2010**, *3* (12), 2606–2617.

(113) Li, L.; Yan, X.-J.; Dong, S.-T.; Lv, Y.-Y.; Li, X.; Yao, S.-H.; Chen, Y.-B.; Zhang, S.-T.; Zhou, J.; Lu, H.; Lu, M.-H.; Chen, Y.-F. Ultra-Low Thermal Conductivities along c-Axis of Naturally Misfit Layered Bi2 [AE]2Co2Oy (AE = Ca, Ca0.5Sr0.5, Sr, Ba) Single Crystals. *Cit. Appl. Phys. Lett* **2017**, *111*, 033902/1-4.

(114) Bhattacharya, S.; Hermann, R. P.; Keppens, V.; Tritt, T. M.; Snyder, G. J. Effect of Disorder on the Thermal Transport and Elastic Properties in Thermoelectric Zn4 Sb3. *Phys. Rev. B - Condens. Matter Mater. Phys.* **2006**, *74*, 134108/1-5.

(115) Schweika, W.; Hermann, R. P.; Prager, M.; Perßon, J.; Keppens, V. Dumbbell Rattling in Thermoelectric Zinc Antimony. *Phys. Rev. Lett.* **2007**, *99* (12).

(116) Wu, F.; Song, H.; Gao, F.; Shi, W.; Jia, J.; Hu, X. Effects of Different Morphologies of Bi2Te3 Nanopowders on Thermoelectric Properties. *J. Electron. Mater.* **2013**, *42* (6), 1140–1145.

(117) Guo, Q.; Chan, M.; Kuropatwa, B. A.; Kleinke, H. Enhanced Thermoelectric Properties of Variants of Tl9SbTe6 and Tl9BiTe6. *Chem. Mater.* **2013**, *25*, 4097–4104.

(118) Poudeu, P. F. P.; D'Angelo, J.; Downey, A. D.; Short, J. L.; Hogan, T. P.; Kanatzidis, M. G. High Thermoelectric Figure of Merit and Nanostructuring in Bulk P-Type Na1-XPbmSbyTem+213. *Angew. Chem. Int. Ed.* **2006**, *45*, 3835–3839.

(119) Heremans, J. P.; Jovovic, V.; Toberer, E. S.; Saramat, A.; Kurosaki, K.; Charoenphakdee, A.; Yamanaka, S.; Snyder, G. J. Enhancement of Thermoelectric Efficiency in PbTe by Distortion of the Electronic Density of States. *Science (80-.).* **2008**, *321*, 554–557.

(120) Shi, X.; Yang, J.; Salvador, J. R.; Chi, M.; Cho, J. Y.; Wang, H.; Bai, S.; Yang, J.; Zhang, W.; Chen, L.

Multiple-Filled Skutterudites: High Thermoelectric Figure of Merit through Separately Optimizing Electrical and Thermal Transports. *J. Am. Chem. Soc.* **2011**, *133*, 7837–7846.

(121) Pei, Y.; Shi, X.; LaLonde, A.; Wang, H.; Chen, L.; Snyder, G. J. Convergence of Electronic Bands for High Performance Bulk Thermoelectrics. *Nature* **2011**, *473*, 66–69.

(122) Toberer, E. S.; Cox, C. A.; Brown, S. R.; Ikeda, T.; May, A. F.; Kauzlarich, S. M.; Snyder, G. J. Traversing the Metal-Insulator Transition in a Zintl Phase: Rational Enhancement of Thermoelectric Efficiency in Yb14Mn1-XAlxSb11. *Adv. Funct. Mater.* **2008**, *18*, 2795–2800.

(123) Hockings, E. F.; White, J. G. The Crystal Structures of TlSbTe2 and TlBiTe2. *Acta Crystallogr.* **1961**, *14* (3), 328.

(124) Hoang, K.; Mahanti, S. D. Atomic and Electronic Structures of Thallium-Based III-V-VI2 Ternary Chalcogenides: Ab Initio Calculations. *Phys. Rev. B - Condens. Matter Mater. Phys.* **2008**, *77* (20), 205107.

(125) Stordeur, M.; Heiliger, W. Anisotropy of the Thermopower of P-Sb2Te3. *Phys. status solidi* **1976**, *78* (2), K103–K106.

(126) Nagao, J.; Ferhat, M.; Hatta, E.; Mukasa, K. Anisotropic Factor of Electrical Conductivity in P-Bi2Te3 Crystals. *Phys. status solidi* **2000**, *219* (2), 347–349.

(127) Paraskevopoulos, K. M.; Hatzikraniotis, E.; Vinga, E. S.; Ozer, M.; Anagnostopoulos, A.; Polychroniadis, E. K. N-p Transformation in TlBi(1-x)SbxTe2 System. *J. Alloys Compd.* **2009**, *467* (1–2), 65–71.

(128) Yan, X.; Poudel, B.; Ma, Y.; Liu, W. S.; Joshi, G.; Wang, H.; Lan, Y.; Wang, D.; Chen, G.; Ren, Z. F. Experimental Studies on Anisotropic Thermoelectric Properties and Structures of N-Type Bi2Te2. 7Se0. 3. *Nano Lett.* **2010**, *10* (9), 3373–3378.

(129) Ohsugi, I. J.; Kojima, T.; Nishida, I. A. Orientation Analysis of the Anisotropic Galvanomagnetism of Sintered Bi2Te3. *J. Appl. Phys.* **1990**, *68* (11), 5692–5695.

(130) Le Bail, A.; Duroy, H.; Fourquet, J. L. Ab-Initio Structure Determination of LiSbWO6 by X-Ray Powder Diffraction. *Mater. Res. Bull.* **1988**, *23*, 447–452.

(131) Zhang, Z.; Sharma, P. A.; Lavernia, E. J.; Yang, N. Thermoelectric and Transport Properties of Nanostructured Bi 2Te3 by Spark Plasma Sintering. *J. Mater. Res.* **2011**, *26* (3), 475–484.

(132) Zhang, Y.; Jia, X.; Deng, L.; Guo, X.; Sun, H.; Sun, B.; Liu, B.; Ma, H. Evolution of Thermoelectric Properties and Anisotropic Features of Bi2Te3prepared by High Pressure and High Temperature. *J. Alloys Compd.* **2015**, *632*, 514–519.

(133) Su, T.; Jia, X.; Ma, H.; Yu, F.; Tian, Y.; Zuo, G.; Zheng, Y.; Jiang, Y.; Dong, D.; Deng, L.; Qin, B.; Zheng, S. Enhanced Thermoelectric Performance of AgSbTe2 Synthesized by High Pressure and High Temperature. *J. Appl. Phys.* **2009**, *105* (073713), 1–4.

(134) Du, B.; Li, H.; Xu, J.; Tang, X.; Uher, C. Enhanced Thermoelectric Performance and Novel Nanopores in AgSbTe 2 Prepared by Melt Spinning. *J. Solid State Chem.* **2011**, *184* (1), 109–114.

(135) Kuropatwa, B. A.; Assoud, A.; Kleinke, H. Effects of Cation Site Substitutions on the Thermoelectric Performance of Layered SnBi2Te4 Utilizing the Triel Elements Ga, In, and Tl. *Zeitschrift fur Anorg. und Allg. Chemie* **2013**, *639* (14), 2411–2420.

(136) Zhang, J.-M.; Ming, W.; Huang, Z.; Liu, G.-B.; Kou, X.; Fan, Y.; Wang, K. L.; Yao, Y. Stability, Electronic, and Magnetic Properties of the Magnetically Doped Topological Insulators Bi2Se3, ,

Bi2Te3, and Sb2Te3. *Phys. Rev. B* **2013**, *88* (23), 235131 1-8.

(137) Kim, J.-H.; Choi, J.-Y.; Bae, J.-M.; Kim, M.-Y.; Oh, T.-S. Thermoelectric Characteristics of N-Type Bi2Te3 and p-Type Sb2Te3 Thin Films Prepared by Co-Evaporation and Annealing for Thermopile Sensor Applications. *Mater. Trans.* **2013**, *54* (4), 618–625.

(138) Horák, J.; Čermák, K.; Koudelka, L. Energy Formation of Antisite Defects in Doped Sb2Te3 and Bi2Te3 Crystals. *J. Phys. Chem. Solids* **1986**, *47* (8), 805–809.

(139) Goldsmid, H. J.; Sharp, J. W. Estimation of the Thermal Band Gap of a Semiconductor from Seebeck Measurements. *J. Electron. Mater.* **1999**, *28* (7), 869–872.

(140) Xiong, D. B.; Okamoto, N. L.; Inui, H. Enhanced Thermoelectric Figure of Merit in P-Type Ag-Doped ZnSb Nanostructured with Ag3Sb. *Scr. Mater.* **2013**, *69* (5), 397–400.

(141) Beyer, H.; Nurnus, J.; Böttner, H.; Lambrecht, A.; Wagner, E.; Bauer, G. High Thermoelectric Figure of Merit ZT in PbTe and Bi2Te3-Based Superlattices by a Reduction of the Thermal Conductivity. *Phys. E Low-Dimensional Syst. Nanostructures* **2002**, *13* (2–4), 965–968.

(142) Shi, Y.; Assoud, A.; Ponou, S.; Lidin, S.; Kleinke, H. A New Material with a Composite Crystal Structure Causing Ultralow Thermal Conductivity and Outstanding Thermoelectric Properties: Tl2Ag12Te7+δ. *J. Am. Chem. Soc.* **2018**, *140* (27), 8578–8585.

(143) Kurosaki, K.; Yamanaka, S. Low-Thermal-Conductivity Group 13 Chalcogenides as High-Efficiency Thermoelectric Materials. *Phys. Status Solidi* **2013**, *210*, 82–88.

(144) McGuire, M. A.; Scheidemantel, T. J.; Badding, J. V.; DiSalvo, F. J. Tl 2AXTe 4 (A = Cd, Hg, Mn; X = Ge, Sn): Crystal Structure, Electronic Structure, and Thermoelectric Properties. *Chem. Mater.* **2005**, *17*, 6186–6191.

(145) Hu, L. P.; Liu, X. H.; Xie, H. H.; Shen, J. J.; Zhu, T. J.; Zhao, X. B. Improving Thermoelectric Properties of N-Type Bismuth-Telluride-Based Alloys by Deformation-Induced Lattice Defects and Texture Enhancement. *Acta Mater.* **2012**, *60* (11), 4431–4437.

(146) Yang, L.; Chen, Z. G.; Hong, M.; Wang, L.; Kong, D.; Huang, L.; Han, G.; Zou, Y.; Dargusch, M.; Zou, J. N-Type Bi-Doped PbTe Nanocubes with Enhanced Thermoelectric Performance. *Nano Energy* **2017**, *31*, 105–112.

(147) Lalonde, A. D.; Pei, Y.; Snyder, G. J. Reevaluation of PbTe1-XIx as High Performance n-Type Thermoelectric Material. *Energy Environ. Sci.* **2011**, *4*, 2090–2096.

(148) Matsubara, M.; Asahi, R. Optimization of Filler Elements in CoSb3-Based Skutterudites for High-Performance n-Type Thermoelectric Materials. *J. Electron. Mater.* **2016**, *45* (3), 1669–1678.

(149) Rogl, G.; Grytsiv, A.; Yubuta, K.; Puchegger, S.; Bauer, E.; Raju, C.; Mallik, R. C.; Rogl, P. In-Doped Multifilled n-Type Skutterudites with ZT = 1.8. *Acta Mater.* **2015**, *95*, 201–211.

(150) Hu, L.; Wu, H.; Zhu, T.; Fu, C.; He, J.; Ying, P.; Zhao, X. Tuning Multiscale Microstructures to Enhance Thermoelectric Performance of N-Type Bismuth-Telluride-Based Solid Solutions. *Adv. Energy Mater.* **2015**, *5*, 1500411/1-1500411/13.

(151) Schwarz, K. DFT Calculations of Solids with LAPW and WIEN2k. *J. Solid State Chem.* **2003**, *176*, 319–328.

(152) Davaasuren, B.; Dashjav, E.; Rothenberger, A. ChemInform Abstract: Synthesis and Characterization of the Ternary Telluroargentate K 4 [Ag 18 Te 11]. *ChemInform* **2015**, *640*, 2939–2944.

(153) Schewe, I.; Böttcher, P.; Schnering, H. G. V. The Crystal Structure of Tl5Te3and Its Relationship to the Cr5B3 Type. *Zeitschrift fur Krist. - New Cryst. Struct.* **1989**, No. 188, 287–298.

(154) Sankar, C. R.; Bangarigadu-Sanasy, S.; Assoud, A.; Kleinke, H. Syntheses, Crystal Structures and Thermoelectric Properties of Two New Thallium Tellurides: Tl4ZrTe4 and Tl4HfTe4. *J. Mater. Chem.* **2010**, *20*, 7485–7490.

(155) Assoud, A.; Shi, Y.; Guo, Q.; Kleinke, H. Crystal and Electronic Structure of the New Quaternary Sulfides TlLnAg2S3 (Ln = Nd, Sm and Gd). *J. Solid State Chem.* **2017**, *256*, 6–9.

(156) Brun, G.; Boubali, M.; Tedenac, J. C.; Ayral, R. M.; Legendre, B. Redetermination of the Phase Equilibria in the System Tl2Te-Ag2Te. *Thermochim. Acta* **1990**, *165*, 93–101.

(157) Toure, A. A.; Kra, G.; Eholie, R.; Olivier-Fourcade, J.; Jumas, J. C. Mise Au Point Sur Le Système Binaire TlTe et Affinement Des Structures de TlTe et Tl5Te3. *J. Solid State Chem.* **1990**, *87*, 229–236.

(158) Klemens, P. G. Thermal Resistance Due to Point Defects at High Temperatures. *Phys. Rev.* **1960**, *119*, 507.

(159) Saleemi, M.; Toprak, M. S.; Li, S.; Johnsson, M.; Muhammed, M. Synthesis, Processing, and Thermoelectric Properties of Bulk Nanostructured Bismuth Telluride (Bi 2Te 3). *J. Mater. Chem.* **2012**, *22*, 725–730.

(160) Poudel, B.; Hao, Q.; Ma, Y.; Lan, Y.; Minnich, A.; Yu, B.; Yan, X.; Wang, D.; Muto, A.; Vashaee, D.; Chen, X.; Liu, J.; Dresselhaus, M. S.; Chen, G.; Ren, Z. High-Thermoelectric Performance of Nanostructured Bismuth Antimony Telluride Bulk Alloys. *Science (80-.).* **2008**, *320* (5876), 634–638.

(161) Hsu, K. F.; Loo, S.; Guo, F.; Chen, W.; Dyck, J. S.; Uher, C.; Hogan, T.; Polychroniadis, E. K.; Kanatzidis, M. G. Cubic AgPbmSbTe2+m: Bulk Thermoelectric Materials with High Figure of Merit. *Science (80-.).* **2004**, *303*, 818–821.

(162) Pei, Y.; Lalonde, A. D.; Wang, H.; Snyder, G. J. Low Effective Mass Leading to High Thermoelectric Performance. *Energy Environ. Sci.* **2012**, *5*, 7963–7969.

(163) Yu, B.; Liu, W.; Chen, S.; Wang, H.; Wang, H.; Chen, G.; Ren, Z. Thermoelectric Properties of Copper Selenide with Ordered Selenium Layer and Disordered Copper Layer. *Nano Energy* **2012**, *1* (3), 472–478.

(164) Jafarzadeh, P.; Oudah, M.; Assoud, A.; Farahi, N.; Müller, E.; Kleinke, H. High Thermoelectric Performance of Ba3Cu16−x(S,Te)11. *J. Mater. Chem. C* **2018**, *6*, 13043–03048.

(165) Zhao, W. Y.; Dong, C. L.; Wei, P.; Guan, W.; Liu, L. S.; Zhai, P. C.; Tang, X. F.; Zhang, Q. J. Synthesis and High Temperature Transport Properties of Barium and Indium Double-Filled Skutterudites Bax Iny Co4 Sb12-Z. *J. Appl. Phys.* **2007**, *102*, 113708/1–113708/6.

(166) Uher, C. Chapter 5 Skutterudites: Prospective Novel Thermoelectrics. *Semicond. Semimetals* **2001**, *69*, 139–253.

(167) He, T.; Chen, J.; Rosenfeld, H. D.; Subramanian, M. A. Thermoelectric Properties of Indium-Filled Skutterudites. *Chem. Mater.* **2006**, *18*, 759–762.

(168) Kuznetsov, V. L.; Kuznetsova, L. A.; Kaliazin, A. E.; Rowe, D. M. Preparation and Thermoelectric Properties of A8IIB16IIIB30IV Clathrate Compounds. *J. Appl. Phys.* **2002**, *87*, 7871–7875.

(169) Toberer, E. S.; May, A. F.; Snyder, G. J. Zintl Chemistry for Designing High Efficiency

Thermoelectric Materials. *Chem. Mater.* **2010**, *22*, 624–634.

Permissions

“Reprinted (adapted) from Journal of Solid State Chemistry, Yixuan Shi, Cheryl Sturm, Holger Kleinke, Chalcogenides as thermoelectric materials, **2019**, *270*, 273-279, Copyright (2019), with permission from Elsevier.” (Chapter 1)

“Reprinted (adapted) with permission from (Shi, Yixuan; Assoud, Abdeljalil; Cheriyedath Raj, Sankar; Kleinke, Holger $Tl_2Ag_{12}Se_7$: A New pnp Conduction switching Material with extraordinarily Low Thermal Conductivity. *Chemistry of Materials,* **2017**, *29* (21), 9565-9571. Copyright (2018) American Chemical Society." (Chapter 3))

“Reprinted (adapted) with permission from (Shi, Yixuan; Assoud, Abdeljalil; Ponou, Simeon; Lidin, Sven; Kleinke, Holger A New Material with a Composite Crystal Structure Causing Ultralow Thermal Conductivity and Outstanding Thermoelectric Properties: $Tl_2Ag_{12}Te_{7+\delta}$. *Journal of the American Chemical Society* **2018**, *140* (27), 8578–8585. Copyright (2018) American Chemical Society." (Chapter 4)

“Reprinted (adapted) from Journal of Alloys and Compounds, Yixuan Shi, Quansheng Guo, Xiaoyu Cheng, Parisa, Jafarzadeh, Leilane R. Macario, Luke Menezes, Holger Kleinke, Thermoelectric Properties of $TlSbTe_2$ doped with In and Yb, **2019**, *795*, 1-7, Copyright (2019), with permission from Elsevier.” (Chapter 5)

“Reproduced from Ref. Journal of Materials Chemistry C, Yixuan Shi, Nour Mashmoushi, Wojciech Wegner, Parisa Jafarzadeh, Zahra Sepahi, Abdeljalil Assoud, Holger Kleinke, 2019, 7, 8029-8036, with permission from the Royal Society of Chemistry.” (Chapter 6)

Appendix

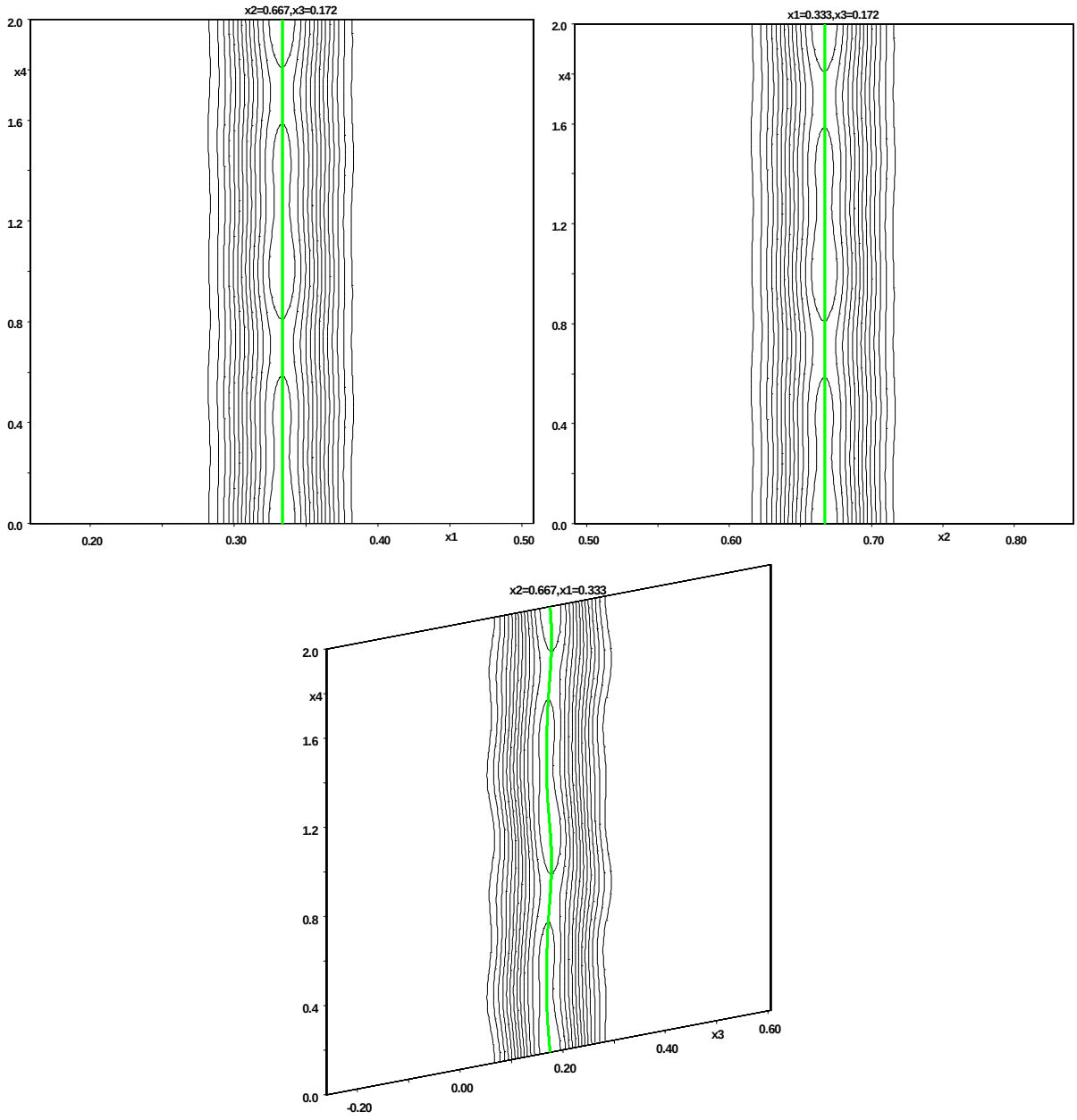

Figure A1. Atomic modulation function for Tl1. The amplitudes are identically zero for x and y, and the amplitude in z is small. This position is far away from the locus of the second composite part of the structure and is therefore barely affected by the modulation.

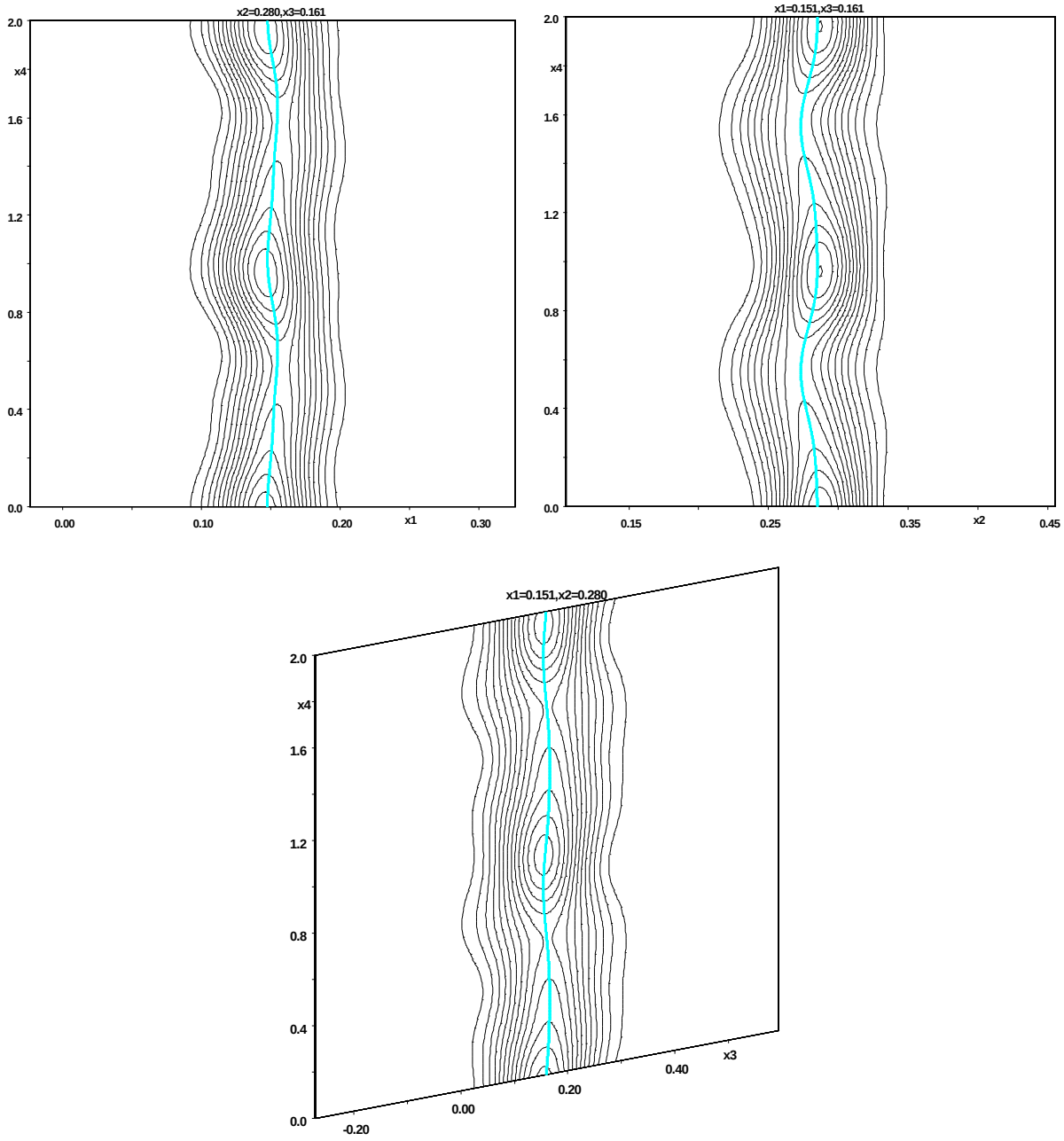

Figure A2: Atomic modulation function for Ag1. This atomic position forms the tunnel in which the second composite part of the structure, the Te2 atom, resides. As a result, this is the most strongly modulated position in the parent structure.

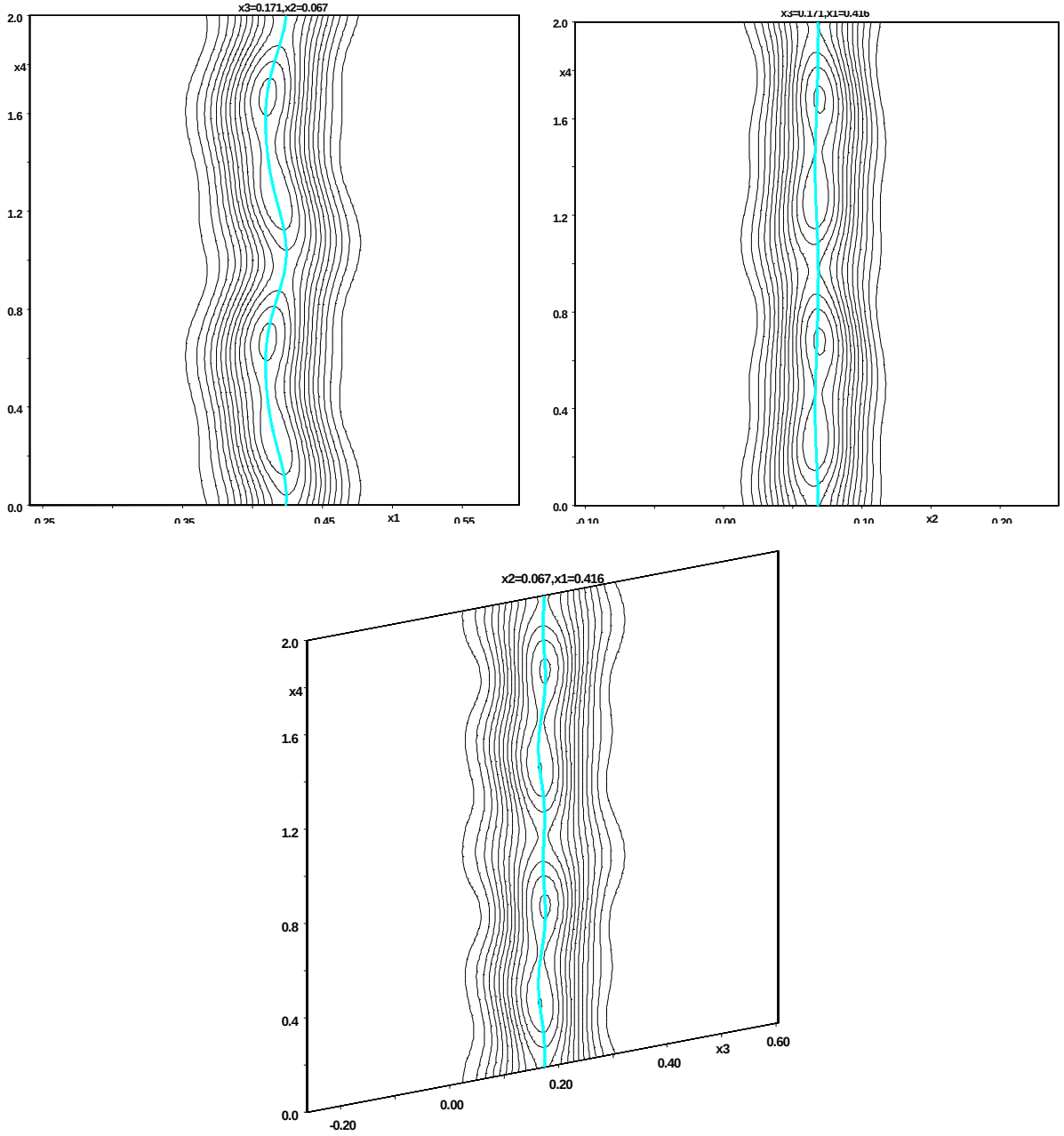

Figure A3: Atomic modulation function for Ag2. This atomic position is, together with Te1, the second nearest neighbor to the Te2 atom. The modulation of this position is moderate.

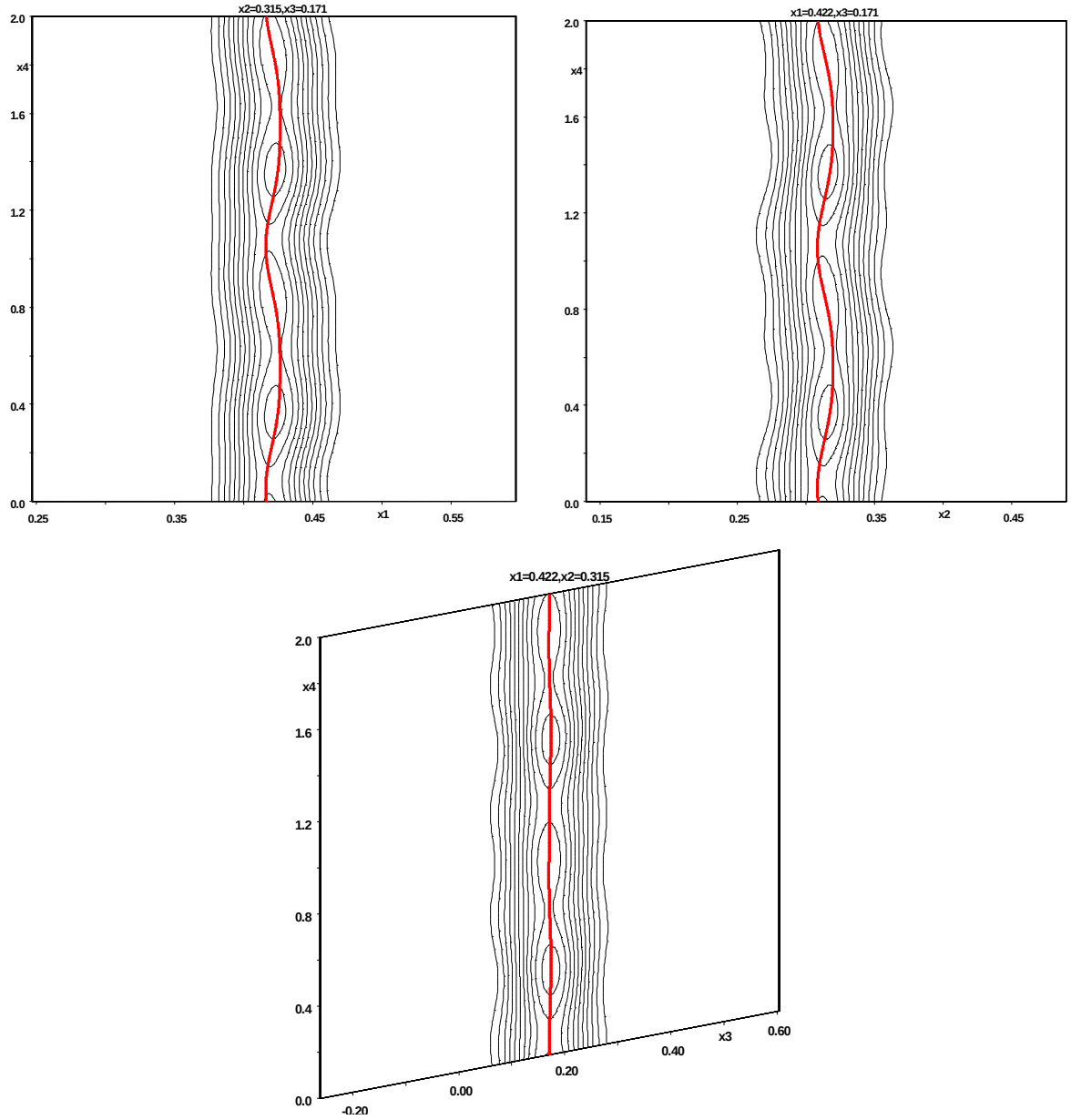

Figure A4: Atomic modulation function for Te1. Like Ag2, the modulation of this position as second nearest neighbor to Te2 is moderate, especially along z.

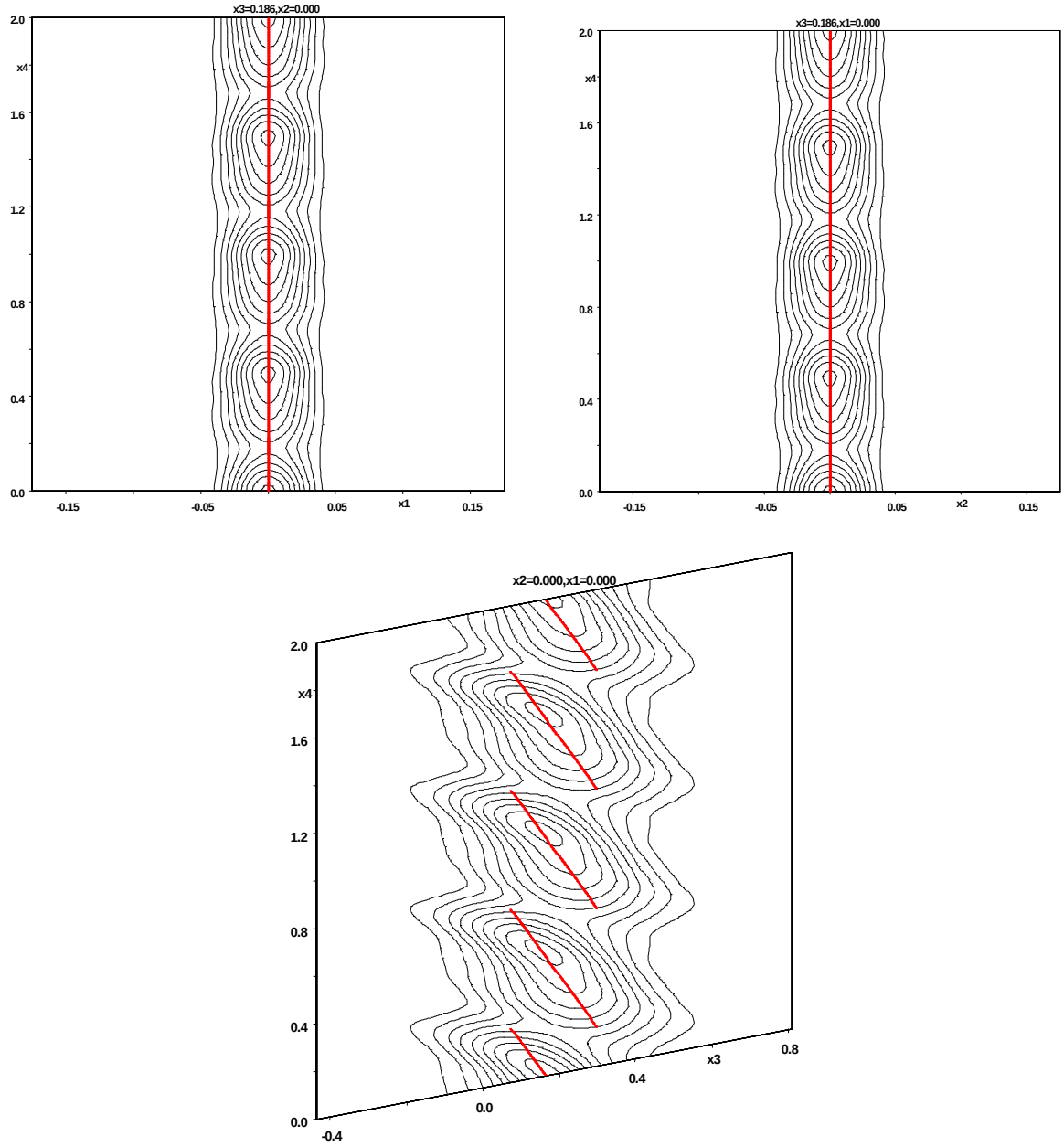

Figure A5: Atomic modulation function for Te2. Note that the atomic surface is shown in the second composite part, i.e. the c axis is shorter. If this atomic surface is shown in the first composite part cell, the modulation is boundless (Figure A6).

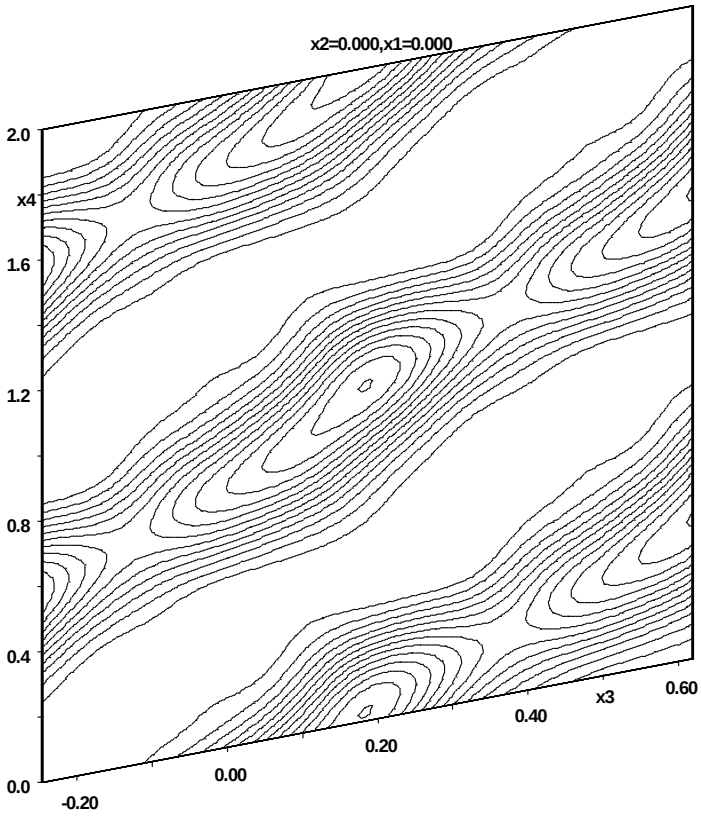

Figure A6. Atomic modulation function for Te2 shown in the first composite.

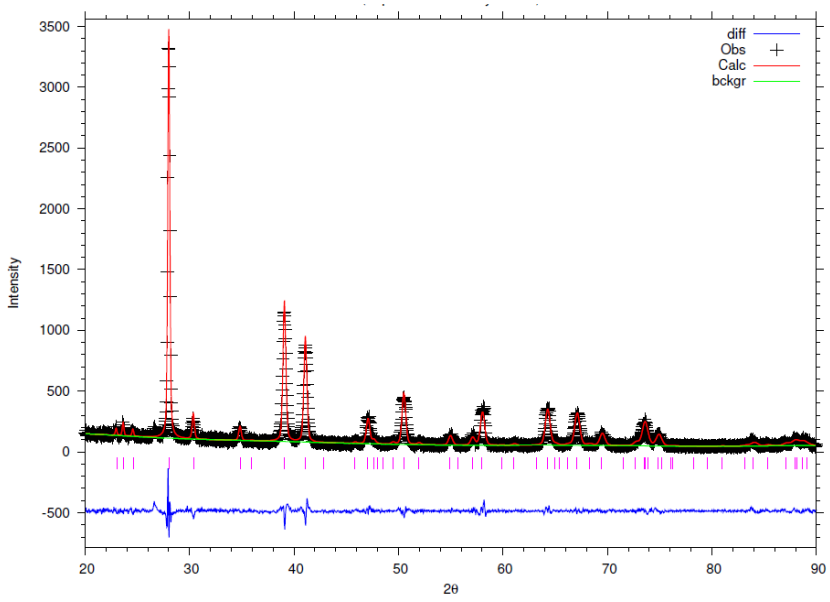

Figure A7: Powder diagram of undoped $TlSbTe_2$.

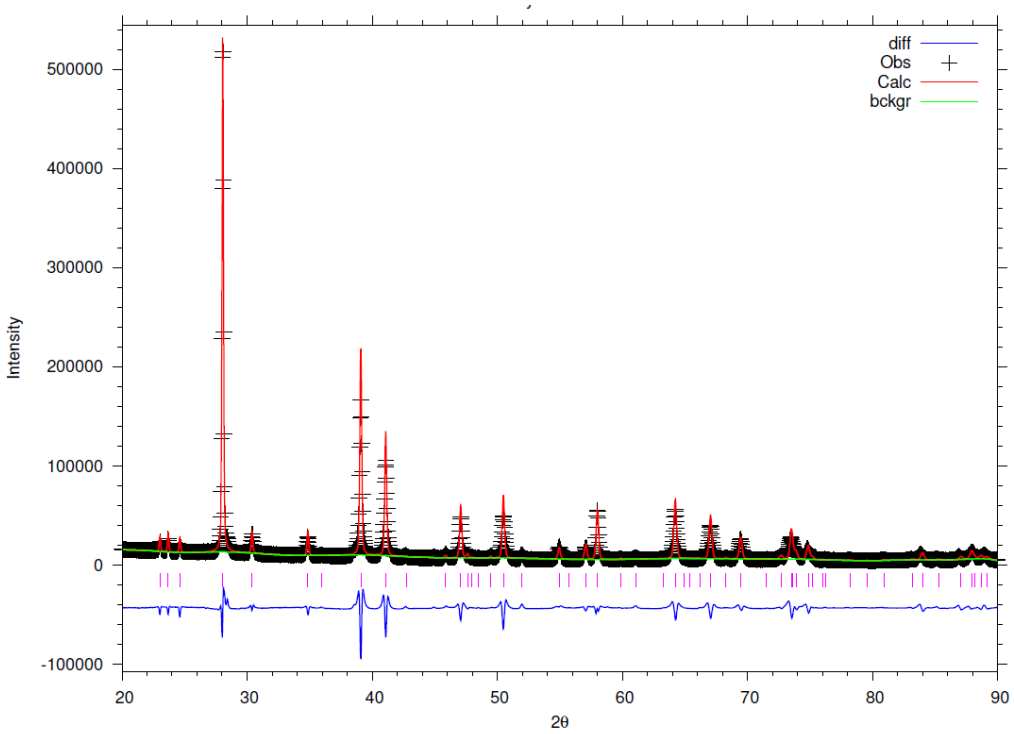

Figure A8: Powder diagram of undoped $Tl_{0.98}In_{0.02}SbTe_2$.

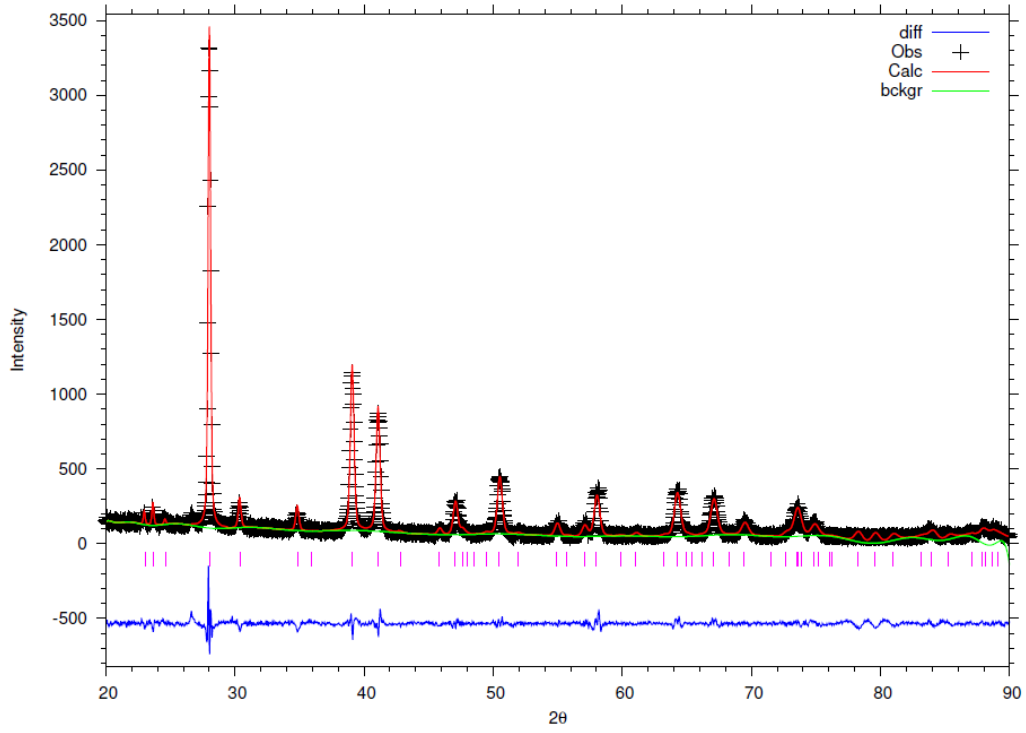

Figure A9: Powder diagram of undoped $TlSb_{0.98}In_{0.02}Te_2$.

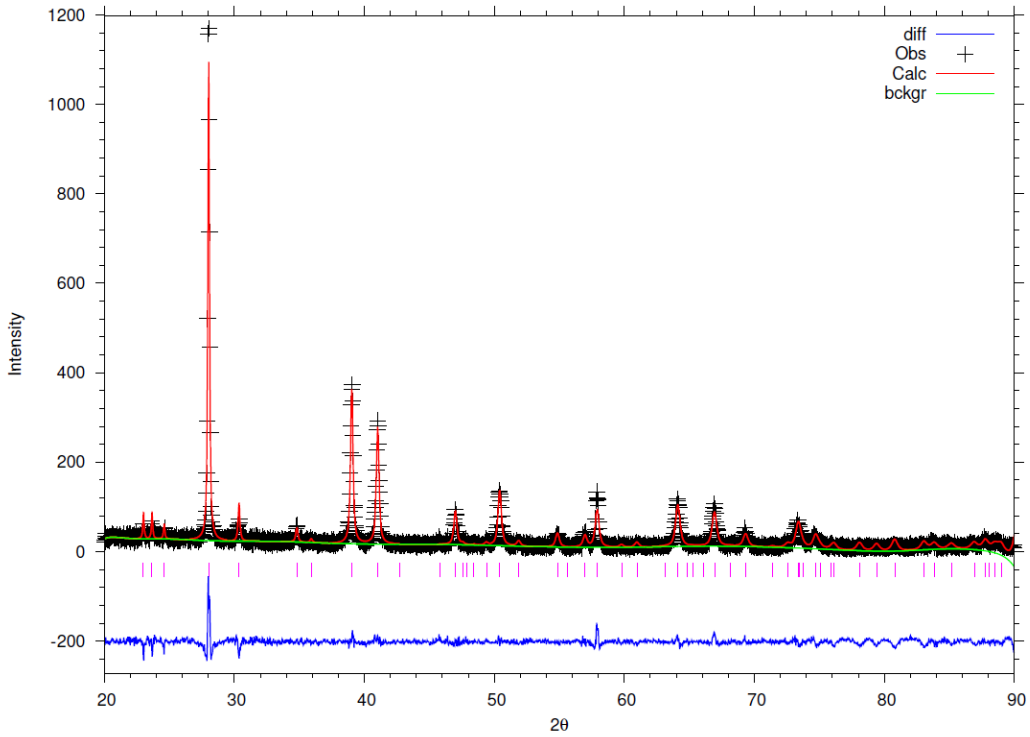

Figure A10: Powder diagram of undoped $Tl_{0.98}Yb_{0.02}SbTe_2$.

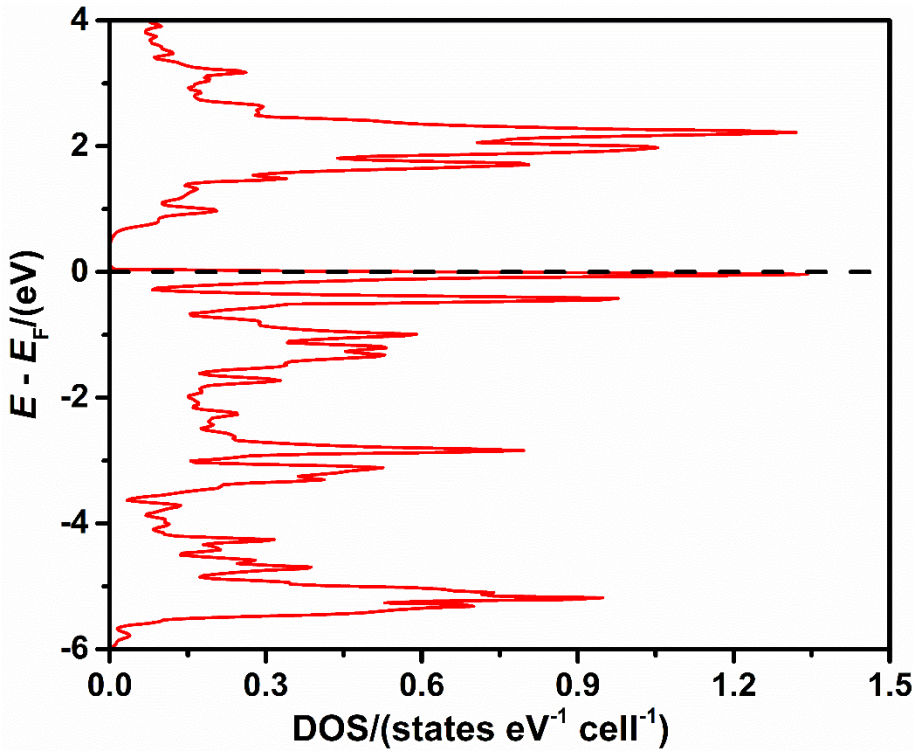

Figure A11: The partial density of states of the p_z orbital of the Te atom in the chain of the on $Tl_2Ag_{12}Te_{7.33}$ model.